Ultrafast Laser-induced Phenomena in Solids Studied by Time-resolved Interferometry

Doctoral Dissertation

for the degree of

Dr. rer. nat.

presented to the

Department of Physics,

University of Duisburg-Essen

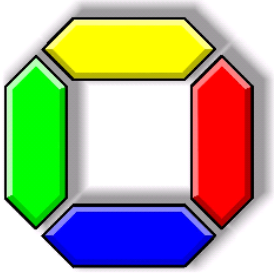

by

Vasily V. Temnov

from Nizhny Novgorod

May 2004

Ultrafast Laser-induced Phenomena in Solids Studied by Time-resolved Interferometry

Doctoral Dissertation

for the degree of

Dr. rer. nat.

presented to the

Department of Physics,

University of Duisburg-Essen

by

Vasily V. Temnov

from Nizhny Novgorod

May 2004

Chairman of the examining committee:
Prof. Dr. L. Schäfer
Referees:
Prof. Dr. D. von der Linde
Prof. Dr. R. Möller

Date of oral examination: July 29th, 2004

Contents

List of Figures

1 Introduction

The interactions of intense ultrashort laser pulses with solids give rise to a variety of very fast transient phenomena such as laser-induced melting, ablation of absorbing solids and optical breakdown in transparent materials. These processes usually manifest themselves in the transient changes of the optical properties of laser-excited material. The surface phenomena might be also accompanied by transient surface deformations. The development of ultrafast time- and space-resolved optical microscopic techniques makes it possible to carry out detailed optical studies of the dynamics of fast laser-induced phenomena, which are required to clarify the basic physical mechanisms of femtosecond laser-induced melting, ablation and optical breakdown.

Femtosecond laser ablation and optical breakdown play an important role in the processing and structuring of materials. With a suitable choice of laser parameters, e.g. wavelength, intensity and pulse duration, laser ablation can be tailored to achieve specific structuring objectives for a wide range of materials. During the past years, the use of ultrashort laser pulses has attracted increasing interest because quite impressive results have been obtained in certain types of applications. These results have stimulated an interest in the physical understanding of the mechanisms of femtosecond laser ablation and breakdown by ultrashort laser pulses.

The ablation craters produced on absorbing solid surfaces by single intense femtosecond laser pulses possess well-defined boundaries, indicating a sharp ablation threshold. Femtosecond time-resolved optical studies of short pulse laser ablation [1] have demonstrated a novel material-independent ablation mechanism, which is characterized by the formation of an optically sharp ablation front, followed by an optically transparent ablation plume. As a result, the conspicuous optical interference pattern (Newton rings) is observed in the ablating surface region a few nanoseconds after laser excitation on *all absorbing solid surfaces investigated so far*. An example of femtosecond time-resolved reflectivity snapshots on many different fs-laser excited solid surfaces taken a few nanoseconds after excitation are shown in Fig. 1. The surface area where the Newton rings are observed coincides precisely with the final ablation crater. This dynamic investigation provided an insight into the basic physical mechanisms and revealed the role of transient non-equilibrium states of matter during femtosecond laser ablation [1, 2]. However, fundamental questions about the actual internal structure of an ablating plume and the physical

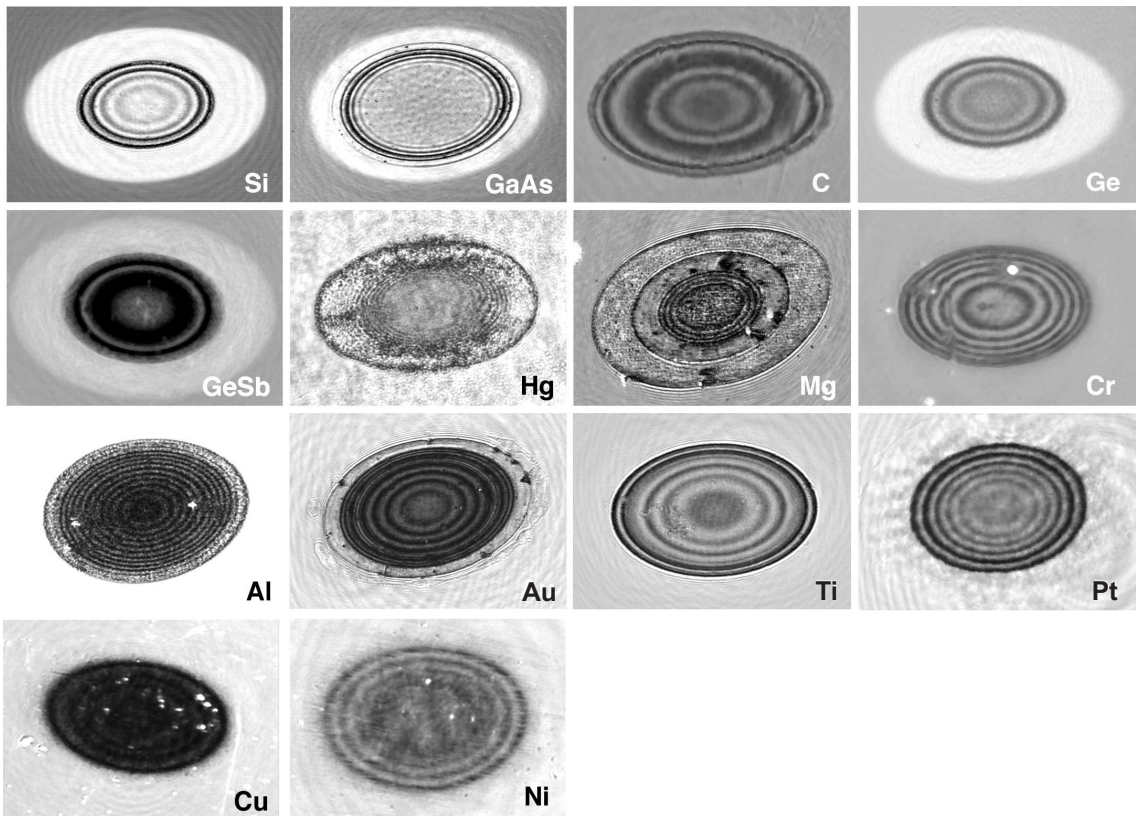

Figure 1: Femtosecond snapshots of surface reflectivity during ablation of different absorbing solids taken a few nanoseconds after excitation with single intense femtosecond laser pulses. The formation of a material-independent optical interference pattern (Newton rings) reveals the general mechanism of femtosecond laser ablation.

nature of an extremely sharp threshold of short pulse laser ablation are still open [2, 3] and motivate further experimental and theoretical investigations.

The very impressive results shown above were obtained by time-resolved optical microscopy developed by Downer and coworkers [4], which is a combination of the spectroscopic pump-probe technique with optical microscopy. It allows the time- and space-resolved measurements of the *reflectivity* of a laser-excited surface to be performed. In other words, the *amplitude* of optical probe pulses reflected from laser-excited surface may be measured. While the temporal resolution is given by the duration of the probe pulse, which can be as short as a few tens of femtoseconds, the spatial resolution is determined by the properties of the imaging optics and is of the order of a micron when using high-resolution microscope objectives [2].

However, reflectivity measurements do not help to answer a fundamental question about the physical nature of the extremely sharp threshold of short pulse laser ablation [2, 3]. Access to the dynamics of small transient surface deformations,

which are expected to appear below the ablation threshold due to the expansion of laser-heated material, is not available in pure amplitude measurements. Important information about surface deformations is contained in the *phase* of light reflected from the surface, which can be measured interferometrically. Therefore, a highly sensitive time- and space-resolved interferometric technique is required to investigate the dynamics of transient surface deformations with amplitudes of a few nanometers. The potential of ultrafast interferometric investigations will be also exploited to provide some important information about the poorly understood mechanisms of free-carrier generation in optically transparent materials by ultrashort laser pulses, which represent the key point in the understanding of optical breakdown.

This dissertation is organized as follows: apart from this first introductory chapter it contains 3 more or less independent chapters with separate summaries of the results. Chapter 2 deals with several aspects of time-resolved imaging Michelson interferometry, but the attention is focused mainly on the optical design of the setup, interferogram analysis and fully automatic phase retrieval algorithm. Two examples of interferometric measurements at a fs-laser excited GaAs-surface are used to illustrate various aspects of the technique and reveal some important problems and drawbacks concerning the physical interpretation of interferometric measurements.

Chapter 3 starts with a detailed microscopic characterization of ablation craters, which aims not only to provide a feeling about the subject of this investigation, but also reveals some new properties and amazing microscopic structures in the vicinity of ablation craters. After that some physical background about the mechanisms of femtosecond laser ablation and, in particular, the two different hypotheses concerning the properties and internal structure of an ablating plume are discussed. The main part of Chapter 2 is devoted to interferometric measurements at fs-laser excited GaAs and Si-surfaces and their physical interpretation.

Chapter 4 deals with the problem of ionization mechanisms of dielectric materials by femtosecond laser pulses. After a review of known ionization mechanisms, in which particular attention is paid to the understanding and establishing of the applicability limits of widely used but poorly understood Keldysh's theory of photoionization we present the results of interferometric measurements in fs-laser excited dielectrics. A specially designed setup for femtosecond time-resolved imaging Mach-Zehnder interferometry is used to study the *extremely fast* dynamics of laser-generated free-carriers in fused silica and sapphire.

Chapter 5 aims to summarize the main results of this work, as detailed conclusions and a discussion of future perspectives is provided in the end of each chapter.

2 Ultrafast time-resolved imaging interferometry

A brief overview of the reported time-resolved interferometric techniques and their applications serves as an introduction but also explains the motivation for further development in the field of time-resolved optical interferometry, which is the subject of this chapter.

Time- and space-resolved optical interferometry, which is a combination of a pump-probe technique with optical interference microscopy, was realized in different experimental configurations. Some of the recent applications of the conventional two-beam interferometry (such as Michelson or Mach-Zehnder) are the dynamical studies of laser ablation of polymer films irradiated by nanosecond pulses [5] and the detection of ps-laser-induced surface acoustic waves in dielectics [6]. A recently developed spectral interferometry [7] was used to investigate the expansion dynamics of fs-laser-produced plasma [7], fs-laser-driven shocks in metals [8] and the dynamics of the electron gas in the bulk of laser-irradiated dielectics [9].

The performance of a time- and space-resolved interferometric technique is determined by its (i) temporal resolution, (ii) lateral spatial resolution and (iii) phase sensitivity. The temporal resolution is determined by the duration of the probe pulse. Lateral spatial resolution and phase sensitivity are determined by the properties of the imaging optics, adjustment of the interferometer, interferogram recording and mathematical algorithms used for the processing of the interferograms.

The spectral interferometry [7] provides femtosecond time resolution and an extremely high phase sensitivity of about $\lambda/2000$. This technique requires an imaging spectrometer and has two important disadvantages. First, the lateral spatial resolution is provided only in one dimension (1D). Second, it is not easy to perform measurements for pump-probe delay times larger than a few picoseconds. The best reported realization of the conventional two-beam interferometry has a temporal resolution of about 100 ps, a 2D-lateral spatial resolution of about 10 μm, phase sensitivity of about $\sim \lambda/100$ and is characterized by a complicated imaging geometry [6]. A high phase sensitivity is achieved by taking an average of the multiple data points, which are obtained from several independent single-shot measurements.

The fundamental restrictions of spectral interferometry mentioned above motivate further development of the conventional two-beam interferometry. In particular, the improvement of the lateral spatial resolution and phase sensitivity in a single-shot measurement is required.

We have designed a simple and robust setup for optical Michelson interferometry with Linnik imaging configuration [10, 11] which is capable of measuring both very

small phase shifts $< \lambda/200$ and amplitude changes (~ 1 percent) with femtosecond time resolution (~ 100 fs) and 2D-lateral spatial resolution of about 1 μm [12]. The 2D-Fourier-transform algorithm is used to reconstruct the amplitude and phase of the interference fringes [13, 14]. The experimental interferograms used to examine the technique represent transient surface dynamics of a GaAs-surface irradiated by fs-laser pulses with fluences just below the ablation threshold. Besides the optical design of the experimental setup the main efforts are devoted to the analysis of optical image formation which appears to be very important for the optimal processing of the interferograms. A general ambiguity in the physical interpretation of the interferometric measurements is discussed. The use of additional information makes it possible to provide (at least) a qualitative interpretation of the data, which is demonstrated for presented experimental interferograms.

2.1 Setup for time-resolved Michelson interferometry

A schematic of the experimental setup for ultrafast Michelson interferometry with Linnik imaging configuration is shown in Fig. 2. A p-polarized pump pulse (Ti:Sa, $\tau = 100$ fs, $\lambda = 800$ nm) at an angle of incidence of approximately 45 deg is used to excite the surface. The excited surface area is illuminated by a weak time-delayed probe pulse (second harmonic, $\tau = 100$ fs, $\lambda = 400$ nm) normally incident on the surface through the objective lens of a high-resolution optical objective (20X, NA=0.3) which has a working distance of 17 mm. In order to achieve a spatially homogeneous surface illumination the probe pulses are subjected to spatial filtering. The use of strongly divergent probe pulses entering the microscope objective allows a large surface area in the object plane to be illuminated. The formation of the interferogram is sketched Fig. 3: in the image plane on a CCD-camera the reflected probe light (the object beam, which is visualized as a cone of rays within an angle β) interferes with a reference beam which has passed through an identical reference arm of the interferometer. By adjusting of the reference mirror a desired tilt of the wavefronts between the object and reference beam characterized by angle α in Fig. 3 is obtained, which determines the orientation and spacing between the interference fringes. We shall discuss the ray geometry of Fig. 3 in detail in the next section, since it plays an important role for the the understanding of the 2D-Fourier-transform technique used to process the interferograms. The interferograms of an unexcited surface obtained with a time difference of a few seconds are almost identical, which demonstrates good mechanical stability of the interferometer.

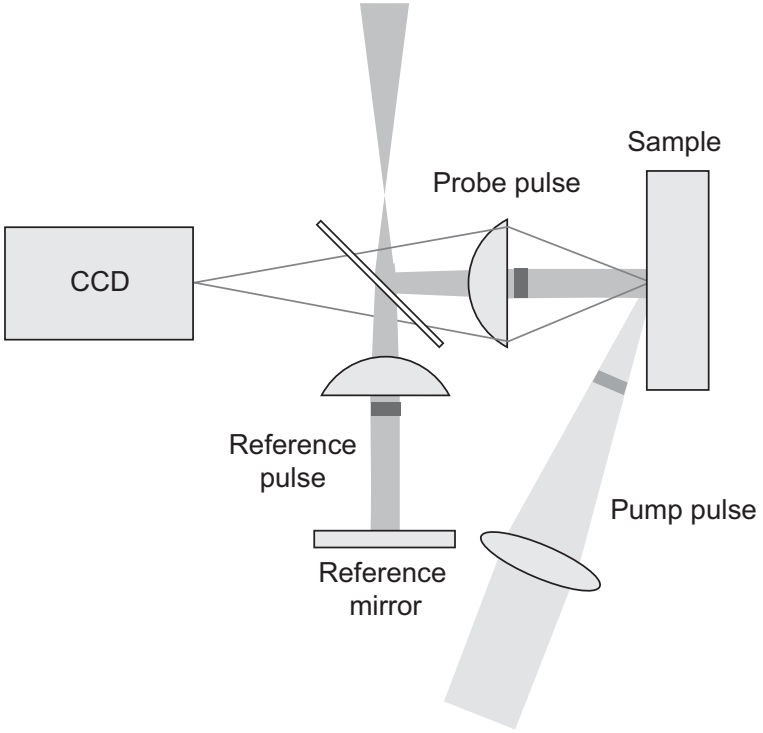

Figure 2: Setup for ultrafast Michelson interferometry with Linnik imaging configuration.

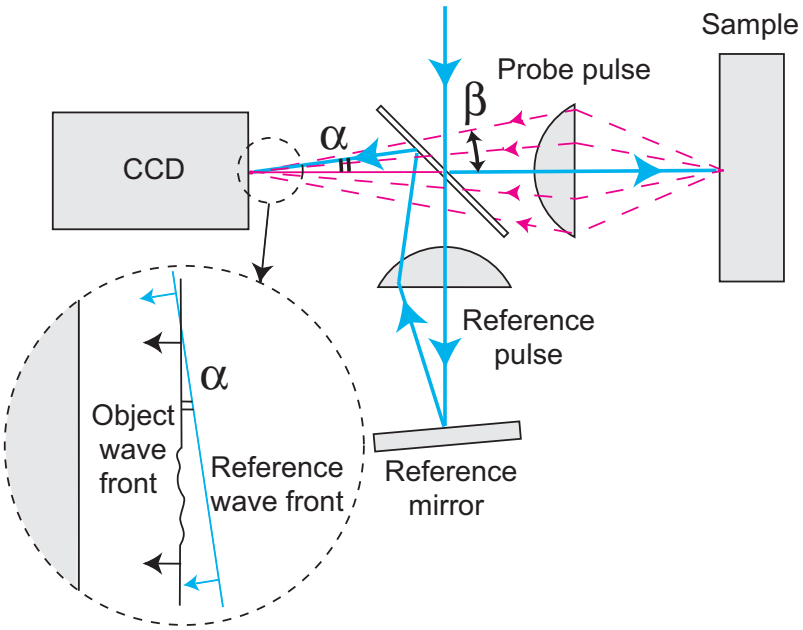

Figure 3: Formation of an interferogram in a Linnik microinterferometer.

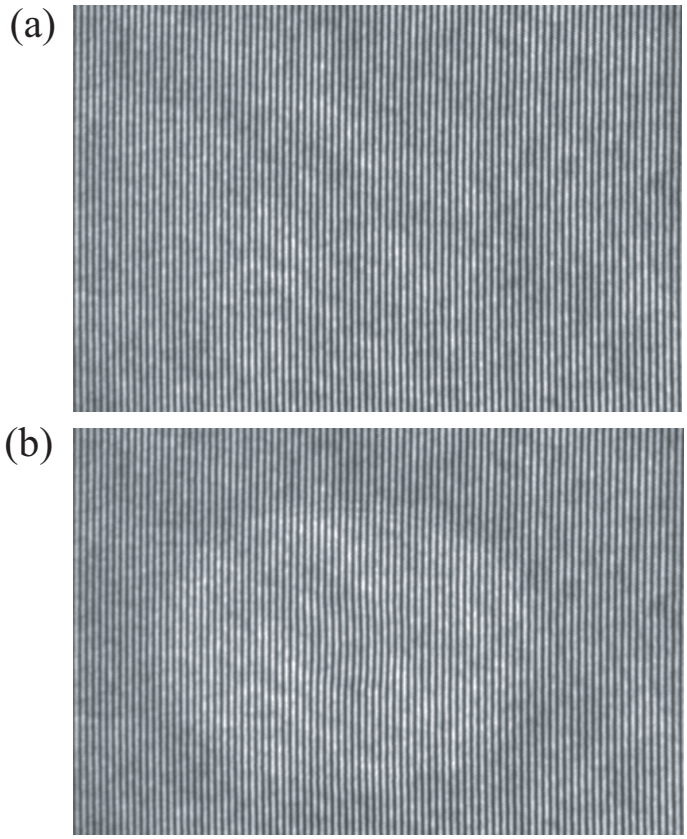

Figure 4: (a) Initial and (b) transient interferograms of GaAs(100) surface excited with $F = 0.98\ F_{thr}$, $\Delta t = 800$ ps. Frame size: 230 μm $\times$ 150 μm.

2.2 Example of an interferometric measurement

Each measurement set usually consists of three interferograms: initial interferogram of an unexcited surface, transient interferogram for a given pump-probe delay-time, and the final interferogram taken a few seconds after the excitation which characterizes the final surface modification. A step-motor controlled optical delay line allows variation of the pump-probe delay time up to a few nanoseconds with minimal steps in time of only 6.7 fs. The interferograms are acquired by an 8-bit CCD camera with a sensor area of 768x512 pixels. The high contrast interferograms with a small fringe spacing of approximately 9 pixels per fringe are well suited for the application of a Fourier-transform processing technique.

Figure 4 shows an example of an interferometric measurement for a fs-laser excited GaAs (100) surface for the pump-probe delay time $\Delta t = 800$ ps and laser fluence $F = 0.98\ F_{thr}$. In the transient interferogram almost no fringe shift can be observed by the naked eye but the bright elliptical area in the center represents an increased reflectivity of the laser-excited surface [26]. The elliptical excited area is due to the

steep angle of incidence of the pump beam. For applied laser fluence below ablation threshold the final interferogram, which is not shown in Fig. 4, is almost identical with the initial one indicating no significant changes of the optical properties and surface relief upon laser irradiation. Note that laser excitation with fluences above the ablation threshold leads to the formation of well-defined ablation craters, which can be easily detected by optical interferometry [2, 3, 15].
The main goal of time-resolved interferometric studies is not only to accurately measure the very small transient phase shifts, but also to measure the amplitude changes of probe pulses and provide their physical interpretation.

2.3 Interferogram analysis and processing by 2D-Fourier-transform technique

An interferogram $I(x,y)$ represents the spatial intensity distribution of light on a CCD-chip

$$I(x,y) = |E_{obj}(x,y)|^2 + |E_{ref}(x,y)|^2 + 2\mathrm{Re}[E_{obj}(x,y)E^*_{ref}(x,y)]\,, \qquad (1)$$

which results from the interference of the object and reference waves described by their complex amplitudes:

$$\begin{aligned} E_{obj}(x,y) &= \tilde{r}(x,y)E_1(x,y)\exp(i\phi_1(x,y))\,, \qquad (2)\\ E_{ref}(x,y) &= E_2(x,y)\exp(i\phi_2(x,y))\,. \end{aligned}$$

For the object wave we have especially introduced the complex reflection coefficient of the investigated surface

$$\tilde{r}(x,y) = r(x,y)\exp(i\Psi(x,y))\,, \qquad (3)$$

whereas for the reference wave it is omitted since it does not change.
As mentioned above, each interferometric measurement consists of at least two interferograms:

$$\begin{aligned} I_{in} &= r_{in}^2E_1^2 + E_2^2 + 4r_{in}E_1E_2\cos(\phi_1-\phi_2+\Psi_{in}) \qquad \text{(initial)}\,, \qquad (4)\\ I_{tr} &= r_{tr}^2E_1^2 + E_2^2 + 4r_{tr}E_1E_2\cos(\phi_1-\phi_2+\Psi_{tr}) \qquad \text{(transient)}\,, \qquad (5) \end{aligned}$$

where the spatial indices x and y are omitted for the purpose of simplicity. In order to extract information about transient processes we shell always compare them with an interferogram of an unexcited surface [6]: from the interferograms (4-5) we shall reconstruct the quantities

$$\begin{aligned} \Delta\Psi_{tr}(x,y) &= \Psi_{tr}(x,y) - \Psi_{in}(x,y) \qquad \text{(transient phase shift)}\,, \qquad (6)\\ \Delta r_{tr}(x,y) &= r_{tr}(x,y)/r_{in}(x,y) \qquad \text{(transient amplitude change)}\,, \qquad (7) \end{aligned}$$

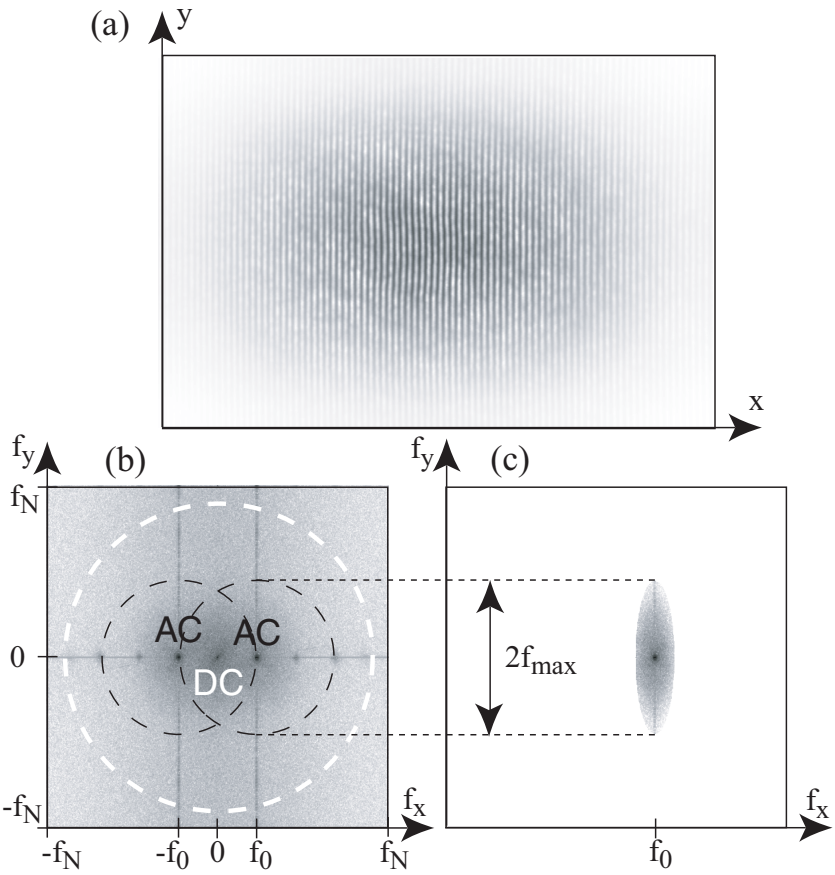

Figure 5: (a) Transient interferogram of Fig. 4(b) multiplied by a Hamming window; (b) 2D-Fourier transform of (a); (c) isolated right AC-peak of (b).

which represent the relative changes in the amplitude and phase of the object wave as compared with an unexcited surface. The normalized phase shifts and amplitude changes (6-7) contain information about transient effects, whereas the unwanted contributions to the phase and amplitude introduced by the optical components are eliminated by this normalization procedure.

In order to provide more insight into mathematical algorithms, which will be used for the processing of the interferograms, we would like to briefly discuss the formation of an interferogram in Linnik microinterferometer. The experimental interferograms of Fig. 4 consist of many parallel, vertical and almost equally spaced interference fringes. As already mentioned in the previous section, this is achieved by the proper tilting of the reference wavefront with respect to the object wavefront by adjusting the reference mirror in the interferometer. In the ideal case the object and reference wave fronts have the same curvature on a CCD-chip, which provides the linear spatial

dependence of the phase of the interference fringes:

$$\phi_1(x,y) - \phi_2(x,y) \;\simeq\; 2\pi f_0 x + const\,. \tag{8}$$

The spatial frequency of the interference fringes f_0, to be referred to as the carrier frequency, is proportional to the angle α between the two wavefronts in Fig. 3.
The next important point is that the interferometer is illuminated by spatially filtered pulses, which leads to a spatially homogeneous intensity distribution for both probe and reference pulses:

$$E_1(x,y) \simeq const\,, \qquad E_2(x,y) \simeq const\,. \tag{9}$$

Using the conditions (8) and (9) the general expression for the interferograms (4-5) can be simplified as follows:

$$I(x,y) = (1 + r^2(x,y)) + 2r(x,y)\cos(2\pi f_0 x + \Psi(x,y)))\,, \tag{10}$$

where equal amplitudes $E_1 = E_2 = 1$ are assumed. The analysis of a simplified and approximate expression (10) will help to understand the main features of the algorithm used for the reconstruction of the amplitude $r(x,y)$ and phase $\Psi(x,y)$.
A 2D-Fourier transform technique [13, 14] introduced by Takeda and coworkers [16] proved to be one of the best algorithms applied to reconstruct the amplitude and phase of the interference fringes in a case of high carrier frequency. An overview on Fourier-transform techniques is given in [17]. To illustrate the different steps of the technique we apply it to the transient interferogram of Fig. 4.
First an interferogram is multiplied by a so-called "window" which decreases from the maximal value in the center to the minimal value at the boundaries of the inteferogram, as shown in Fig. 5(a). We apply a Hamming window [18], which is widely used for the interferogram processing [17]. The purpose of "windowing" is to reduce the boundary effects of the 2D-Fourier transform [18], which is the next step in the processing: Fig. 5(b) is the squared absolute value of a 2D-Fourier-transform of the windowed interferogram in Fig. 5(a). It is plotted on a logarithmic scale since the magnitude of the 2D-Fourier transform varies over many orders of magnitude.
Due to the sampling of the interferogram recorded by a CCD-chip the frequency domain is bounded by Nyquist frequencies $f_N = 1/(2\Delta)$ where $\Delta = \Delta_{\mathrm{CCD}}/M = 300$ nm is the pixel size of an interferogram, $\Delta_{\mathrm{CCD}} = 9\ \mu$m and $M = 30$ are the pixel size of a CCD-camera and optical magnification, correspondingly. The three distinct peaks can be recognized in a Fourier plane, Fig. 5(b). The central peak located at zero frequency (DC-peak) corresponds to the term $(1 + r^2(x,y))$ in Eq. (10).

The two peaks located at frequencies $\pm f_0$ (AC-peaks) contain identical information about the amplitude and phase of the interference fringes and correspond to the term $r(x,y)\cos(2\pi f_0 x + \Psi(x,y))$ in Eq. (10). The additional sidebands or harmonics located at frequencies $f = \pm 2f_0, \pm 3f_0, ..$ have the amplitude below 10^{-2} as compared to the AC-peaks. They are caused by the nonlinear response of the CCD-camera [19, 20].

The basic idea of the Fourier-transform technique is to "isolate" one of the AC-peaks in a frequency domain by spectral filtration. The inverse Fourier transform of a filtered spectra would give the phase $2\pi f_0 x + \Psi(x,y)$ and the amplitude $r(x,y)$ of the interference fringes. The choice of an adequate shape and size of the spectral filter represents a serious problem since the location and spread of useful signal components in the Fourier plane is usually unknown.

In order to understand which parts of a Fourier plane contain the desired information about the amplitude and phase of the object wave we consider a well-known model of the optical image formation by a microscope objective with a finite numerical aperture [21, 22, 23]. Only a finite cone of rays coming from the object and collected by a microscope objective contributes to the formation of the image. The rest is "cut off" by the aperture function of the objective which implies that the object wave $r(x,y)\exp(i\Psi(x,y))$ does not contain high spatial frequency components:

$$f < f_{max} = NA/\lambda\,, \tag{11}$$

where λ is the wave length of probe pulses. In our experimental configuration the maximal frequency is $f_{max} = 0.45 f_N$. This simple analysis provides important consequences for the Fourier-transform of Eq. (10), which can be analyzed using a convolution theorem: the spectral components of the two AC-peaks must be localized within the black circles of radius f_{max} centered at frequencies $\pm f_0$ (black dashed circles in Fig. 4(b)), whereas the DC-peak components are localized within the circle of the radius $2f_{max}$ (white dashed circle in Fig. 4(b)). This result allows for a simple geometrical interpretation in terms of the angles α and β in Fig. 3:

$$f_0/f_{max} = \frac{\sin\alpha}{\sin\beta} < 1\,. \tag{12}$$

This demonstrates the importance of the proper adjustment of the interferometer and also reveals an important limitation of the Linnik microinterferometer. Indeed, it can be easily inferred from Fig. 3 that the maximal value of the angle α in the Linnik interferometer is limited by β, or, which is just the same, that the career frequency f_0 cannot exceed the cut-off frequency f_{max}. For the presented interferograms both angles are very small: $\alpha = 0.5 \times 10^{-2}$ rad, $\beta = 10^{-2}$ rad.

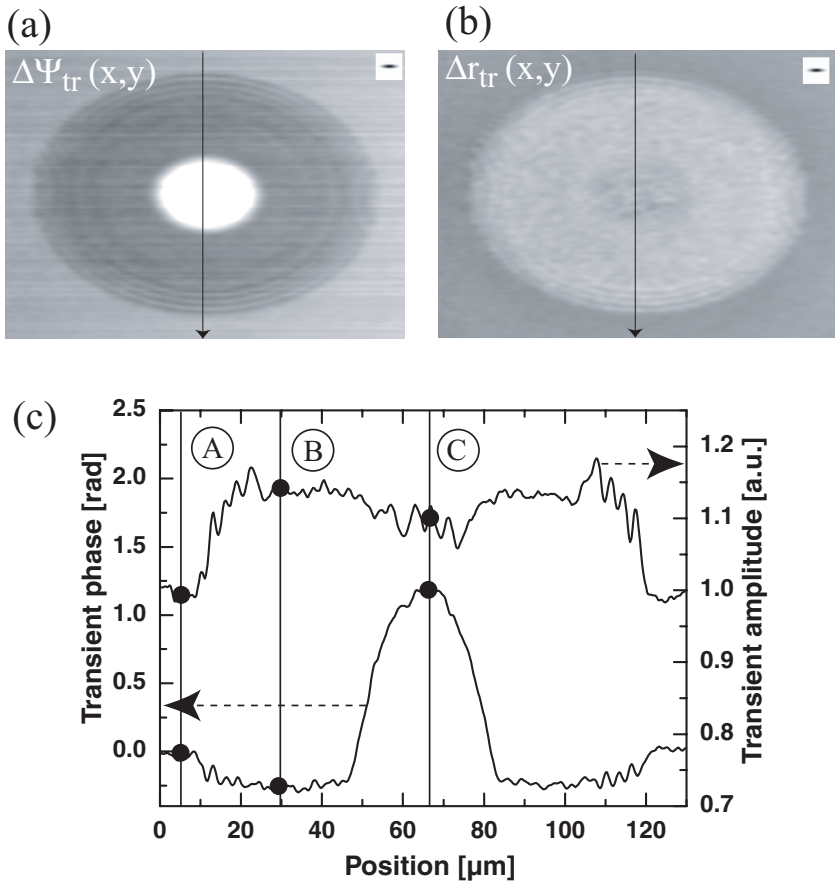

Figure 6: The reconstructed transient phase shift $\Delta\Psi_{tr}(x, y)$ (a) and amplitude change Δr_{tr} (b); the plot (c) represents the transient phase and amplitude profiles along the vertical cross-sections in (a) and (b). Frame size: 180 μm $\times$ 130 μm.

In summarizing the results of the above analysis we would like to stress the main conclusion: the components of the AC-peaks (localized within the black dashed circles in Fig. 5(b)) cannot be fully separated from the central DC-peak (localized within the white dashed circle in Fig. 5(b)). This fundamental limitation is determined by the interferogram formation in the Linnik microinterferometer and makes it impossible to clearly separate the spectral components describing the *amplitude* and the *phase* of interference fringes in a Fourier-plane.

Nevertheless, under certain conditions one of the AC peaks in a Fourier plane (we have chosen the right one) can be reasonably isolated by means of spectral filtration in such a way that the important information about the amplitude and phase of the interference fringes is not lost. We have used an elliptical Hamming filter with the following properties: its vertical size was chosen to be equal to the cut-off frequency of the microscope objective in order to maintain the best possible spatial resolution

in the y-direction, whereas its horizontal size is four times smaller in order to obtain a reasonable separation of the AC-signal components from the central DC-peak (Fig. 5(c)).

The angle of the inverse Fourier transform of the filtered Fourier spectra (Fig. 5(c)) is equal to the total phase of the transient interferogram $\phi_1(x,y) - \phi_2(x,y) + \Psi_{tr}(x,y)$, whereas its amplitude is equal to $2r_{in}(x,y)E_1(x,y)E_2(x,y)$. The initial interferogram is subjected to the same processing as the transient one and the normalized phase shifts (6) and amplitude changes (7) are calculated, which are presented in Fig. 6. The phase shift is unwrapped (i.e. the 2π discontinuities removed) using the simple unwrapping algorithm of Takeda [16].

The spatial resolution in the reconstructed phase and amplitude maps is determined by the size and shape of the response function of the spectral filter (Fourier transform of the filter), which is plotted in the right upper corner of Fig. 6(a,b). Since the used elliptical Hamming filter (see Fig. 4(b)) is asymmetric its response function is also asymmetric, which gives different lateral resolutions

$$\Delta x = 6.0\ \mu\mathrm{m}\,,\ \Delta y = 1.5\ \mu\mathrm{m} \tag{13}$$

in horizontal and vertical directions correspondingly. The shape of the Hamming filter makes the resolution in the vertical direction worse than the conventional Rayleigh resolution limit $0.6\lambda/NA = 0.8\ \mu$m [23], but it allows the errors due to the boundary effects of the Fourier-transform to be reduced [17]. The better spatial resolution in the vertical direction suggests it would be beneficial to analyze the vertical profiles of the phase and amplitude maps, which are presented in Fig. 6(b) and will be discussed in detail in the following section.

Complementary to the lateral spatial resolution we define the accuracy of phase and amplitude measurement as a standard deviation (root mean square) of the normalized phase and amplitude maps (Fig. 6(a,b)) measured over the area not excited by the laser pulse:

$$\begin{aligned} &\mathrm{rms}\quad \{\Delta\Psi_{tr}(x,y)\} \simeq \pi/100\,, \\ &\mathrm{rms}\quad \{\Delta r_{tr}(x,y)\} \simeq 0.01\,. \end{aligned} \tag{14}$$

Thus the calculated values (13) and (14) can be used to characterize the resolution of the reconstructed phase and amplitude maps.

It is clear that the choice of the spectral filter is very important since it influences both the lateral spatial resolution (13) and the sensitivity to phase and amplitude changes (14). The optimal filter choice depends on the optical design and adjustment of the interferometer as well as on the observed phase and amplitude signals.

The influence of noise introduced by the acquisition of the interferograms, which is disregarded in our study, could also be very important [13].

A significantly improved performance of the Fourier-transform technique could be achieved by the application of the so-called correction for the continuum [14, 24]. The idea is first to estimate somehow the background illumination (DC-peak), which can be used to "correct" the interferogram. The Fourier spectra of such a corrected interferogram does not contain a DC-peak, which leads to a better isolation of the desired signal components of the AC-peaks. Unfortunately, this approach is limited to the situation in which the background illumination is always the same. The background illumination of our transient interferograms (5) is influenced by transient reflectivity changes, and such a simple correction procedure cannot be applied.

In trying to provide a general description of the technique we have disregarded the fact that the used pump pulses possess a perfect bell-shaped fluence distribution, which produces nice elliptical structures in phase and amplitude maps. In other words the contours of constant fluence are ellipses: the smaller the fluence the larger the size of the ellipses. Therefore the images contain much more physical information about the fluence-dependence of phase and amplitude than that provided by single spatial profiles analyzed so far. For example on the phase map (Fig. 6(a)) one can easily recognize many rings with the naked eye. In the vertical phase cross-section of Fig. 6(c) such rings correspond to tiny oscillations between points A and B, but not all of these rings can be found: they just cannot be distinguished from noise. When we restrict ourselves to analysis of certain cross-sections a lot of important information is lost! Therefore, in some cases, when the pure lateral spatial resolution in the horizontal direction is not crucial, we will analyze profiles or cross-sections *averaged* over different directions. It is quite easy to implement this procedure of spatial averaging technically. Given the exact position and eccentricity of the ellipse the phase and amplitude values are averaged over thin elliptical rings which are plotted against the size of the rings. This procedure improves significantly the signal-to-noise ratio as compared to (14), sometimes by orders of magnitude! Given the spatial fluence distribution, which can be measured experimentally, a highly accurate dependence of phase shifts and amplitude changes on excitation fluence can be obtained. The results of such data processing enable, for example, the clear measurement of tiny thermo-acoustic oscillations of laser-molten material, which will be discussed in the next chapter.

2.4 Physical interpretation of the interferometric measurements

In order not to overload the next chapter which deals with the physical mechanisms of femtosecond laser ablation with the details of the interferometric technique, we shall now discuss here some important problems concerning the physical interpretation of interferometric measurements. The first question, i.e. how to clearly identify small geometrical surface deformations will be treated by analyzing the interferometric data presented in the last section. The second important set of questions, as well as some drawbacks of the technique, will be introduced using some examples of interferometric measurements at an ablating GaAs-surface.

2.4.1 Is it possible to identify a small geometric surface deformation ?

In the previous section we have reconstructed the phase shifts and amplitude changes of light waves upon reflection from a laser-irradiated GaAs-surface 800 ps after laser excitation presented in Fig. 6. As already mentioned above, the optical properties of the surface might change due to (i) changes of the optical constants upon laser excitation and (ii) surface deformations.

Let us first analyze the reflection of a normally incident plane electromagnetic wave (object wave) from a surface characterized by a deformation $d(x, y)$ and complex index of refraction $\widetilde{n}(x, y) = n(x, y) + ik(x, y)$. The spatial indices x and y will be omitted further. Since the spectra of our 100 fs long probe pulses are quite narrow ($\Delta\omega/\omega \sim 0.01$) we may use the approximation of a monochromatic wave. Assuming an $\mathrm{e}^{-i\omega t}$-process we fix a positive sign of the imaginary part of the refractive index, $\widetilde{n} = n + ik, k > 0$, which corresponds to the damping of the wave in the propagation direction [25]. Whereas the complex reflection coefficient of an undeformed surface is described by the simple Fresnel formula

$$\widetilde{r}_{fr} = r_{fr}\mathrm{e}^{i\phi_{fr}} = \left(\frac{1-\widetilde{n}}{1+\widetilde{n}}\right), \tag{15}$$

where the Fresnel convention for the sign of the reflected wave is used [25], the surface deformation provides an additional contribution to the phase of reflected light:

$$\widetilde{r} = r_{fr}\mathrm{e}^{i(\phi_{fr}+(4\pi/\lambda)d)}\,. \tag{16}$$

Under the set of conventions used (the assumption of an $\mathrm{e}^{-i\omega t}$-process and the Fresnel sign convention) the surface excursion ($d > 0$) induces a positive phase shift in (16). The results of the forthcoming analysis will be, of course, independent of the

particular set of conventions used, which is a matter of personal taste [25]. The two basic formula (15) and (16) will be used in the forthcoming analysis.

The interferometric measurements provide information about (i) the amplitude of the reflected object wave which is determined by the optical constants only and (ii) the phase of the reflected wave which might be influenced both by the changes in the optical constants and surface deformations. The two measured quantities are obviously not enough to determine the three unknown parameters in (16), which are r_{fr}, ϕ_{fr} and d. Thus, some additional information or assumptions are required to provide a physical interpretation of the experimental data.

Now we shall focus on the spatial phase and amplitude profiles of Fig. 6(c). Starting from the reference values of an unexcited solid (point A) the amplitude rapidly increases by 13%, whereas the phase decreases by -0.08π (point B). In the vicinity of point B the amplitude and phase do not change as a function of the coordinate forming a "plateau". In the center (point C) the phase reaches a maximum of about 0.4π and the reflectivity slightly decreases.

The formation of a "plateau" in the amplitude of reflected light (in the vicinity of point B) represents the area of high constant surface reflectivity and is consistent with the previous observations provided by time-resolved microscopy [26]. It can be physically interpreted as a result of the laser-induced melting of semiconductors [1] with the thickness of the molten layer being larger than the penetration depth of the probe pulse.

Our time-resolved interferometric measurements, which will be discussed in detail in the next chapter show that at point B both the amplitude and phase approach the constant values very fast (within approximately 1 ps after excitation) indicating a fast melting process [26], and remain unchanged for a few nanoseconds, after which the liquid semiconductor cools down and resoldifies. Exploiting a simple argument that the time needed for the surface deformations to arise is very large as compared to 1 ps, this observation suggests that point B in Fig. 6 describes an *undeformed* laser-molten GaAs layer with a thickness larger than the skin-depth of the probe light. The observed decrease of the phase is thus associated only with the changes in the optical constants according to the Fresnel formula (15). At this point it is worth mentioning that it is an ultimate femtosecond temporal resolution that allows for such simple understanding and interpretation of the experimental data.

In order to calculate the optical constants of liquid GaAs it should be noted that our interferometric amplitude and phase measurements are relative with respect to

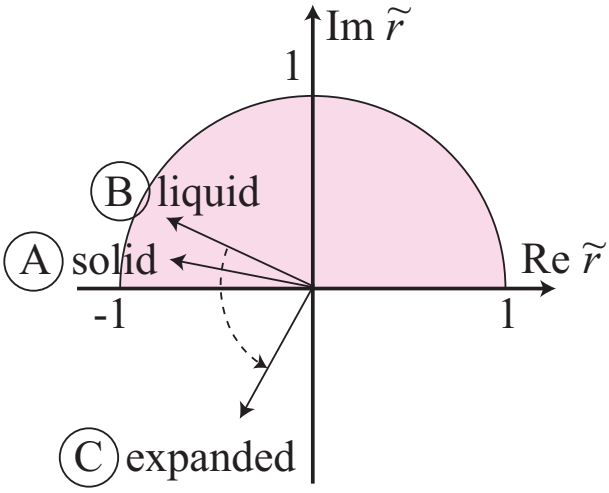

Figure 7: Physical interpretation of interferometric measurements. Complex reflectivity vectors for 3 points on Fig. 6(c): (A)-solid GaAs, (B)-liquid GaAs, (C)-expanded surface. The dark region contains all possible complex reflection coefficients of an undeformed surface (see text for details).

an unexcited solid. Taking the optical constants of unexcited GaAs [27]

$$\widetilde{n}_{\text{solid}} = 4.373 + 2.146i \tag{17}$$

for $\lambda = 400$ nm as a reference and using the Fresnel formula (15) the complex index of refraction of liquid GaAs can be determined:

$$\widetilde{n}_{\text{liquid}} = 2.0 + 3.4i\,. \tag{18}$$

The small real and large imaginary part of the refractive index (18) clearly demonstrates the metallic optical properties expected for liquid GaAs.

In order to interpret the phase and amplitude changes observed in the center of the laser-irradiated area (point C), we shall make use of a formula (16). It is very convenient to present an arbitrary complex reflection coefficient (16) by a vector on a complex reflectivity diagram, Fig. 7. The dark area contains all possible Fresnel reflection coefficients (15) for all possible optical constants $n > 0, k > 0$. Thus, the reflection coefficients (15) of any *undeformed* surface ($d = 0$) are obliged to lie inside the dark area.

The complex reflection coefficients A, B and C in Fig. 7 represent the corresponding points in Fig. 6(c). The complex reflection coefficients A and B lie within the dark area, which is in agreement with our previous conclusions, namely that they describe undeformed solid and liquid GaAs surfaces correspondingly. Vector C lies well outside of the dark region. This cannot be explained by pure change in the

optical constants, but it represents transient surface excursion. Assuming that the phase difference of $\delta\phi = 0.38\pi$ between vectors B and C is mostly induced by surface excursion we get an estimate of its amplitude:

$$d \simeq (\lambda/4\pi)\delta\phi = 38 \text{ nm}\,. \tag{19}$$

We believe that this conclusion based on a simplified formula (15) will also hold for a more sophisticated analysis, which accounts for the spatially inhomogeneous optical properties within the laser-heated layer.

It immediately follows from the above analysis of the optical constants that (i) huge phase shifts of the order of the wavelength or larger are mostly induced by surface deformations but (ii) smaller phase shifts should be carefully analyzed before providing their interpretation. In concluding this section, we would like to mention that in principle, the phase sensitivity of the technique is high enough to detect surface deformations with amplitudes of only 1 nm. The use of previously introduced spatial averaging techniques exploiting the elliptical symmetry of spatial fluence distribution makes possible to measure surface displacements in the *angstrom* range! Despite an intrinsic ambiguity of the interferometric measurements the available experimental data allowed us to distinguish the contributions due to (i) the changes of the optical constants due to melting and (ii) transient surface deformations. A general approach based on the analysis of complex reflection coefficients appears to be helpful in physical interpretation of the interferometric data.

2.4.2 Some examples of interferometric measurements at ablating GaAs-surface

So far we have illustrated and discussed the details of interferometric technique by using only one example. In this subsection we shall present and discuss in detail some more examples, which help not only to reveal the problems and drawbacks of the interferometric technique itself but also explain some artifacts in well-known experimental data obtained by time-resolved microscopy many years ago.

Figure 8 show two examples of transient interferometric measurements at an ablating GaAs-surface excited 30% above the ablation threshold for two different delay times 1.8 ns and 3.3 ns. The five consequent images for each delay time are: transient interferograms (a1,b1), their Fourier spectra (a2,b2), filtered Fourier spectra (a3,b3), reconstructed phase shifts (a4,b4) and reflectivity changes (a5,b5). In contrast to the previously analyzed interferograms of a GaAs-surface excited below ablation threshold, the interferograms in Fig. 8 show big displacement and contrast modulation of interference fringes within a laser-excited area, which seem to be more pronounced

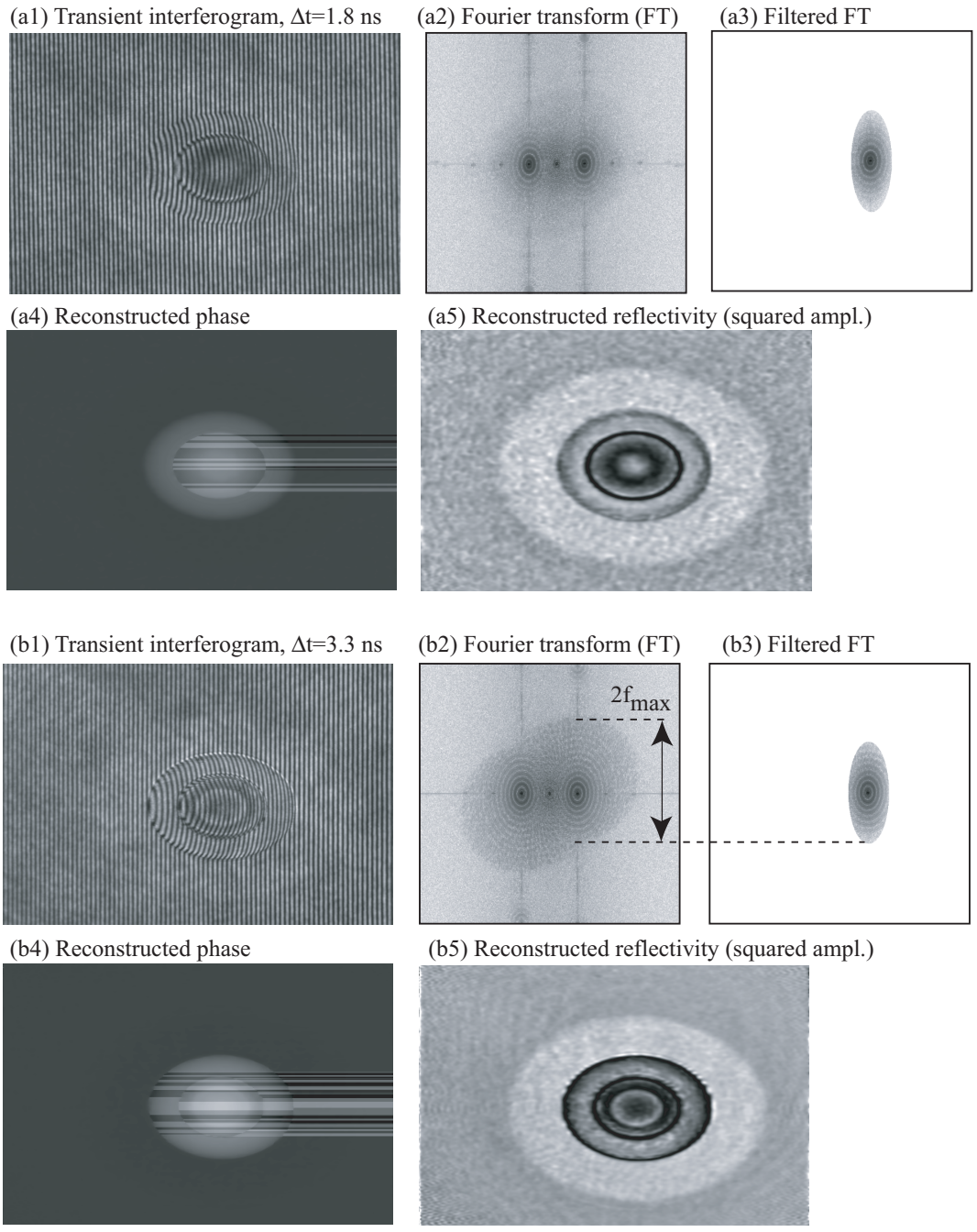

Figure 8: Two examples of transient interferometric measurements at ablating GaAs-surface, $F = 1.3\ F_{thr}$, made at two different delay times $\Delta t = 1.8$ ns (a1-a5) and $\Delta t = 3.3$ ns (b1-b5).

for a larger delay time of 3.3 ns. The corresponding Fourier spectra show a sequence of dark rings around the AC-peaks, which are again much more pronounced in the second case. In the Fourier spectra (b2) we can recognize the two dark overlapping circular areas with diameter $2f_{max}$ (see Eq. (11)). These circles mark the location of spectral components of the AC-peaks as described in the previous section. In contrast to the two circles in Fig. 5(b), which are horizontally displaced with respect to the central DC-peak, the two circles in Fig. 8(b2) are also displaced in a vertical direction. Note that the positions of the two circles in Fig. 5(b) are calculated assuming a perfect adjustment of the interferometer, i.e. a perfectly centered (aligned on-axes) object beam and horizontally displaced reference beam.

An extended routine analysis (which will not be discussed here) shows that additional vertical displacement of the two circles in the Fourier plane can be explained by a slight misalignment of the interferometer, in which the vertical position for both the reference and the object beams is equally displaced with respect to the optical axes of the microscope objectives. Since the spacing and vertical orientation of interference fringes remain unchanged for this type of misalignment, it can hardly be recognized by looking at the interference pattern.

The fact that we are able to see the discussed circular areas in real spectra indicate that some frequency components are indeed cut off by the microscope objective. In other words the laser-excited surface exhibits extremely sharp spatial phase and/or reflectivity modulations, which cannot be resolved by our optical microscope. During interferogram processing we must apply an even smaller spectral filter to isolate an AC-peak and thus artificially cut further relevant signal components. This phenomena is called ”aliasing” or ”energy leakage” [29, 30] in the interferometry and gives rise to some artifacts in the reconstructed phase and amplitude maps. One of the artifacts readily manifests itself in the phase maps (a4,b4) of Fig. 8: the phase could not be correctly unwrapped. Note that we have applied the same type of unwrapping algorithm we used to get the spatially continuous phase distribution in Fig. 6(a). Phase values between the neighboring dark and bright horizontal stripes in phase maps (a4,b4) differ by the multiples of 2π. The number of such stripes is much higher in the phase map corresponding to the longer delay time 3.3 ns, for which the problem of ”aliasing” is expected to be more significant.

Before starting to tackle the problem of unwrapping ”bad” phase data we shall present the last example of interferometric measurement of final surface morphology of a GaAs-surface after laser ablation. The reason for doing this first will become clear later.

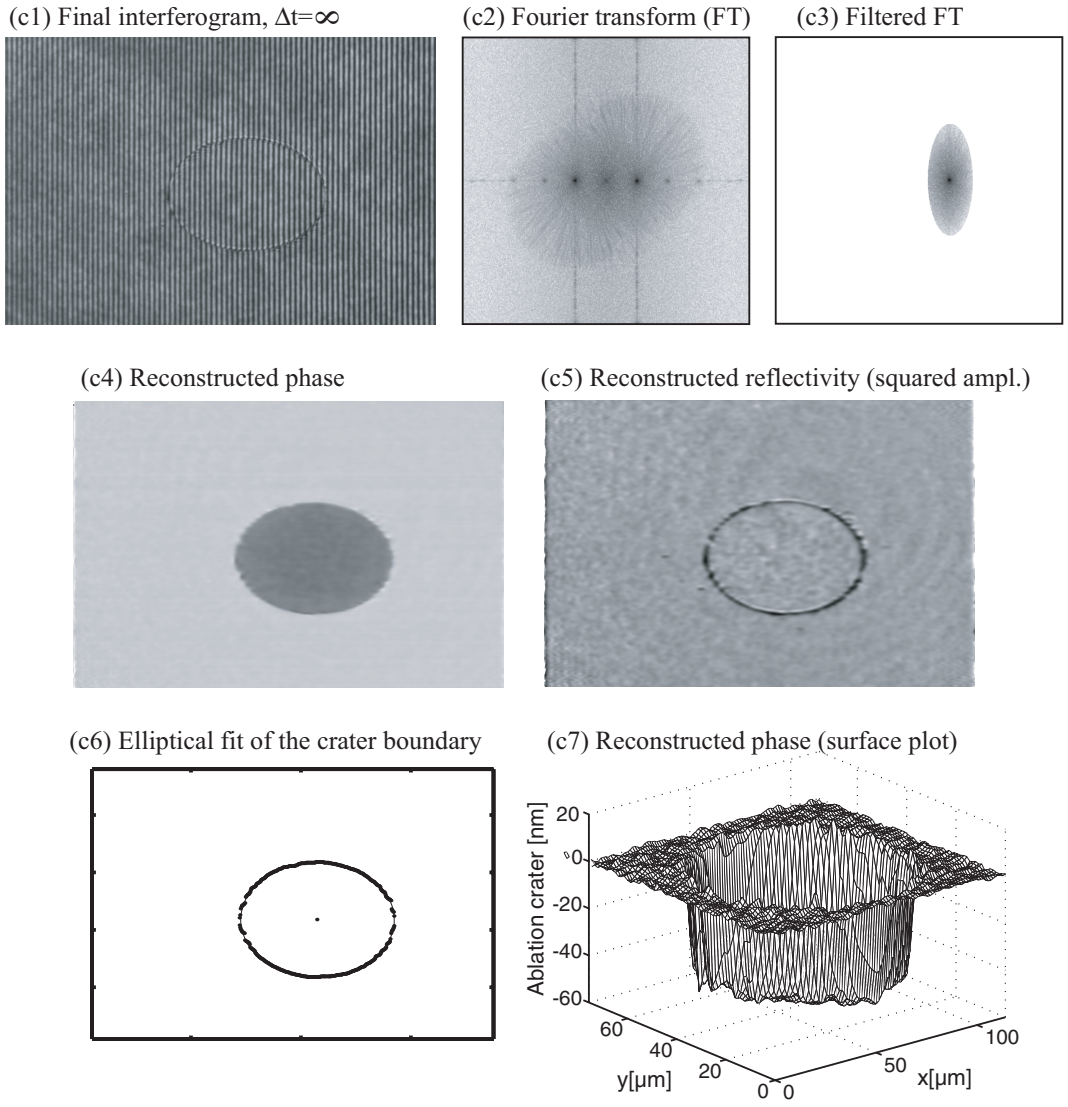

Figure 9: Interferometric measurement of final ablation crater on GaAs, $F = 1.3\ F_{thr}$.

Figure 9 shows a similar sequence of images to the one we have just discussed for Fig. 8 and illustrates the processing of the final interferogram of a GaAs-surface after laser excitation with peak fluence 30% above the ablation threshold: final interferogram (c1), its Fourier spectra (c2), filtered Fourier spectra (c3), reconstructed phase shift (c4), reflectivity change (c5) plus two more plots (c6,c7) to be discussed later. The final interferogram (c1) contains an elliptical ring at which interference fringes experience a jump. This jump represents the boundary of the ablation crater and is induced by the permanent removal of a macroscopic amount of the material from a solid surface as result of laser ablation [2]. Fourier spectrum (c2) does again possess the two clear cut-off circles, indicating that the crater boundary is extremely

sharp compared to the optical resolution, and we again have a problem of "aliasing". The reconstructed phase is surprisingly well unwrapped by the same algorithm, so the phase map (c4) does not show any sudden phase jumps of 2π. A dark black ring indicates the crater boundary in the reconstructed reflectivity map (c5). Except for this ring surface reflectivity is constant and equal to that of solid GaAs, which suggests that there is no additional phase shift due to changes in the optical constants. For this reason we can can directly convert the reconstructed phase to surface profile according to Eq. 19, which is visualized in Fig. 9(c7) as a surface plot. The ablation crater has a depth of 40 nm=0.4π and possesses very steep walls. Because of these steep walls it is technically easy to determine the position of the crater boundary, say at half of the crater depth, and fit it with an ellipse. The result of this procedure is presented in Fig. 9(c8). The knowledge of the exact position and size of the ablation crater provides important information about the position and the energy of the pump pulse used to excite the sample, which will be important for fully automatic processing of interferometric data.

2.4.3 Unwrapping of "bad" phase data

Provided with the exact position of the excitation pulse on the sample we return to the problem of unwrapping the "bad" phase data of Fig. 8(a4,b4). Figure 10 aims to explain where the problems with unwrapping come from. The phase maps (a1,b1) in Fig. 10 are identical to whose in Fig. 8(a4,b4). They have been unwrapped line-by-line in a horizontal direction. Figures (a2,b2) are the same phase maps as (a1,b1) but unwrapped line-by-line in vertical directions, which leads to different results. Vertical and horizontal cross-sections of these maps are presented in Fig. 10(a4,b4) correspondingly. The two phase cross-sections in plot (a4) are quite remarkable: at the points, where the slope of the vertical phase profile of map (a2) is maximal, the horizontal profile of map (a1) experiences a negative jump. The difference in the center of the laser-excited value appears to be 2π, as expected from the wrong unwrapping procedure. The correct phase profile is obviously that in the vertical direction since we have a much better spatial resolution in this direction determined by the choice of spectral filter. If the size of the spectral filter in vertical direction is reduced, then the vertical phase profile becomes like the horizontal one, i.e. with a negative phase jump. Thus, the problems with unwrapping originate from aliasing. There exists a very useful interferomertic trick, which allows one to find the so-called inconsistent phase values which cannot be unwrapped by *any* unwrapping algorithm in principle. The idea is to compare the phase value $p_{x,y}$ at an arbitrary point x, y of

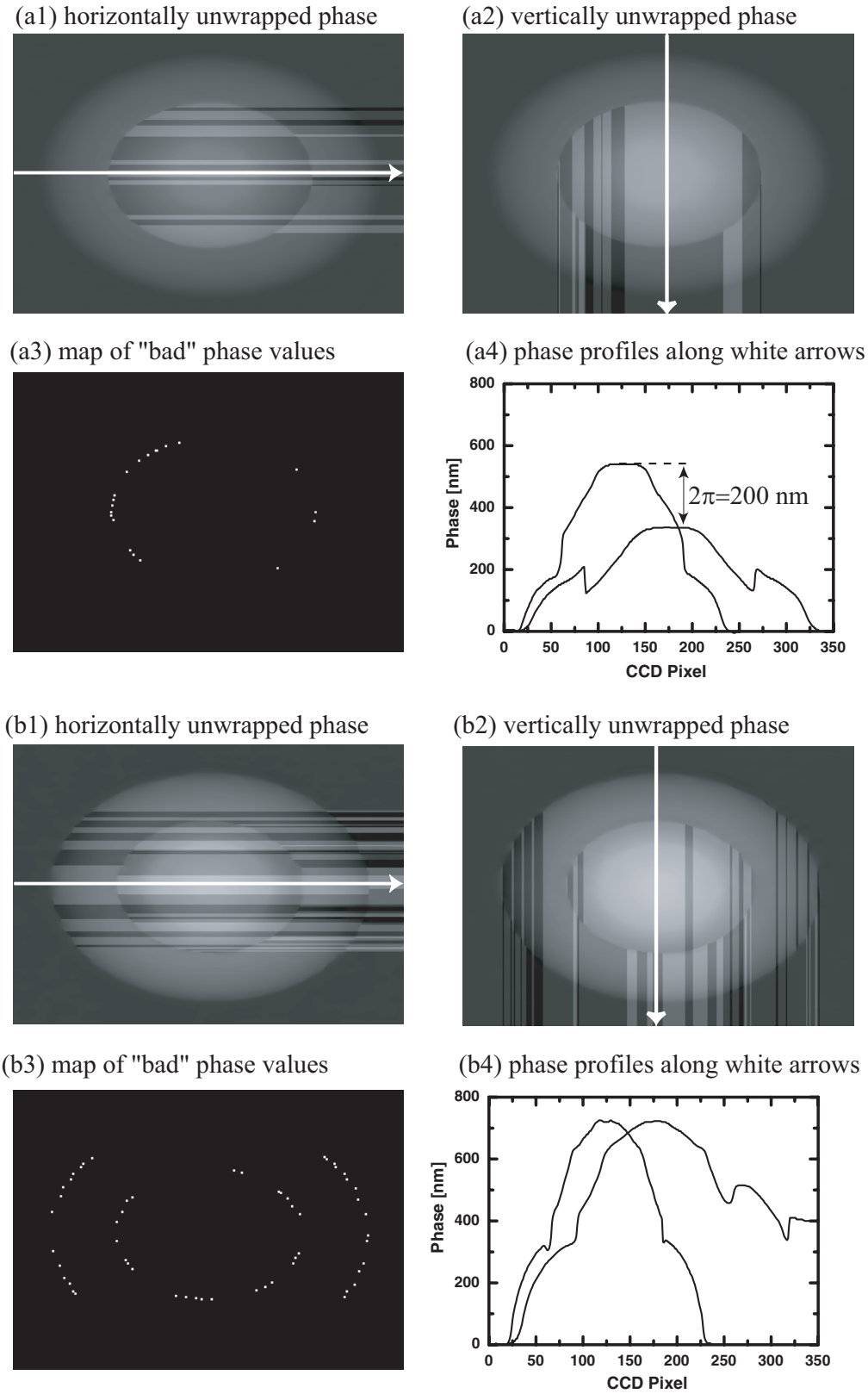

Figure 10: Transient phase surfaces of Fig. 8 unwrapped line-by-line in different directions, their so-called "consistency check" and phase profiles unwrapped in different directions (see text for details).

the phase map with phase values at three neighboring points. An artificial sequence of five phase values $p_1 = p_{x,y}, p_2 = p_{x+1,y}, p_3 = p_{x+1,y+1}, p_4 = p_{x,y+1}, p_5 = p_{x,y}$ is unwrapped. If p_5 differs from p_1 after unwrapping, all four pixels are marked as containing "bad" phase values. These "bad" phase values are called aliasing-induced dislocations in the jargon of interferometric community [30].

Figures 10(a3,b3) show the positions of aliasing-induced dislocations values for phase maps (a1,b1). As expected, there are again far more dislocations in (b3) as compared with (a3). The second and most important observation is that the dislocations lie on one or two elliptical rings around the center of the laser excited area, where the spatial gradient of the phase is very big.

By using the knowledge of where the dislocations come from and exploiting the elliptic symmetry we have developed our own unwrapping algorithm. It is illustrated in Fig. 11. Extensively analyzed transient phase maps (a1,b1) are unwrapped along elliptical paths line-by-line starting from the center of the laser excited area (a2,b2). This part of the unwrapping algorithm requires knowledge of the exact position and eccentricity of the laser-excited elliptical area on the sample. These parameters are determined fully automatically from the analysis of final ablation craters, as already discussed previously (see Fig. 9(c6)). The residual problems with unwrapping manifest themselves in Fig. 11(a2,b2) as a few dark and bright elliptical rings. The position of these rings does naturally correspond to aliasing-induced dislocations of Fig. 10(a3,b3). Any cross-section of phase maps (a2,b2) not presented here appears to be symmetric and continuous except for a few multiples-of-2π phase jumps at the position of the rings. To get rid of these still annoying phase discontinuities we would like to stress the obvious fact that elliptically unwrapped phase maps (a2,b2) look optically much better as compared to (a1,b1). This is why we decided to use the so-called bandlimit approach (global feed-back): "the approach is anologous to a human observer adding arbitrary phase step function to the wrapped data until the result appears smooth and continuous for the eye"[29].

We have called this method *Fourier unwrapping*, because it involves manipulations with the Fourier transform of the phase map. Our iterative implementation of the algorithm consists of several steps. First, the elliptically unwrapped phase map (a2) is Fourier-transformed. The Fourier transform contains high frequency components induced by a few 2π-phase jumps on elliptical rings with phase dislocations. High-frequency components in Fourier spectra are removed by spectral filtering. The inverse Fourier transform of such filtered spectra generates a smoothed phase. The smoothed phase is compared with the original one for each pixel: if the phase differ-

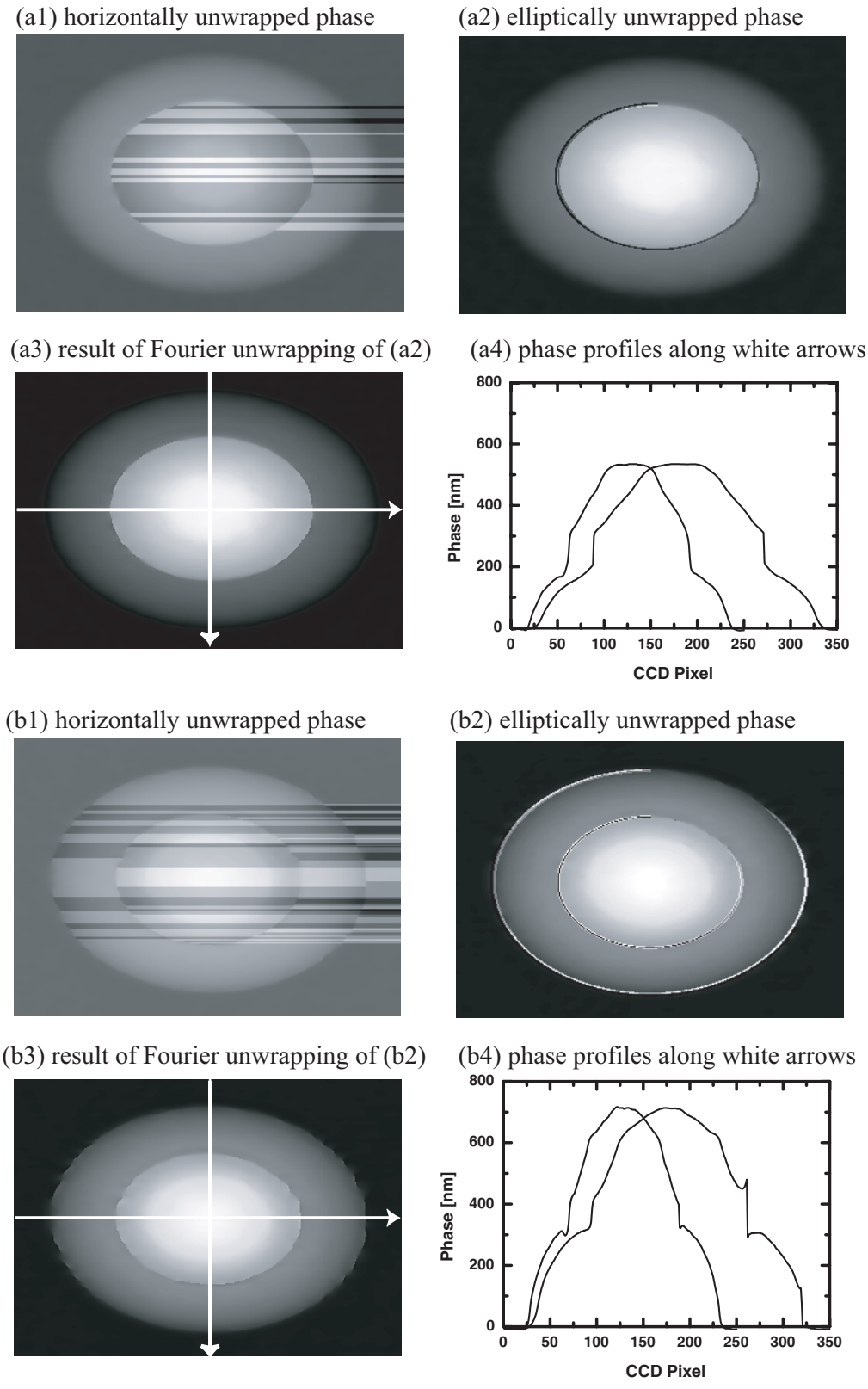

Figure 11: Transient phase surfaces of Fig. 8 (a1,b1) are unwrapped line-by-line along elliptical paths (a2,b2) and subjected to Fourier-unwrapping (a3,b3). Plots (a4,b4) show the profiles of unwrapped phases (a3,b3).

ence is larger than π then a multiple of 2π is added to the original phase to minimize the difference, otherwise the original phase remains unchanged. This procedure is repeated several times to generate the phase maps, presented in Fig. 11(a3,b3). Note that in order to generate phase maps (a3,b3) from phase maps (a2,b2) no image processing has been applied except for adding multiples-of-2π at a few pixels. Fourier-unwrapped phase maps indeed appear to be smooth and continuous to the eye; only a few points corresponding to "bad" phase values indicate that there were unwrapping problems.

Vertical and horizontal spatial profiles of Fourier-unwrapped phase maps (a3,b3) are presented in (a4,b4). In graph (a4) the vertical and horizontal profiles appear to be perfectly identical. The maximal observed phase shifts in the center of the laser-excited area are much larger than π and, therefore, are mostly induced by positive surface excursion. The maximal surface excursion in (a4) is around 500 nm. In graph (b4) some small errors due to aliasing still can be recognized at the points where negative phase jumps existed in Fig. 10(b4). They cannot be removed in principle, but they are small. Graph (b4) suggests that the maximal surface excursion is approximately 700 nm. However, the physically expected continuous in time surface motion (the corresponding experimental data will be discussed in the next chapter) requires that the maximal surface excursion at 3.3 ns must be around 900 nm. Thus it can be concluded that even after successful unwrapping we still miss one phase jump of 2π in (b4). Inspection of temporal evolution makes it evident at which points the missing multiples-of-2π should be added.

Despite all the discussed ambiguities and problems of interferometric measurements the extracted phase information can be considered as quite reliable because phase errors are mostly reduced to missing 2π-phase jumps and we know where they should be added. This is in contrast to the reconstructed reflectivity maps!

2.4.4 Are the reconstructed reflectivity maps correct?

Figure 12 compares the reconstructed surface reflectivities of Fig. 8(a5,b5) and Fig. 9(c5) with those directly measured by time-resolved microscopy for equal delay times and excitation conditions. The directly measured reflectivities are different from reconstructed ones. The difference between (a1) and (a2) but also (b1) and (b2) is quite apparent: the reconstructed reflectivities contain more dark areas (corresponding to lower reflectivity) as compared with those measured directly. To explain this difference we shall again refer to the problem of aliasing or "energy leakage". Energy conservation law in mathematics is formulated in terms of the Parce-

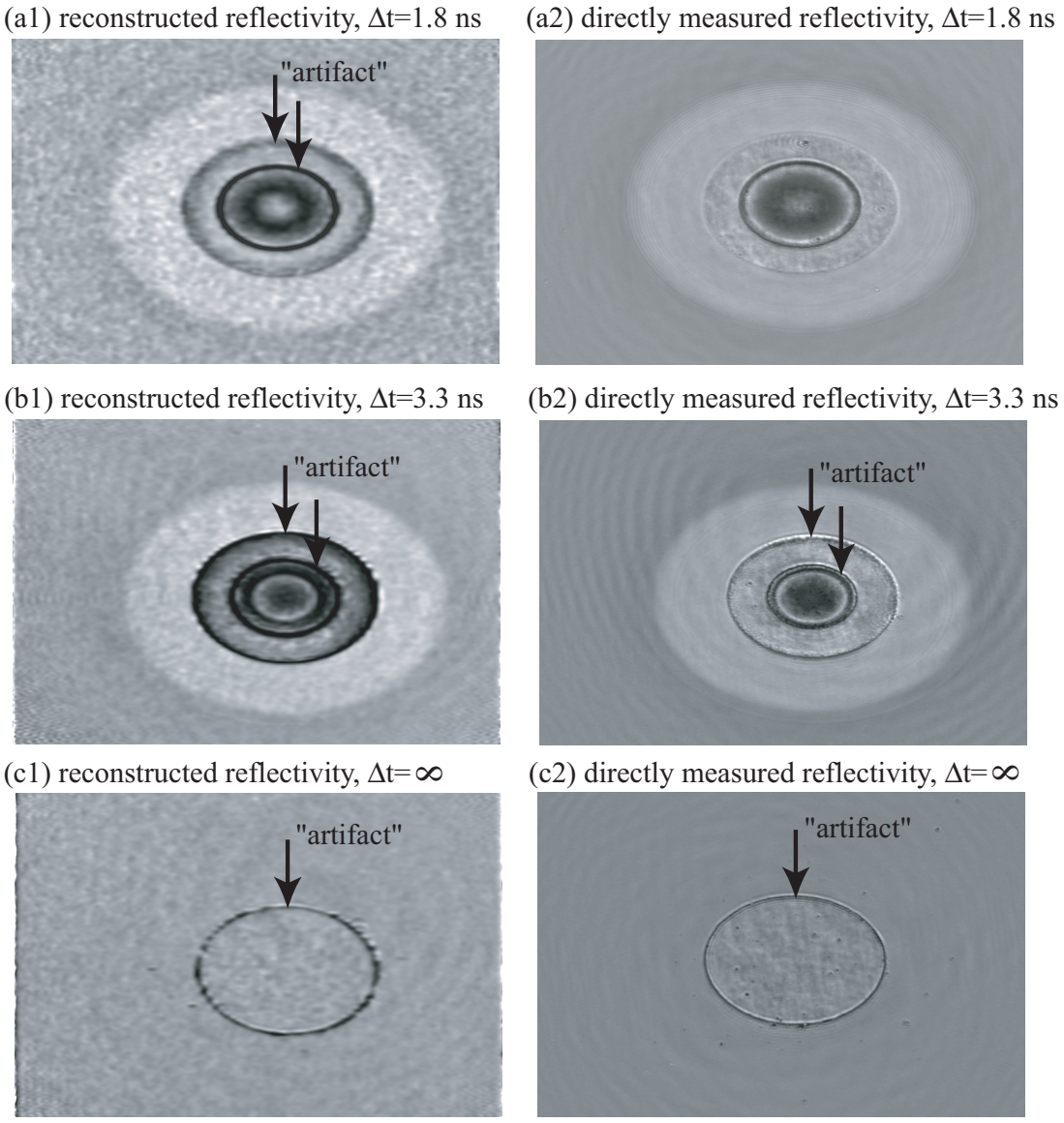

Figure 12: Comparison of reconstructed surface reflectivities of Fig. 8 and Fig. 9 with those directly measured by time-resolved microscopy; GaAs, $F = 1.3\ F_{thr}$.

val's theorem: integral of squared signal in coordinate space is equal to integral of squared Fourier spectra in frequency domain. Since some frequency components of the signal can be cut by (i) numerical aperture of the microscope objective and (ii) artificial spectral filtering, the reconstructed reflectivity should be smaller than the real one. Black pointers in Fig. 12 named "artifacts" show the structures which are either strongly different from, or have nothing to do at all with the actual surface reflectivity. We are sure that (a2) represents the only map in Fig. 12 that corresponds to real surface reflectivity, because we do not see any signatures of cut-off by the numerical aperture of the microscope objective (see the Fourier spectra of Fig. 8(a2)).

Thus, all differences in (a1) as compared with (a2) can be considered as artifacts. The argumentation for plots (b1) and (b2) is similar except for the fact that some spectral frequency components are already cut by the microscope objective (see the Fourier spectra of Fig. 8(b2)). For this reason we do also mark the two dark rings in (b2) as artifacts. Note that the two marked black rings in (a1), (b1) and (b2) correspond to the areas with the highest spatial gradient of the phase (or, gradient of surface position). The maximum tilt angle of the ablating surface with respect to the unexcited surface, which can be roughly estimated from presented spatial phase profiles of Fig. 11(b4) is of the order of 10 degrees, which is comparable with the opening angle of the microscope objective of about 17.5 degrees. Therefore some rays coming from the microscope objective do not enter the objective aperture after reflection from strongly tilted surface areas, leading to the formation of conspicuous dark rings, which have nothing to do with actual surface reflectivity.

The same type of argumentation holds for reflectivity images of the final surface (c1) and (b1). Direct microscopic studies of ablation craters, to be discussed in the next chapter, show that the crater boundary corresponds to an extremely sharp spatial variation of the surface profile, corresponding to the true phase jump in our discussion. We have also verified by very simple computer simulation that a pure phase jump in the object plane generates an artificial reflectivity decrease in the image plane when imaged by an ideal microscope objective with finite numerical aperture.

In order to verify the above conclusions we have compared the directly measured reflectivity profiles with those obtained using spectral filters of different shapes and sizes for several interferometric data sets. Not only the size but also the shape of the spectral filter is found to be important. In case of strong spatial reflectivity modulations or phase gradients the reconstructed reflectivity maps are always some that different from direct reflectivity measurements. Correct values of surface reflectivity are obtained only in the case of smooth spatial dependencies of reflectivity and phase.

2.5 Conclusions and future perspectives

In this chapter different aspects of imaging time-resolved interferometry were presented and discussed. Particular attention was paid to the formation of interferograms in the Linnik microinterferometer, which plays an important role for the understanding and correct application of the 2D-Fourier-transform algorithm for phase and amplitude reconstruction. Important aspects of the physical interpretation of

interferometric measurements have been discussed using the experimental data for a fs-laser excited GaAs-surface excited below and above the ablation threshold. A rather general analysis of the complex reflection coefficients within the frame of the simple Fresnel formula makes it possible to significantly reduce the intrinsic ambiguity of single-wavelength interferometric measurements and clearly identify geometric surface deformations with amplitudes of a few tens of nanometers. This result appears to be very important for the physical interpretation of interferometric measurements to study femtosecond laser ablation. Another important set of questions, which has been extensively investigated deals with phase unwrapping algorithms and their failure in certain cases. Phase measurements are found to be quite reliable, whereas major phase errors represent multiples-of-2π jumps, which can be easily recognized and removed both manually and by using fully automatic algorithms. In contrast, the reflectivity maps reconstructed from the interferograms exhibit a lot of artifacts, which cannot be eliminated. The comparison of reconstructed and directly measured reflectivity maps (by means of time-resolved microscopy) allowed us not only to reveal the properties and the importance of such artifacts but also to identify some artifacts in directly measured images. A straightforward explanation for all these observations is provided by considering the imaging with a microscope objective with finite numerical aperture and application of additional spectral filtering during interferogram processing.

It should be stressed that imaging two-beam interferometry (in reflection) represents a sensitive and reliable technique for phase measurements, whereas the accompanying information about surface reflectivity usually contains artifacts. Some more details and the analysis of imaging Mach-Zehnder-type interferometry (in transmission) will be discussed in Chapter 4, which deals ultrafast optical measurements in laser-excited dielectrics.

The applied 2D-Fourier-transform algorithm for phase reconstruction is relatively simple, numerically efficient and widely used. However, the novel methods utilizing the concept of *wavelets* offer big advantages over the Fourier-transform-based algorithms [31]. Whereas the Fourier transformation represents a decomposition of an arbitrary function in a set of delocalized plane waves, wavelet transformation utilizes also oscillating but localized basis functions with zero mean (this is essentially a general definition of wavelets). Some of the big problems with wavelets are that there are many of them, they are very different and most of them cannot be represented by analytical functions. According to our knowledge the only attempt to apply the concept of wavelets to a physical problem was made by L. Onural in

his paper "Diffraction from wavelet point of view" [32] (see also the successive critical discussion and comments [33]). The application of a discrete wavelet transform for interferogram processing demonstrates a significant improvement of performance according to the figures and figure captions in [34] (the rest is unfortunately in Chinese). According to our knowledge of the outstanding computational performance of wavelets, we believe that their application to physical problems represents a new and very promising direction for future research.

3 Femtosecond laser ablation

As already mentioned in the introduction the two highly interesting features of femtosecond laser ablation of absorbing surfaces such as metals and semiconductors are (i) the sharp ablation threshold and (ii) the specific internal structure of the ablating layer, which gives rise to the observation of a transient optical interference pattern (Newton rings) during laser ablation. The main issue of this investigation is to clarify the basic physical mechanisms responsible for the sharp threshold and gain some experimental evidence about the actual internal structure of the ablating layer. This section is organized as follows. Some results on comparative characterization of ablation craters provided by different types of microscopy show final surface morphology near the ablation threshold in typical semiconductors GaAs and Si. These data aim to demonstrate the actual sharpness of surface structures at the ablation threshold, which appears to be far below the resolution limit of the optical microscopy. Then the basic ideas about the mechanisms of femtosecond laser ablation are discussed and the two very distinct models for the internal structures of ablating layer are presented. The main experimental results deal with time-resolved interferometric measurements of transient deformations of laser-excited GaAs and Si-surfaces both above and below ablation threshold and their physical interpretation.

3.1 Sharp ablation threshold and internal structure of ablating layer

3.1.1 Morphology of ablation craters in GaAs and Si

In this section we report on a detailed microscopic investigation of the morphology of GaAs(100) and Si(100) surfaces irradiated by single intense femtosecond laser pulses with fluences slightly above the ablation threshold. As in the previous investigations of the dynamics of laser ablation [1, 2], laser fluences below 1 J/cm^2 are used to initiate the ablation process. Note that the applied moderate laser fluences are not large enough to directly ionize the solid. Thus, we do not consider laser ablation in the so-called plasma regime, which has been investigated very extensively.

The application of the optical differential interference contrast (DIC) and interference microscopy, atomic force (AFM) and scanning electron (SEM) microscopy to the same object, i.e. the ablation crater, provides the complete information about its structure. Starting from the global "macroscopic" overview of the surface area affected by a laser pulse we "zoom in" into the particular characteristic surface regions and study their "microscopic" structure. In this manner a complete characterization

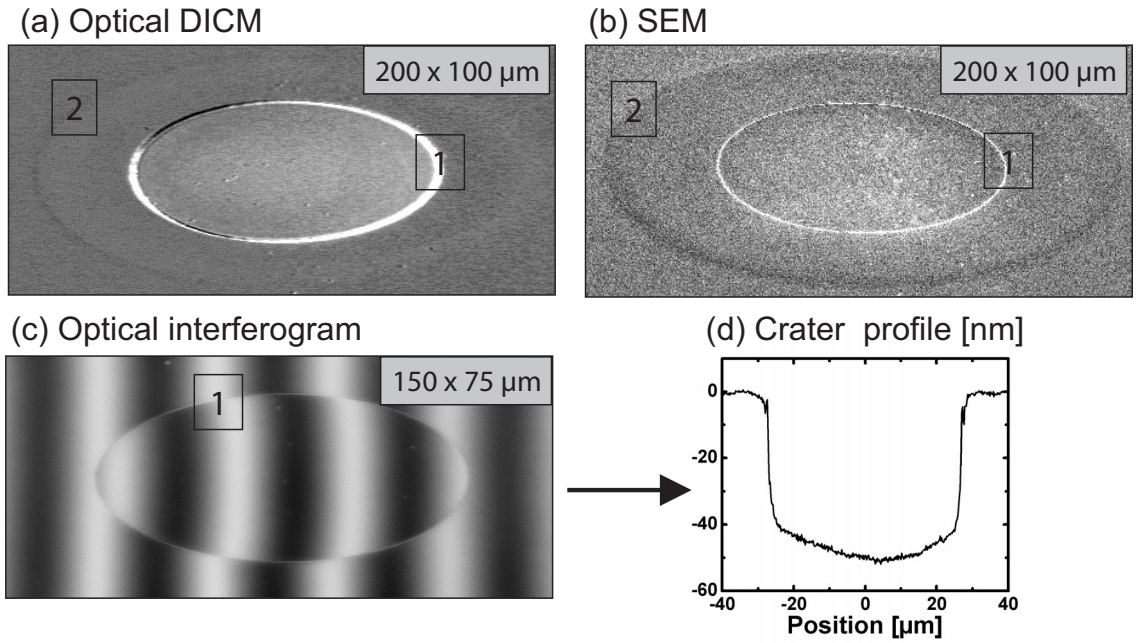

Figure 13: An overview of the ablation craters on GaAs, $F = 1.4\ F_{thr} = 0.3$ J/cm^2. The boundary of the ablation crater and the outer ring are marked by numbers 1 and 2, correspondingly (see text for details).

of the final surface morphology has been performed: starting from the center of the ablation crater to the region outside of it where the material was not ablated but only molten by the laser pulse.

As samples of crystalline GaAs(100) and Si(100) we used small pieces of commercially available wafers (typically 3 or 4 inch in diameter) made by breaking the wafers along their crystallographic directions under mechanical load. After that several identical samples were positioned on a motorized x-y stage and irradiated by femtosecond Ti:Sa laser pulses in the air. The p-polarized laser pulses with a width of 100 fs at λ=800 nm and energy up to 1 mJ were focused on the sample by a lens with long focal length (f=50 cm) under angle of incidence of approximately 45 degrees. The laser focus on the surface of the sample had a Gaussian intensity distribution (150x75 μm FWHM). While the motorized stage was moving in one direction with properly adjusted constant velocity the laser running at 10 Hz repetition rate produced many identical ablation craters on fresh sample areas. The equal spacing between the craters was large enough to avoid any overlap between different laser-modified surface spots. In this manner several samples containing many identical ablation craters could be prepared very quickly and were investigated later by means of the AFM, SEM and optical microscopy. The process of crater production was controlled in real time by imaging of the sample surface on a CCD-camera.

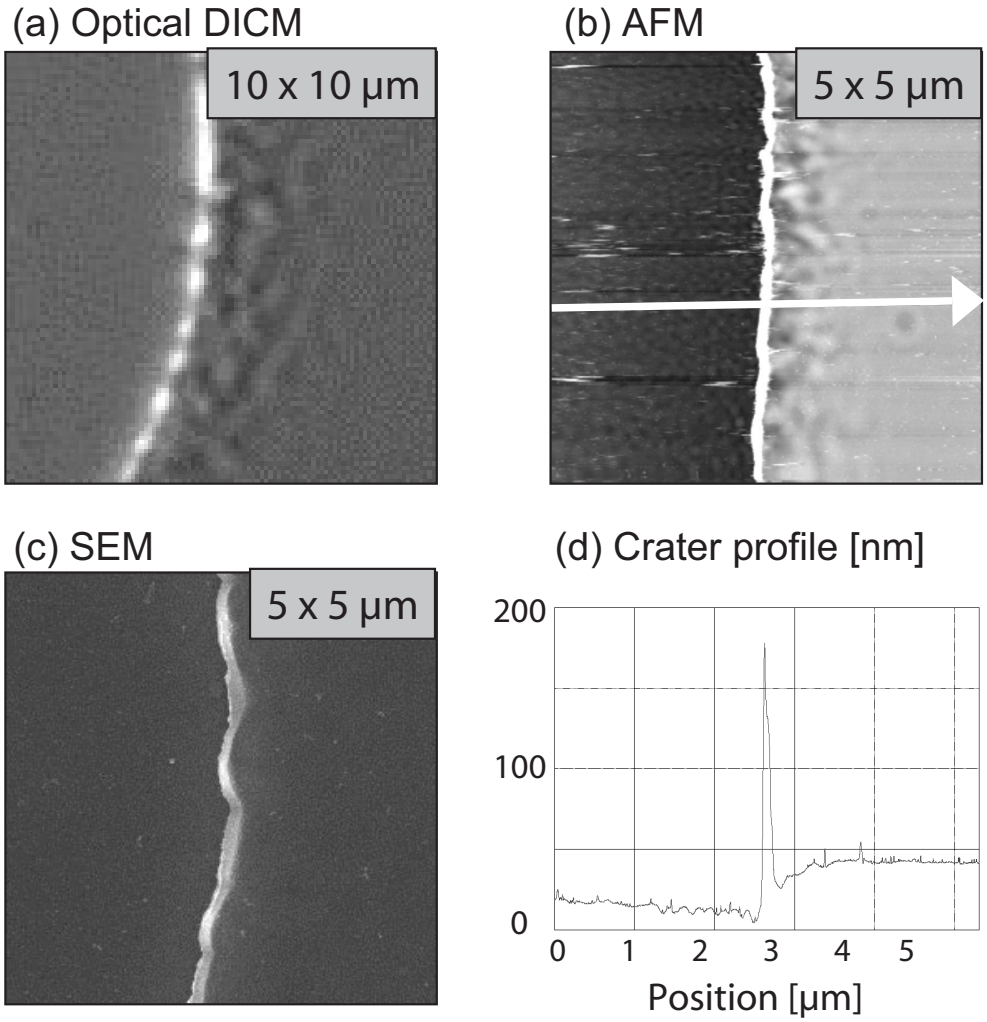

Figure 14: Boundary of the ablation craters on GaAs, $F = 1.4\ F_{thr}$. The crater is on the side left of the boundary.

An overview of the ablation crater on GaAs(100) produced by single femtosecond laser pulse with fluence forty percent above the ablation threshold, $F = 1.4\ F_{thr} = 0.3$ J/cm^2 is presented in Fig. 13. The two rings can be seen in the crater images provided by both the optical DIC-microscopy (a) and the SEM (b).
The inner bright, well-pronounced ring in the DIC and SEM images represents the boundary of the ablation crater. In the optical interferogram (c) the crater boundary manifests itself in the jump of the interference fringes indicating that a part of the material is removed from the initially flat surface. The quantitative analysis of the optical interferogram (c) allows the reconstruction of the actual crater profile (d), which clearly demonstrates the threshold character of laser ablation. Whereas just above the ablation threshold a 40-nm thick layer of material is removed, just below the threshold no material removal can be detected interferometrically. Considering

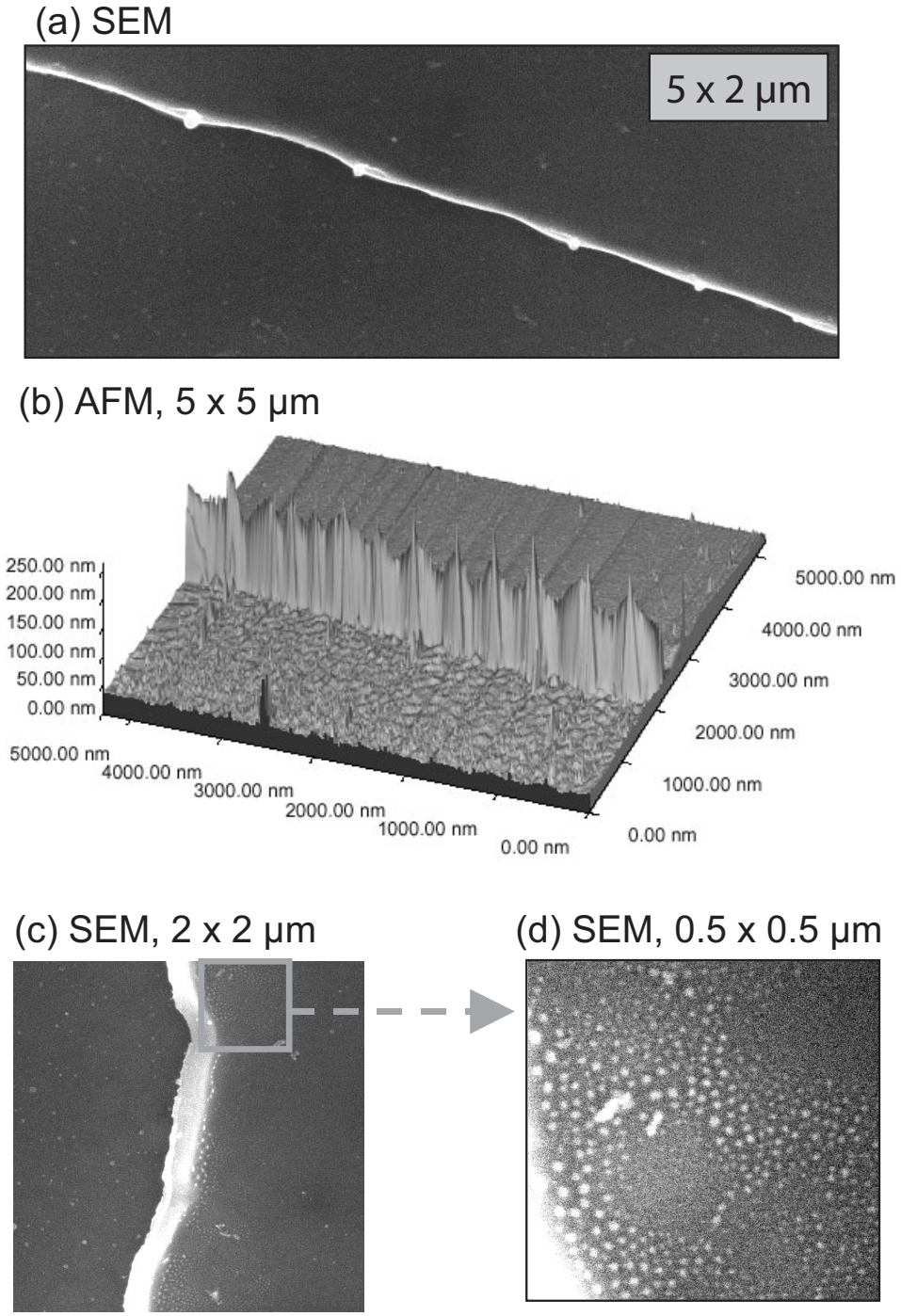

Figure 15: Fine structure of the crater boundary on GaAs, $F = 1.4\ F_{thr}$.

the Gaussian laser fluence distribution on the surface it can be shown that the variation of laser fluence in the threshold region is far below 1%. Except for the sharp boundaries the ablation crater appears to be relatively flat: its depth shows only a weak dependence on the laser fluence approaching the value of 50 nm in the center of the crater.

The second, less pronounced outer ring is only characterized by minor reflectivity changes in both DIC and SEM images and most likely represents the amorphous GaAs, which can be formed during the rapid cooling down and resoldification of laser-molten material due to thermal conductivity. There are no indications of material removal between the crater boundary and the outer ring from the optical interferograms. The detailed understanding of the conditions under which the resoldification process evolves via recrystallization or amorphization was developed by Bloembergen and co-workers [35].

As already mentioned in the introduction, one of our goals was to provide a microscopic characterization of the boundaries of the ablation crater. The desired information can be inferred from Fig. 14, where the DIC (a), AFM (b) and SEM (c) images of the crater boundary on GaAs are presented. The profile across the crater boundary as provided by AFM (d) shows that it consists of a high and narrow rim. The rim has a height of approximately 150 nm and an extremely small lateral extension of 50-100 nm. The surface outside the crater (right) is characterized by a very fine surface waviness localized in the vicinity of the rim, which can be clearly seen in the AFM image (b).

Fig. 15 shows some irregular structures on the crater boundary. The SEM (a) and AFM (b) images of Fig. 15 show a part of the rim with several sharp needles with a height above 100 nm and diameter about of approximately 50 nm, which appear to be quite regularly spaced on the rim. We could observe these needles only on some AFM and SEM images, very often they are completely absent. The SEM images (c) and (d) show further nanostructures in the vicinity of the rim, which have typical lateral dimensions of 20 nm. Like the needles, these structures also appear to be statistically distributed along the rim.

The ablation craters produced on Si (100) surface by laser pulses with fluence $F = 1.4\ F_{thr} = 0.49$ J/cm^2 have been subjected to the same analysis as the craters on GaAs.

An overview of the ablation crater is shown in Fig. 16. The images look a little bit different as compared to GaAs. Nevertheless, the boundary of the ablation crater, which can be easily seen in the optical DIC image (a) can be also recognized in the SEM (b) image and the optical interferogram (c). The crater profile (d) reconstructed from the optical interferogram appears to be very shallow. The crater depth is about 7 nm at the crater boundary and decreases with increasing fluence approaching the minimal value of approximately 5 nm in the center of the crater. This unusual behavior is consistent with the previous measurements of crater profiles

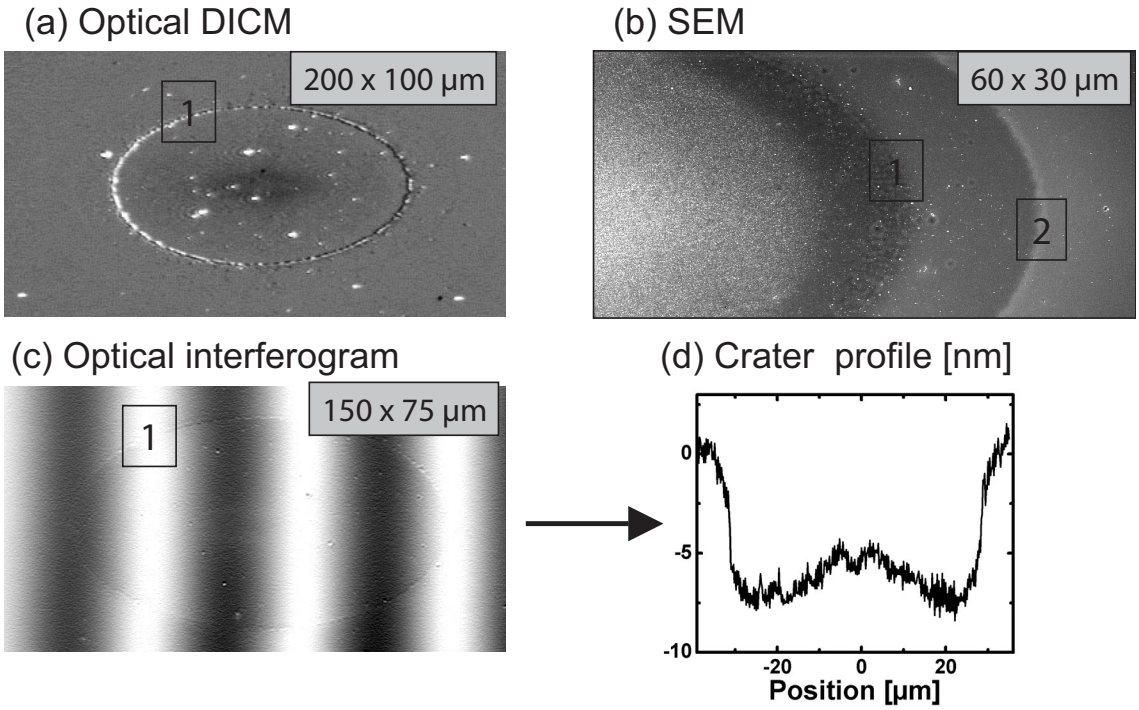

Figure 16: An overview of the ablation craters on Si, $F = 1.4\ F_{thr} = 0.49$ J/cm^2. The boundary of the ablation crater and the outer ring are marked by numbers 1 and 2, correspondingly (see text for details).

on Si(111) by means of a profilometer [36]. The author observed the formation of the "hill" in the center of the crater at higher laser fluences, i.e. the surface in the center showed an excursion with respect to an undisturbed surface indicative for the formation of low density and probably porous material [36]. According to our measurements the reflectivity in the center of the crater in the DIC (a) and SEM (b) images is also very different from that of crystalline or amorphous silicon.

All above observations suggest that the final surface modification of silicon surface by ultrashort laser pulses in the air are quite different from GaAs. Nevertheless, a detailed inspection of the crater boundary on silicon in Fig. 17 reveals some important common features. The crater boundary appears to be well-pronounced in the DIC (a), AFM (b) and SEM (c) images. The AFM data show that the crater boundary also consists of a rim with a lateral extension of approximately 300 nm; it can be also inferred from the AFM image (b) that the height of the rim oscillates quasi-periodically along the boundary. We were also able to see this periodicity in many optical images. The height of the rim changes significantly; it reaches values of up to a few tens of nanometers as shown in (d), but the average height of the rim is only about 10 nm. As in the case of GaAs a small surface waviness can also be

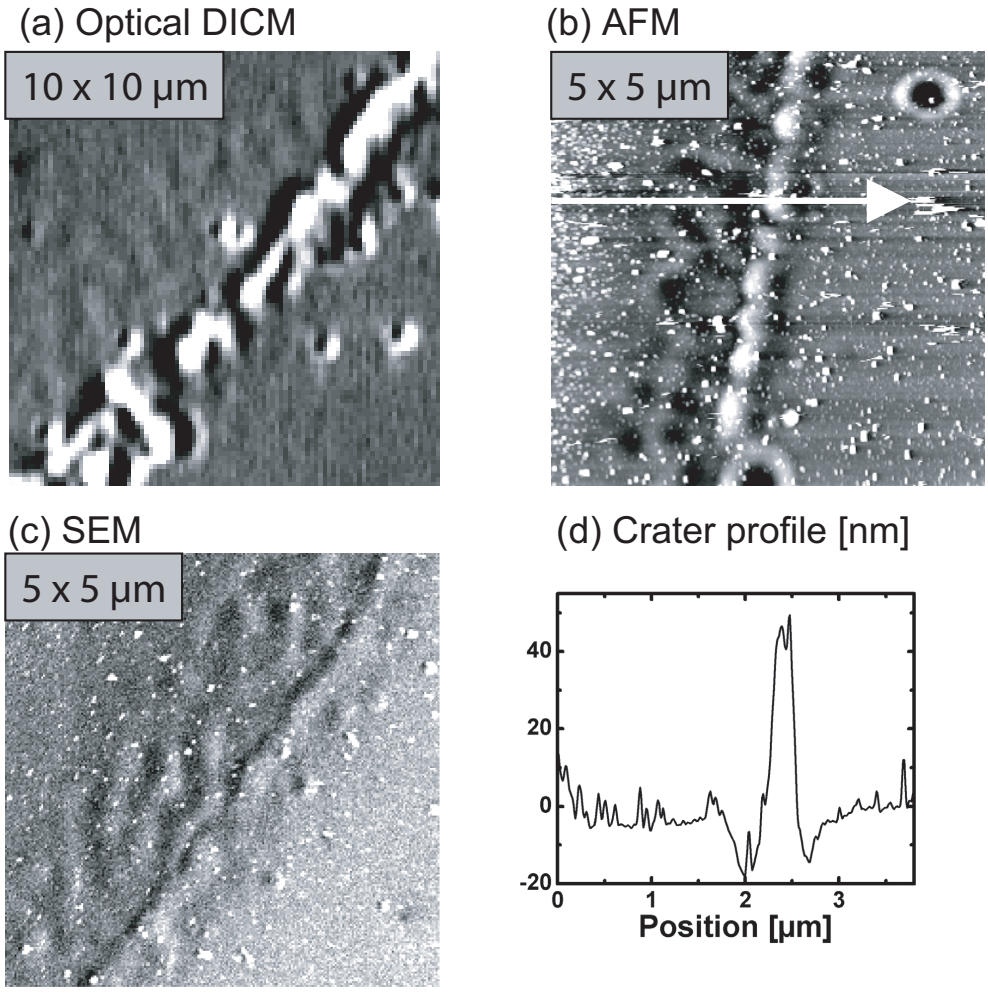

Figure 17: Boundary of the ablation crater on Si, $F = 1.4\ F_{thr}$. The crater is on the left side from the boundary.

seen on Si, Fig. 17(b,c). From a first glance it seems to be surprising that surface waviness appears inside the crater (left from the boundary), whereas on GaAs it was outside. A more careful crater inspection on GaAs allowed us to detect some fine surface waviness of the crater bottom too.

The results of the above analysis reveal some differences in crater morphology on two investigated materials but also some very important common features of the crater boundaries.

The main result of the presented microscopic investigation is that for both gallium arsenide and silicon the boundary of the ablation crater consists of a high and narrow rim. Whereas for GaAs the rim is very high (∼150 nm) and extremely narrow (∼50-100 nm), for Si it is significantly lower (∼10 nm) and broader (∼300 nm).

The second observation is that the ablation craters on both GaAs and Si are rela-

tively flat, i.e. their depth is a slowly varying function of the applied laser fluence. It should be pointed out that the morphology of ablation craters produced on GaAs, Si, and InP surfaces by tightly focused femtosecond laser pulses (beam waist in focus 6x6 μm FWHM) [37] is qualitatively different from our observations. The reported crater shape is very similar to that known for nanosecond laser ablation [38], where the so-called "piston" mechanism of melt ejection by the evaporation recoil pressure determines the final crater morphology. In the case of femtosecond laser ablation the recoil pressure provided by the ablating material under conditions of tight focusing could probably also lead to the high transverse pressure gradients followed by melt ejection. Thus, the influence of focusing conditions upon the mechanisms of final crater formation is a subject of further investigation.

3.1.2 Two models of the internal structure of an ablating layer

Besides the sharp ablation threshold there is another striking feature of femtosecond laser ablation, which manifests itself as the formation of a transient optical interference pattern (Newton rings) within the ablating area on a nanosecond time-scale. Any model for the internal structure of an ablating plume requires that a sharp ablation front is formed so that the incoming probe light reflected from it can interfere with light reflected from the back surface of the non-ablating material. Two such models have been proposed to explain the remarkable interference phenomenon: a simple spatially homogeneous structure [1] and some more complicated spatially inhomogeneous "bubble-like" structure [2], which are sketched in Fig. 18.

Both models assume that a hot pressurized superficial layer of liquid material is created within a few picoseconds after laser excitation, before the material removal starts. The thickness of the liquid layer depends on material parameters, the properties of the pump pulses and, of course, on the mechanisms of light absorption by the electrons and their coupling to the lattice. For a typical semiconductor the thickness of the laser-molten layer is of the order of a few tens of nanometers [39]. A hot liquid material starts to expand towards the vacuum and is removed from the surface leading to the formation of final ablation craters. It is known from time-of-flight mass spectrometry measurements that the final state of the ablating material is a weakly ionized volatile gaseous phase containing single atoms and small atomic clusters [40]. Therefore during the expansion a part of initially high-density liquid film is converted into a low-density gaseous phase via liquid-gas phase transition, passing through different non-equilibrium states of matter. The lack of knowledge about how and where the phase transition occurs provides motivation to consider

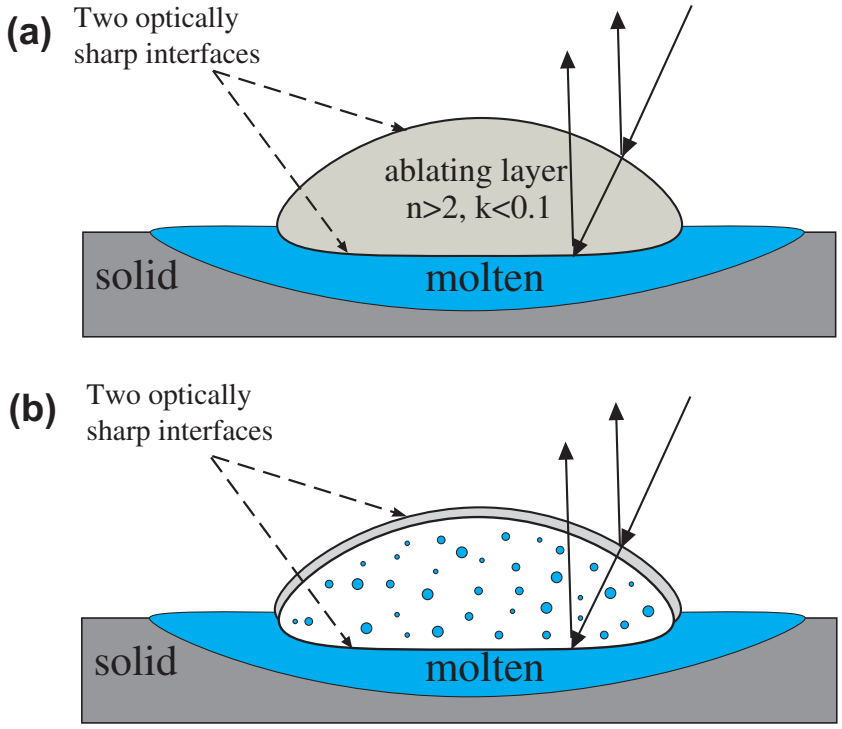

Figure 18: Two models for internal structure of ablating material, which are capable of explaining optical interference phenomena: (a) spatially homogeneous and (b) spatially inhomogeneous "bubble-like" structure.

different models of material removal.

The simple model of Fig. 18(a) assumes that the ablating layer of material remains spatially homogeneous during the expansion, but its density becomes lower with time [1]. To be capable of explaining the observed high-contrast transient interference pattern the material must possess a high refractive index and be optically transparent. At some point the density of the expanding liquid layer becomes so low that it *must* undergo the liquid-gas phase transition and is converted into mixture of two phases: liquid droplets surrounded by vapor (of course, only for the case when the expansion isoentropes enter the liquid-gas coexistence region on the phase diagram [1]). Since the mass density of the two-phase mixture is constant within the ablating layer, it is described by a constant (spatially homogeneous) effective index of refraction. Assuming that the typical sizes of the liquid droplets are small compared to the optical wavelength one can apply a well-known Maxwell-Garnett formula [41] for dielectric response ε_{MG} of such medium and recognize that it can indeed possess a high refractive index and low absorption coefficient [1]:

$$\varepsilon_{MG}(f) = \varepsilon_g\left(1 + \frac{2f\Lambda}{1 - f\Lambda}\right) \quad \text{with} \quad \Lambda = \frac{1}{\varepsilon_l}\frac{\varepsilon_g - \varepsilon_l}{\varepsilon_g + 2\varepsilon_l}\,. \tag{20}$$

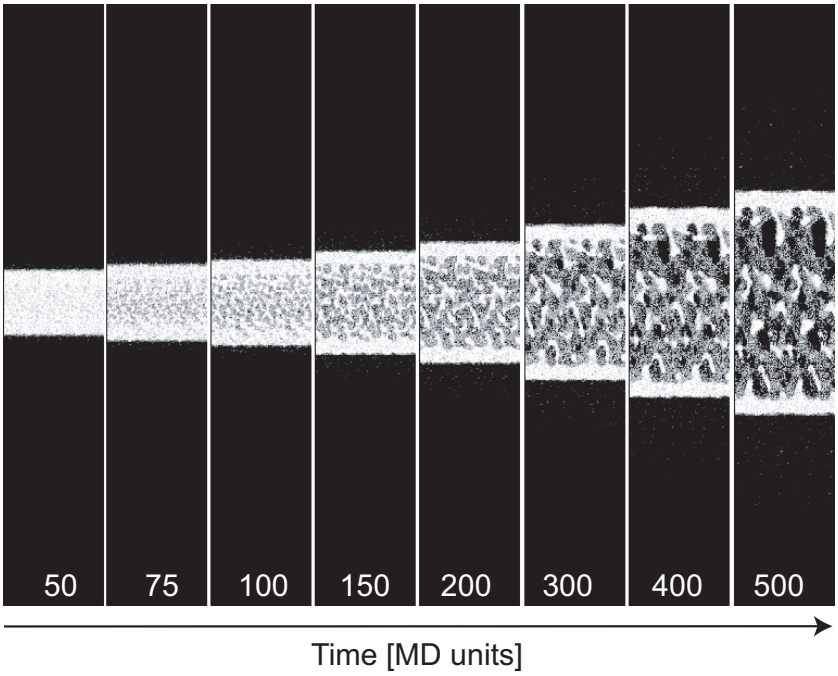

Figure 19: Molecular dynamics simulation for one-dimensional expansion (in vertical direction) of a hot pressurized liquid film, which simulates the conditions of femtosecond laser ablation. Time-scale is provided in dimensionless MD units (see text for details).

Here ε_l and ε_m stand for dielectric functions of gas and liquid, respectively, whereas the very important filling factor f $(0 < f < 1)$ is equal to the volume fraction of the liquid phase in the two-phase mixture. The necessary requirement for a high refractive index is that the filling factor f is quite high, $f \sim 0.5$, which breaks down in the later stages of expansion when the material density becomes very low and the refractive index becomes close to unity according to Maxwell-Garnett. Nevertheless this kind of argumentation had been used to explain Newton rings in earlier publications [1] before the expansion of the liquid layer was modeled by solving hydrodynamic equations for media that can undergo phase transitions [42, 43] and performing molecular dynamics simulations [44]. These theoretical investigations have shown that a more complicated "bubble-like" structure of Fig. 18(b) is developed during the expansion of a hot liquid layer. Fig. 19 shows a sequence of images from molecular dynamics simulations, which follow the dynamics of a hot pressurized liquid film (described by Lennard-Jones interatomic interaction potential) which is allowed to expand in both vertical directions [44, 45]. The initial thickness $2l$ of the film corresponds to 77 atomic layers of Lennard-Jones liquid, the time is provided in dimensionless MD-units: l/c_s=25 MD units, where c_s is the sound velocity in

Lennard-Jones liquid. A thin high-density and stationary liquid shell moves with constant velocity and forms the ablation front, which is followed by the low-density two-phase mixture: liquid droplets surrounded by vapor. The details about both the hydrodynamic solution and the molecular dynamics simulations have been extensively discussed in the past [42, 43, 44].

The very basic idea behind the hydrodynamic calculations is related to the thermodynamic properties of the ablating matter. Fast adiabatic expansion of a hot pressurized liquid layer corresponds to a known evolution of thermodynamic material properties on a pressure-density phase diagram: moving along different isoentropes $S(p, \rho) = const$ (see Fig. 34). The starting point on the phase diagram corresponds to the solid density $\rho = \rho_{solid}$, whereas the initial pressure and temperature values are determined by the amount of absorbed laser energy. For sufficiently high initial value of pressure the expansion isoentropes enter a metastable two-phase region at $\rho = \rho_B$ (ρ_B-density at the binodal), which corresponds to curve (c) in Fig. 34. A metastable two-phase region is bounded by the so-called "binodal" and "spinodal" curves, whereas the thermodynamic properties of matter therein are quite remarkable and give rise to the development of non-equilibrium thermodynamics of phase transitions [46, 47].

The most striking effect is the *drop of the sound velocity* $c_s(\rho) = \sqrt{(\partial p/\partial \rho)_S}$ as an initially homogeneous liquid layer enters the two-phase region at $\rho = \rho_B$. The quantitative description of this phenomena (i.e. drop of the sound velocity) is provided by Landau and Lifshitz in their course on fluid mechanics [48]. The drop of the sound velocity and reflection of the rarefaction waves from the non-ablating material are found to trigger the formation of a "bubble"-like structure [42, 43], whereas a constant mass density of the "bubble" is equal to ρ_B, which is significantly lower than the equilibrium density of a liquid (by factor $1.5 \div 2$ [43, 44]).

The main point concerning the optical properties of a "bubble-like" structure is that optical interference phenomena is due to the reflection from a thin liquid "bubble", which does not significantly change its properties during the ablation process (see Fig. 19). Further, the existence of the interference pattern is independent on how large is the refractive index of the two-phase mixture behind the "bubble". In contrast, if the ablating layer is spatially homogeneous, it might possess a high index of refraction but it should strongly depend on the filling factor f. This striking difference in the optical properties of the two discussed models will be exploited in our experiments to distinguish between them.

3.2 Interferometric measurements at fs-laser excited GaAs-surface

3.2.1 Irreversible dynamics of GaAs-surface excited slightly above the ablation threshold

In this section we shall present the results of interferomertic measurements at an ablating GaAs-surface. As already mentioned in the previous chapter the time- and space-resolved interferomertic measurements provide two-dimensional spatial distributions of amplitude (reflectivity) and phase of probe pulses reflected from laser-excited surface. Reconstructed reflectivity maps could contain a lot of artifacts in case of strong spatial variations of optical properties within the laser-excited area, which is particularly pronounced for excitation above the ablation threshold. For this reason all reflectivity data to be discussed in connection with above-threshold behavior have been directly measured by time-resolved microscopy. Fig. 20 shows the snapshots of surface reflectivity during ablation of GaAs excited with fluence 40% above the ablation threshold for different pump-probe delay times. During the first few picoseconds the reflectivity within the bright laser-excited area reaches the constant value $R_{liquidGaAs} = 0.61$, indicating the melting of the superficial layer of GaAs. A few tens of picoseconds after laser excitation the reflectivity starts to decrease in the center first, then it increases and oscillates further as a function of time. At nanosecond delay times a characteristic ring structure is developed within the ablating area, which is known as Newton interference fringes. These pure reflectivity measurements are supplemented by interferometrically measured transient phase surfaces presented in Fig. 21, whereas the vertical profiles of phase maps for different delay times are shown in Fig. 22. On a nanosecond time-scale the pronounced irreversible excursion of the laser-excited surface is observed, which is associated with the development of a sharp ablation front. Since the observed phase shifts are large compared to π, they are mostly induced by surface deformations and, for this reason expressed in *nanometers* of surface displacement.

The ablation front in the center of the laser-excited area is found to expand towards the vacuum with the constant velocity of about 400 m/s, which can be inferred from Fig. 23. Relatively big error bars in Fig. 23 are due to shot-to-shot fluctuations of laser energy.

The above results are obtained by manual processing of experimental data, which appears to both time-demanding and inaccurate. Much more physically relevant quantitative information can be obtained by fully automatic processing of experimental data within the MATLAB-environment. Most of the data to be discussed

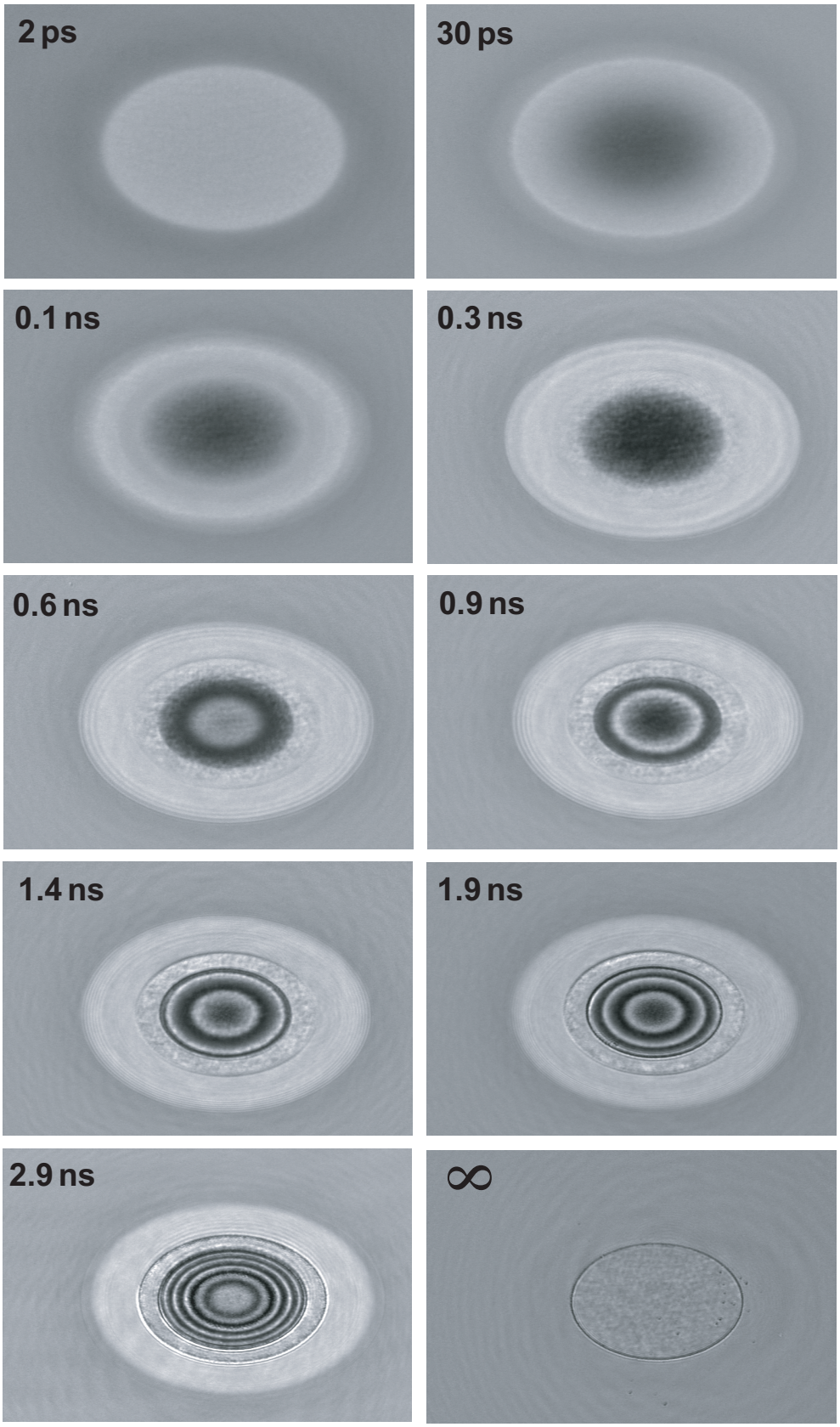

Figure 20: Time-resolved reflectivity snapshots during ablation of GaAs-surface at fluence $F = 1.4\ F_{thr} = 0.3$ J/cm^2.

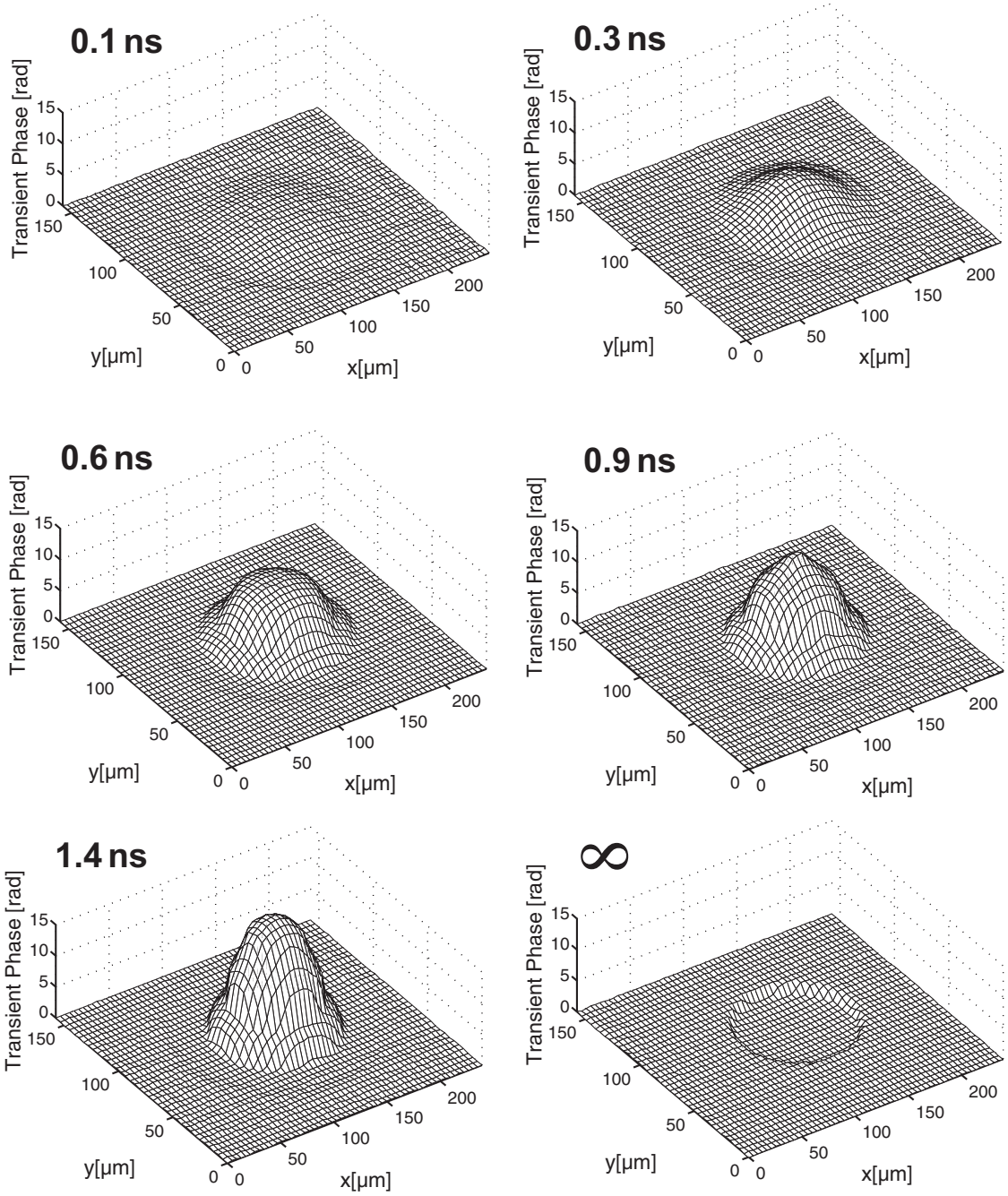

Figure 21: Phase surfaces of ablating GaAs-surface at different pump-probe delay times, $F = 1.4\ F_{thr}$.

further are obtained per button press within several tens of seconds, which allows for a highly efficient and amazing interactive analysis of experimental data.

Some of the tricks concerning data processing have already been discussed in the previous chapter. However, in order not to give the impression that further results are generated by some mysterious image processing, we would like to briefly discuss

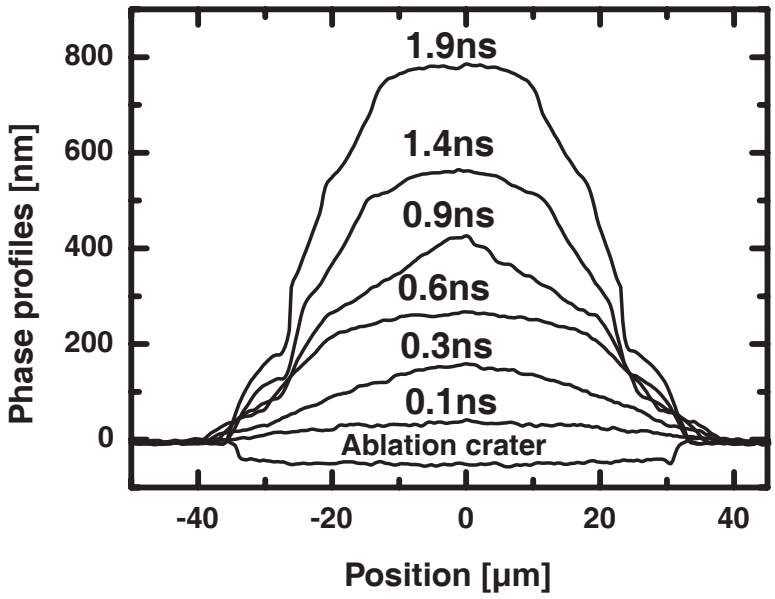

Figure 22: Phase profiles at different pump-probe delay times for GaAs, $F = 1.4\ F_{thr}$.

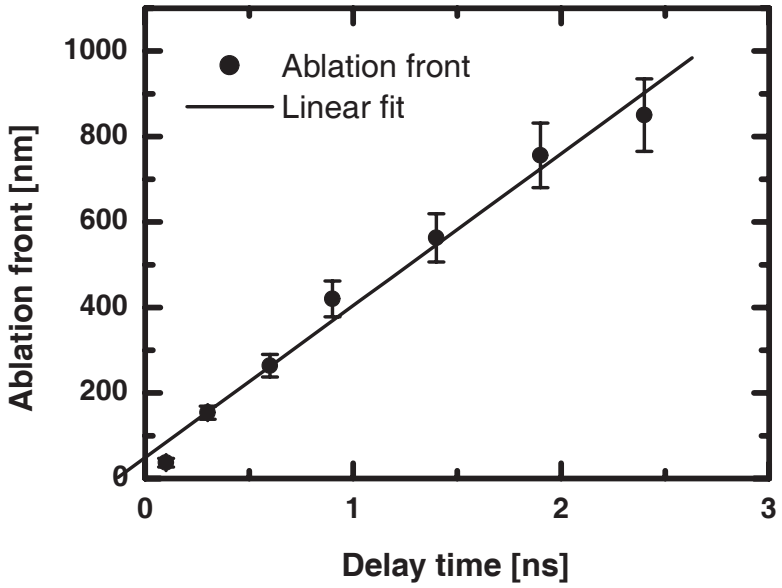

Figure 23: Dynamics of the ablation front for GaAs, $F = 1.4\ F_{thr}$.

the sequence of operations, which are applied to unwrapped phase maps similar to those shown in Fig. 21.

• Spatial fluence distribution at the position of the sample is determined from the analysis of the diameter of ablation craters produced by pulses with different energies (the so-called Liu-method [49]). For a well-adjusted setup the spatial fluence distribution possesses a perfect elliptical symmetry and can be well approximated

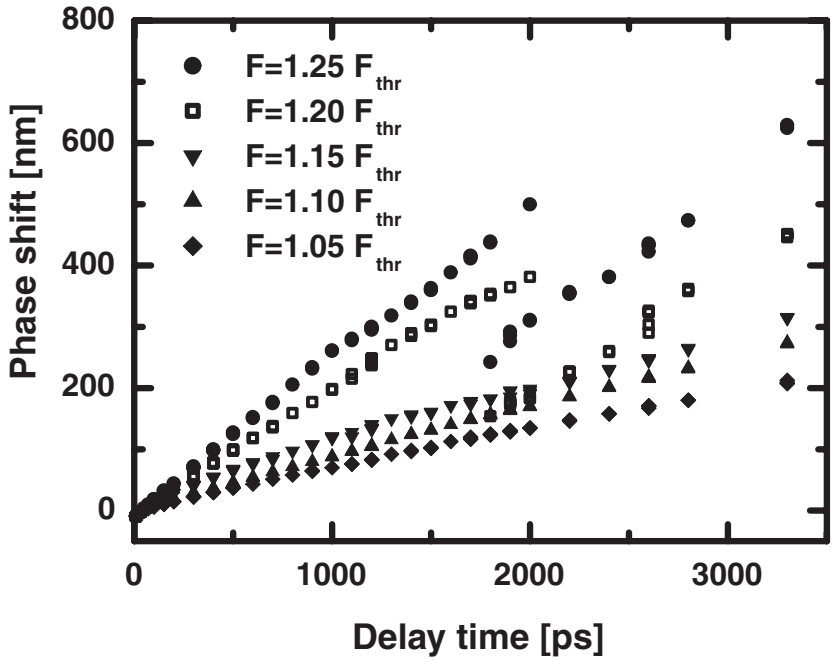

Figure 24: Temporal evolution of ablation front in GaAs for 5 different fluence values exceeding the ablation threshold F_{thr}. The curves represent the result of automatic processing of more than 100 data sets for different pump-probe delay times. Artificial 2π-phase jumps (2π=200 nm) can be recognized in the two upper curves.

by a Gaussian.

• Both pulse energy (energy fluctuations) and the position on the sample (pointing stability) fluctuate from shot to shot, whereas the shape of spatial fluence distribution remains extremely stable. Therefore, for each interferometric measurement the position and size of the final ablation crater is determined as described in the previous chapter. This is enough to precisely know the value of pump fluence for each point within the laser-excited area for each shot.

• Utilizing an elliptical symmetry of spatial fluence distribution, phase profiles are obtained by averaging of phase values over thin elliptical strips centered at the position of the crater. These profiles are similar to those of Fig. 22, but possess a much better signal-to-noise ratio, in particular far from the center.

• Given the peak fluence of the pump pulse the phase shift for *any* smaller value of fluence can be obtained from spatial profiles of the phase.

An example of such fully automatic processing of phase data is presented in Fig. 24, where the time dependencies of the phase for five different fluence values exceeding the ablation threshold are presented. We would like to address two points in discussion of Fig. 24.

First of all, for two highest fluence values $1.2F_{thr}$ and $1.25F_{thr}$ the curves in Fig. 24

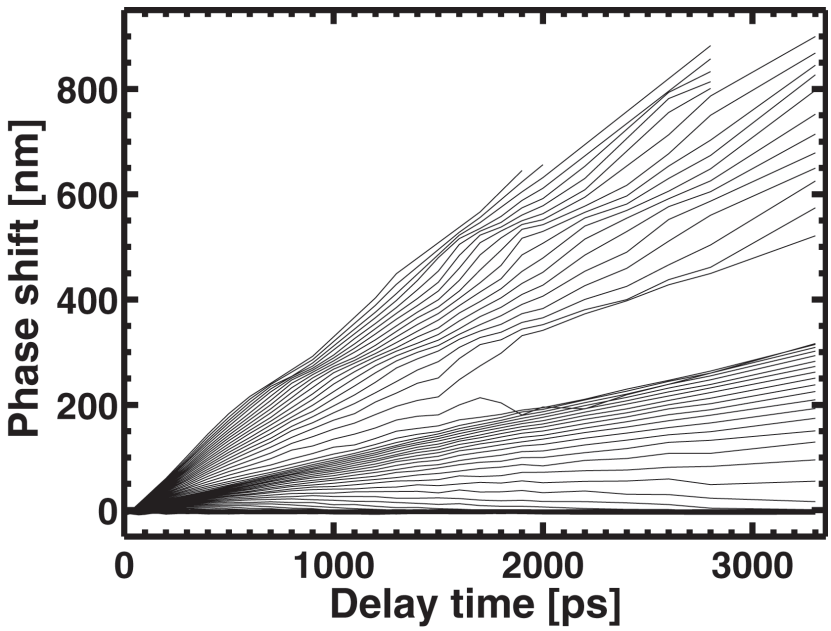

Figure 25: Family of automatically reconstructed temporal phase dependencies for different fluence values $F = 0.25 \div 1.35 F_{thr}$ with fluence step $\delta F = 0.01 F_{thr}$. Artificial 2π-phase jumps in Fig. 24 are automatically corrected.

exhibit artificial 2π-phase jumps (2π=200 nm), which indicate the failure of phase unwrapping algorithm due to extremely sharp spatial gradients of the phase (see the discussion in the previous chapter). Phase curves must be corrected for these artificial phase jumps, which is easily implemented into the algorithm used for data processing.

Second, for most values of delay time several data sets were used to calculate phase shifts. Most of the data points obtained from different measurements precisely coincide in Fig. 24: only for a few values of fluence and delay time does the spread of data points become visible in the form of several vertically displaced symbols. Thus, the automatic data processing allows the elimination of unwanted effects due to shot-to-shot energy fluctuations and pointing stability of the laser beam.

The final results of automatic data processing, to be used for physical interpretation, is presented in Fig. 25 in the form of a family of temporal phase dependencies for fluence values in the range $F = 0.25 \div 1.35 F_{thr}$ obtained with s small fluence step $\delta F = 0.01 F_{thr}$. For fluences exceeding the ablation threshold the ablating material continuously moves away towards the vacuum and the velocity of the movement is larger for higher fluences. An apparent "gap" for delay times above 2 ns indicates that a small change in excitation fluence of only 1% causes a large difference in surface position. This effect arises from previously discussed extremely high spatial

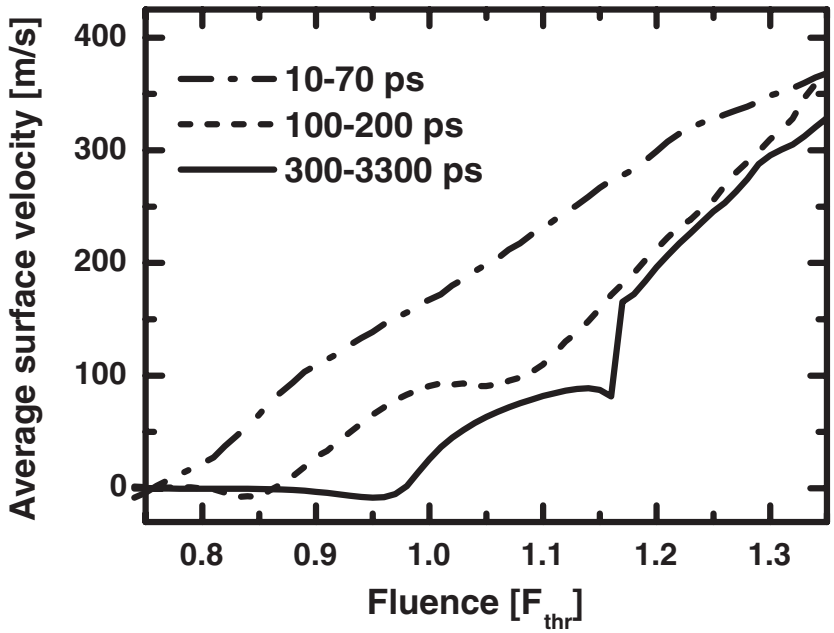

Figure 26: Fluence dependence of the average velocity of excited GaAs-surface calculated for three different time intervals $10 \div 70$ ps, $100 \div 200$ ps and $300 \div 3300$ ps.

gradients of the phase, which now can be attributed to the discontinuity in the surface position. This discontinuity of the surface position inevitably implies the jump in surface velocity.

Very important physical information can be extracted from the analysis of *surface velocity* as a function of excitation fluence and delay time. Being equal to the slope of curves in Fig. 25 surface velocity is found to be dependent on both excitation fluence and delay time. Different parts of phase dependencies of Fig. 25, corresponding to three different time intervals $10 \div 70$ ps, $100 \div 200$ ps and $300 \div 3300$ ps were fitted by a linear low $\phi(t) = At + B$. The derived slope A, to be referred to as an *average surface velocity*, for three different time intervals is plotted in Fig. 26. It is apparent that in the early stage of expansion in the time range $10 \div 70$ ps the surface velocity scales linearly with the applied laser fluence. Note that a non-zero surface velocity is evident for excitation fluences below ablation threshold, indicating on sub-threshold surface deformations, to be discussed later. Average surface velocity during the time interval $100 \div 200$ ps appears to be significantly smaller. Thus, the surface movement slows down, whereas the most significant decrease of surface velocity occurs for excitation a few percent above the threshold, indicating the formation of local minima. For long-term expansion between $300 \div 3300$ ps this local minima develops into the jump of surface velocity from 80 m/s at $F = 1.16F_{thr}$ to 160 m/s at $F = 1.17F_{thr}$. Surface velocity for higher fluence values did not change significantly

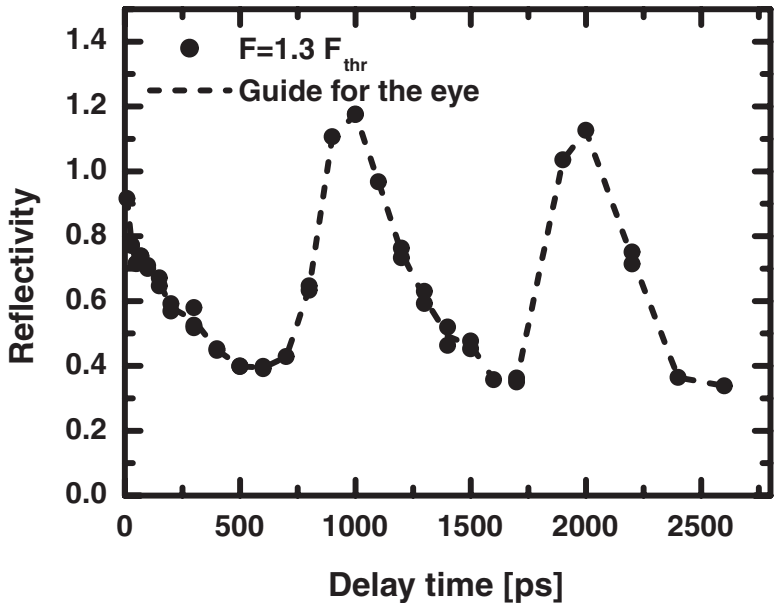

Figure 27: Temporal evolution of surface reflectivity of ablating GaAs-surface, integrated over the area of constant fluence $F = 1.3\ F_{thr}$.

as compared with the preceding curve.

Slowing down of surface movement for excitation slightly above the ablation threshold, which leads to the formation of velocity jump and discontinuity of the ablating surface, represents the most important result of above-threshold interferometric measurements. Before starting to interpret these results it makes sense to discuss and analyze complimentary time-resolved surface reflectivity measurements and present the interferometric measurements of sub-threshold surface deformations.

3.2.2 Temporal evolution of surface reflectivity of ablating GaAs-surface

Interferometic measurements allow direct monitoring of the movement of an ablating surface and thus provide reliable information about the position of the ablation front at each pump-probe delay time. The question arises as to whether some additional information about the internal structure of the ablating material can be obtained from time-resolved reflectivity measurements (see Fig. 20).

Figure 27 shows the temporal evolution of surface reflectivity of an ablating GaAs-surface excited 30 % above the ablation threshold, which is normalized on the reflectivity value of an undisturbed GaAs-surface. A fully automatic algorithm developed to process many surface reflectivity images for different delay times implies an automatic determination of the position and peak fluence of the pump pulses from final microscopy images of ablation craters, which is very similar to the discussed

processing of interferometric data. A small spread of data points in Fig. 27 obtained from several independent measurements demonstrates the high accuracy of surface reflectivity measurements.

Analogous to the Newton rings in the spatial domain, the distinct maxima and minima of time-dependent reflectivity in Fig. 27 are due to constructive and destructive interference of probe radiation reflected from the two optically sharp interfaces sketched in Fig. 18. We have simulated temporal evolution of both the phase shift and the reflectivity for two previously discussed models: spatially homogeneous and "bubble-like" internal structures of the ablating layer (see Fig. 18).

The system of three layers shown in Fig. 28(a) can be used to simulate both models. Being the common elements for both models, the two optically sharp interfaces are the ablation front $z(t) = vt$ propagating towards the vacuum with constant velocity $v = 275$ m/s (deduced from interferometric measurements at excitation fluence $F = 1.3F_{thr}$) and the bottom of the final ablation crater with a depth $h = 50$ nm. Temporal evolution calculated at a single point in space (center of laser-excited area in Fig. 28(a)) for both phase shift and reflectivity (normalized to the values of undisturbed solid surface) is presented in Fig. 28(b) for two structures of the ablating layer.

The homogeneous model utilizes the Maxwell-Garnett formula (see Eq. (20)): $n_1(t) = n_2(t) = \sqrt{\varepsilon_{MG}(f(t))}$ with the time-dependent filling factor $f(t) = h/z(t)$ and the following dielectric constants for gaseous phase and liquid droplets: $\varepsilon_g = 1$, $\varepsilon_l = (2.0 + 3.4i)^2$. Both the phase shift and reflectivity dependencies are found to be strongly different from experimental results, independent of the choice of the dielectric constant ε_l ($\varepsilon_g = 1$ must be always close to unity for dilute gases). The failure of the Maxwell-Garnett description is predetermined by the fact that the well-known filling factor becomes very small for long delay times, $f < 0.1$, which results in a small index of refraction. A strange temporal behavior of the phase, which does not follow the continuously increasing geometric deformation of the ablation front, can also be explained by the smallness of the refractive index, since most of the incident radiation is reflected not from the ablation front itself but propagates through the layer and is reflected from the non-ablating melt. Roughly speaking the phase of light reflected from the back interface between the ablating layer and the non-ablating material is seen.

The inhomogeneous "bubble-like" structure provides a good agreement with experimental data for the following set of parameters: $\tilde{n}_1 = 4.4 + 0.7i$, $d_1 = 40$ nm, $\tilde{n}_2 = 1$, $\tilde{n}_3 = 2.0 + 3.4i$. However, among these fitting parameters only $\tilde{n}_1$ and d_1 are

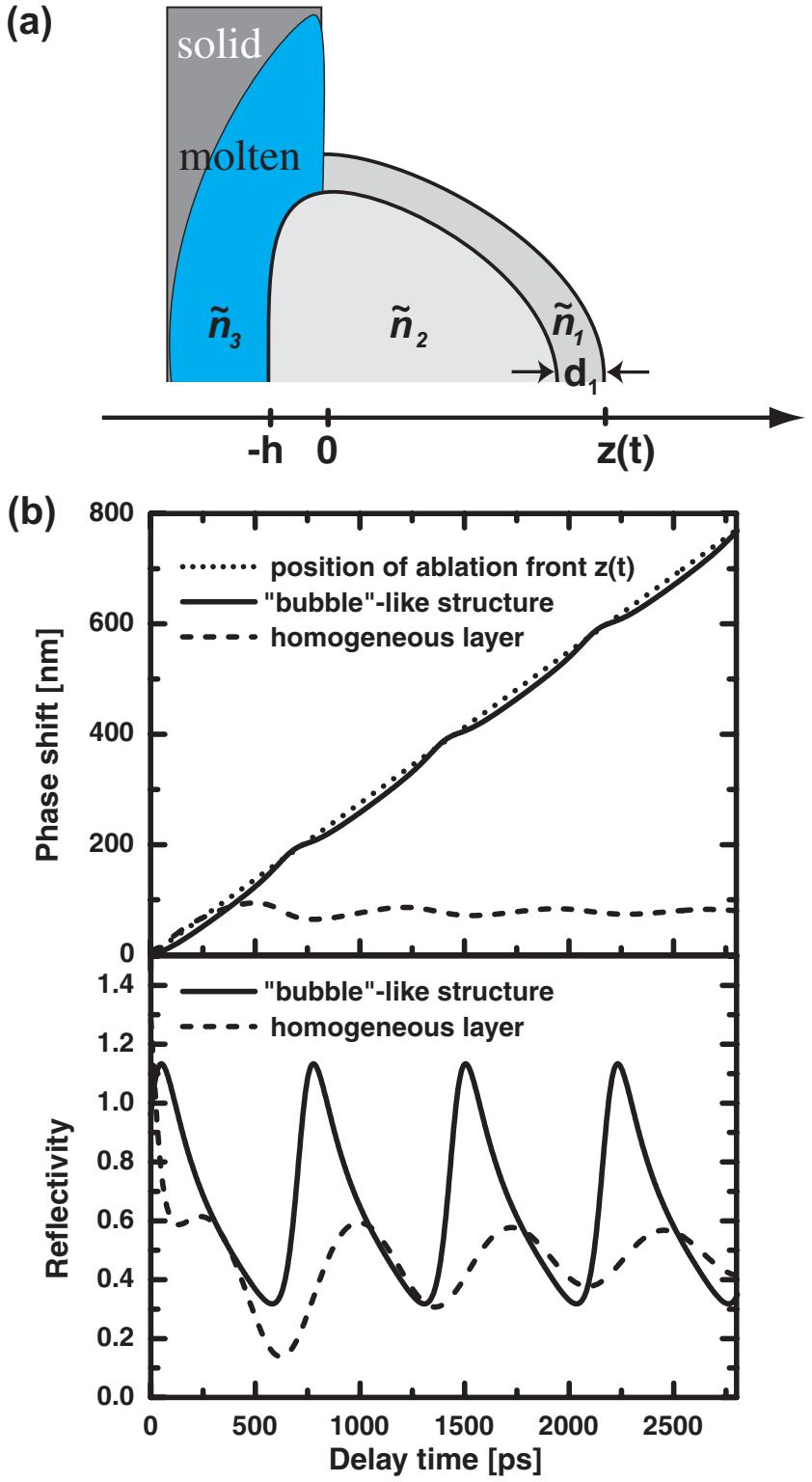

Figure 28: (a) Schematic for thin-film calculations of the optical properties of ablating plume for both homogeneous and "bubble"-like internal structures: $\tilde{n}_i$- complex index of refraction; $h = 50$ nm - depth of ablation crater, $z(t) = vt$ - position of ablation front; (b) phase shift and reflectivity for homogeneous layer ($\tilde{n}_1(t) = \tilde{n}_2(t)$-according to Maxwell-Garnett with $f(t) = h/z(t)$, $\tilde{n}_3 = 2.0 + 3.4i$) and "bubble"-like structure ($\tilde{n}_1 = 4.4 + 0.7i$, $d_1 = 40$ nm, $\tilde{n}_2 = 1$, $\tilde{n}_3 = 2.0 + 3.4i$).

completely unknown. The question arises how as to reliable and unique the results of the fit are, if they predict that the liquid "bubble" possesses dielectric properties: $\mathrm{Re}\{\tilde{n}_1\} >> \mathrm{Im}\{\tilde{n}_1\}$!

In order to test the reliability of fitting results we shall again have a look at the experimentally measured temporal evolution of the reflectivity in Fig. 27: the maxima appear to be relatively narrow and slightly asymmetric. When playing with parameters of thin-film simulations we were able to generate similar shapes only if the following condition was fulfilled:

$$2d_1\mathrm{Re}\{\tilde{n}_1\} \simeq \lambda\,, \tag{21}$$

where λ stands for probe wavelength. In case $2d_1\mathrm{Re}\{\tilde{n}_1\} = \lambda$ reflectivity maxima are symmetrical, whereas small deviations introduce some asymmetry. For the parameter sets which do not satisfy this condition the reflectivity maxima are broad but the minima are narrow. Although there are many possibilities to satisfy the condition (21), the requirement of having certain reflectivity values at interference minima and maxima forbids an arbitrary choice of parameters. Temporal evolution of the phase in Fig. 28(b) is in perfect agreement with the experimental data in Fig. 25: the phase follows the geometric surface deformation whereas some small periodic deviations in the form of "waves" correlate with reflectivity minima and maxima and can be assigned to phase contribution due to internal interference effects in the ablating layer. We have also simulated spatial phase profiles with the given parameters of the "bubble" (not shown), which appear to be similar to those in Fig. 22.

The only problem with the fit is that the period between reflectivity minima and maxima in the simulated dependencies of Fig. 27(b) is a little bit smaller than in the experimentally measured curve of Fig. 27. One could correct this discrepancy by setting the refractive index for the two-phase mixture $\tilde{n}_2 = 0.9$ in thin-film calculations. A lot of other interferometric data sets and their analysis (not discussed here) did also provide confusing indications that the average refractive index of the ablating layer is somewhat smaller than unity. The simplest physical explanation of this manipulation would be a negative Drude-like contribution to the refractive index from free electrons. However, this hypothesis contradicts with the results of Cavalleri and co-workers [40] who have investigated femtosecond laser ablation in GaAs and Si by means of time-of-flight mass spectroscopy. Their results show that a fraction of anablating plume detected ~ 10 cm away from the sample in UHV (ultra-high vacuum) contains mostly neutral atoms and small atomic clusters, whereas the detected fraction of single-ionized atoms is negligibly small ($\sim 10^{-4}$). Currently we

have no plausible explanation for $\tilde{n}_2 < 1$, which requires a critical consideration of the above multi-parametric fit.

Hovewer, keeping in mind certain problems with our fit, we still shall discuss the optical properties of the "bubble". An observation that the "bubble" possesses dielectric optical properties might be interpreted as metal-isolator transition, which can take place, for example, in liquid metals at high temperatures and low densities [50, 51]. The results of extensive theoretical and some experimental research of femtosecond laser ablation show that the liquid material of the "bubble" possesses a significantly lower density $\rho_{bubble} \sim 0.5 \div 0.7 \rho_{liquid}$ [43, 45] and high temperature strongly exceeding the melting temperature [40]. Moreover, according to Mott "most metal-isolator transitions in liquids occur in the regime where $l \sim a$" [51], where l and a denote the mean free path of conducting electrons and mean interatomic distance, respectively. The condition $a \sim l$ is known as the Joffe-Regel limit and will be introduced and discussed in detail in the next chapter in a different context. At this point it is only necessary to cite the results of *ab initio* molecular dynamics simulations of atomic structure and bonding in liquid GaAs [52], which obtained $l \sim a$.

The idea about the possibility of metal-isolator transition during femtosecond laser ablation is not new; it was first pointed out by Sokolowski-Tinten at al. [53] as one of the ways to explain transient interference phenomena (Newton rings). At that time this hypothesis seemed to be unlikely, since absolutely no information about the internal structure and thermodynamic properties of ablating layer was available. Somewhat later the same idea was exploited to justify the high optical transparency of the 70 nm-thick "bubble" obtained from hydrodynamic simulations of femtosecond ablation in aluminum [43]. In this context the observed dielectric optical properties of the "bubble" become less surprising.

More experiments should be performed in order to verify this important but preliminary observation. According to the results of our thin-film calculations performed for different probe wavelengths, broad-band optical measurements should be very sensitive in the case of the "bubble" with the parameters discussed above.

Unfortunately we do not see any possibility to extract information about the mass density of the liquid "bubble" from the optical measurements, which seems to be very important for the understanding of the underlying physics.

3.2.3 Extremely long reversible surface deformations of GaAs-surface excited a few percent below ablation threshold

The character of the sub-threshold surface deformations of a GaAs-surface excited a few percent below ablation threshold, the indication of which could readily be recog-

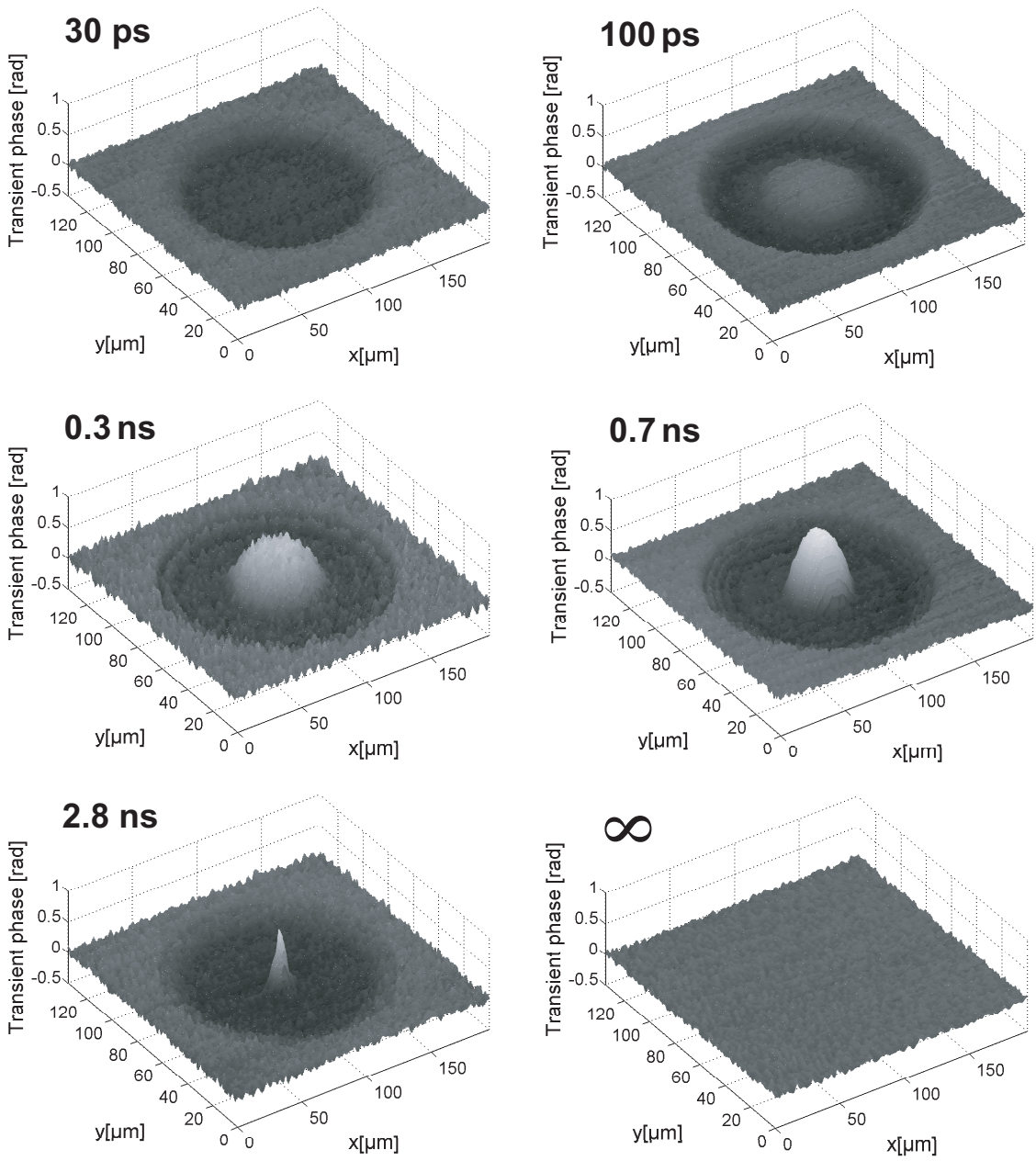

Figure 29: Interferometrically measured phase maps at GaAs-surface excited below ablation threshold for different pump-probe delay times, $F = 0.98\ F_{thr}$. Dark oval areas represent the negative phase shift due to the changes of the optical constants upon melting, whereas the bright hill can be associated with fully reversible transient surface excursion.

nized in Fig. 26 as a non-zero expansion velocity during the first tens of picoseconds after excitation, is very important for the understanding of the physical nature of the extremely sharp ablation threshold.

A large series of interferometric measurements was performed for excitation fluences near the ablation threshold. Due to shot-to-shot energy fluctuations some of the pulses initiated the ablation and some of them had a peak fluence slightly below the ablation threshold. The energies for each shot were recorded by a photodiode, which allows to choose data sets with a desired peak fluence. A series of phase maps corresponding to laser excitation approximately 2% below ablation threshold is presented in Fig. 29. The dark oval area which corresponds to a negative phase shift of about 0.08π existing in all the transient phase maps of Fig. 29 mainly represents the changes of the optical constants upon melting, whereas the contribution of surface deformations is negligibly small. The bright hill in the center of the laser-excited area corresponding to a positive phase shift, which comes out, reaches the maximum and disappears within a few nanoseconds, can be associated with fully reversible transient surface excursion. The hill becomes very narrow for long delay times indicating that the laser-excited surface contracts much faster for smaller excitation fluences. The resoldification occurs on a time scale of the order of 10 ns [36] and no permanent changes of surface morphology can be seen in the final phase surface ($\Delta t = \infty$).

The dynamics of sub-threshold surface deformations in the center of the laser-excited area is shown in Fig. 30, where the curves for different excitation fluences near the ablation threshold have been produced manually by sorting a large amount of interferometric data sets with respect to peak excitation fluence. The uncertainty in the fluence determination was around $\pm 1\%$. Fig. 30 demonstrates that reversible surface deformations with maximum amplitudes of the order of 100 nm occur just below ablation threshold. A surface excited with $F = 0.99F_{thr}$ shows a huge excursion of 150 nm up to 6 ns. For smaller excitation fluences the maximum amplitude of transient surface excursion is smaller and the time-scale for this up-and-down motion is shorter. As expected, excitation just above the threshold, $F = 1.01F_{thr}$, leads to irreversible expansion of ablating material and leads to the formation of 40 nm deep ablation craters.

At this point it should be mentioned that the observed surface deformations with amplitudes of several tens of nanometers induce relatively small positive phase shifts $\Delta\Phi < \pi$ ($1\pi = 100$ nm). Thus the contribution of the phase shifts due to the changes in the optical constants cannot be completely disregarded as is the case for large

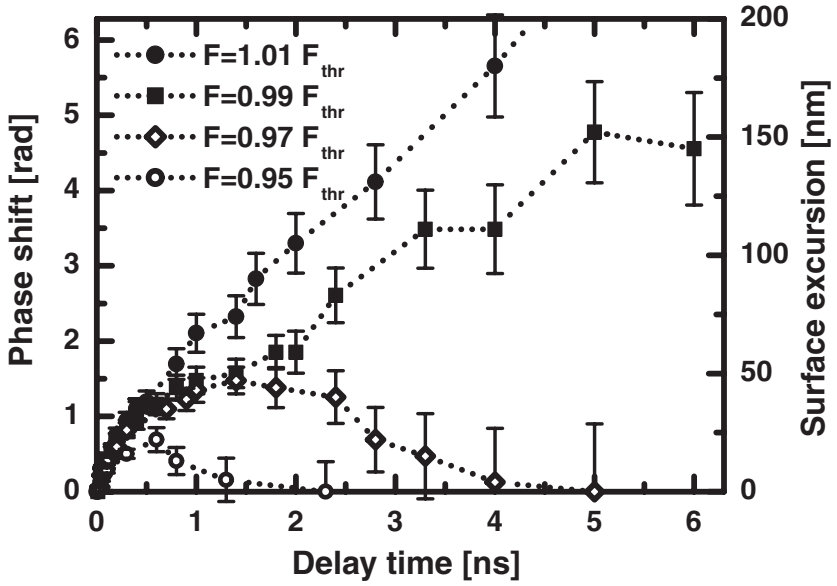

Figure 30: Dynamics of transient surface deformations of GaAs-surface excited by pulses with peak fluences very close to ablation threshold F_{thr}. The curves represent the result of manual selection of data points from a large amount of interferometric data sets, whereas the big error bars are due to inevitable shot-to-shot energy fluctuations.

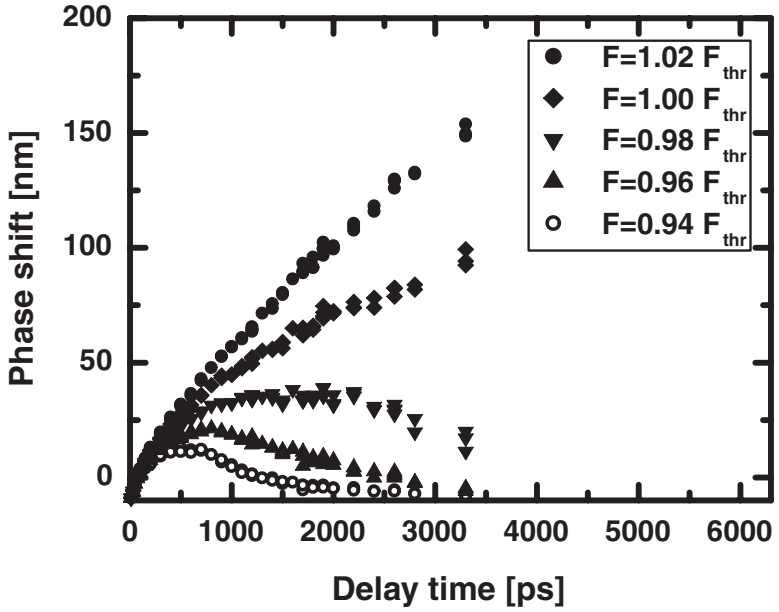

Figure 31: Dynamics of transient surface deformations of GaAs-surface for fluences very close to ablation threshold F_{thr}. The curves are automatically reconstructed from data sets with peak fluence $F = 1.3\ F_{thr}$ by integrating over the area of constant fluence.

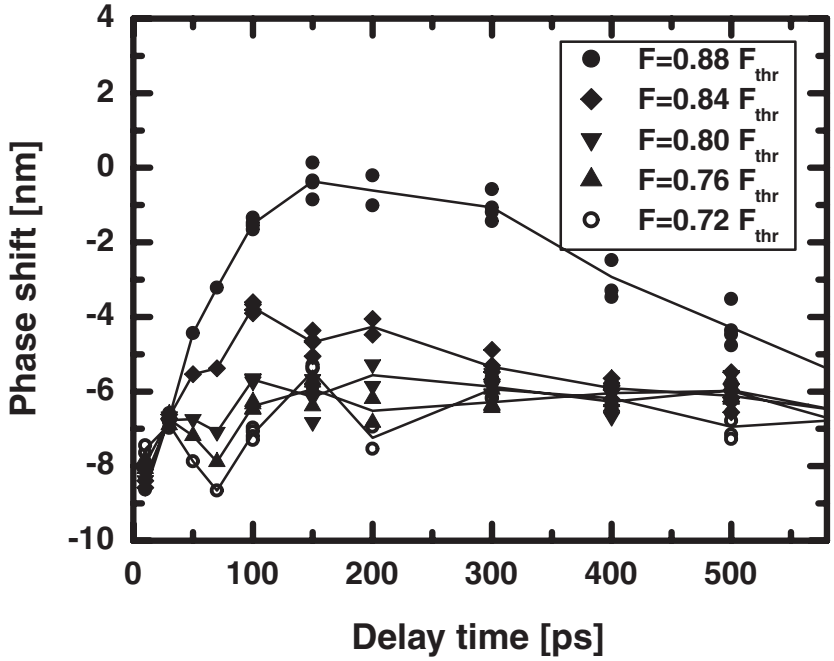

Figure 32: Dynamics of transient surface deformations of GaAs-surface for fluences $10 \div 30\%$ below ablation threshold. The onset of thermo-acoustic oscillations manifests itself as a local phase maximum at 30 ps and local phase minimum for 70 ps for three curves corresponding to fluence values $F = 0.72, 0.76, 0.80\ F_{thr}$. The curves are automatically reconstructed from data sets with peak fluence $F = 1.3\ F_{thr}$ by integrating over the area of constant fluence.

surface deformations induced by the moving ablation front. However, the analysis performed in the previous chapter (see Fig. 7) shows that the contribution from the geometric surface deformation is still dominant.

The content of Fig. 31 is identical to that of Fig. 30, the only difference is that the curves have been obtained via automatic data processing from the data set with peak excitation fluence 30% above the ablation threshold, which was used to generate all curves in the previous section. The quantitative agreement of the curves in Figures 30 and 31 does again demonstrate the good performance of the fully automatic processing algorithm. On the other hand, it becomes evident that transverse spatial effects do not affect the dynamics of sub-threshold surface deformations.

Before providing a further interpretation of sub-threshold deformations observed a few percent below ablation threshold we would like to present experimental data for the dynamics of a GaAs-surface induced by even smaller excitation fluence.

3.2.4 Thermoacoustic oscillations of superficial laser-molten layer of GaAs-surface excited 20% below ablation threshold

Figure 32 demonstrates temporal phase dependencies for several values of excitation fluence significantly below ablation threshold. The magnitude of the observed phase shifts is so small that their physical nature cannot be uniquely identified. However, the onset of oscillations, which manifest themselves as phase maximum at 30 ps and phase minimum at 70 ps represents the striking feature of temporal phase dependencies for the 3 lowest fluence values $F = 0.72, 0.76, 0.80\ F_{thr}$. Larger intervals between the successive data points do not allow us to conclude whether the oscillating character persists for longer delay times. In order to convince ourselves that the oscillations are not the artifacts of the measurement, we have processed another series of interferometric data sets and were able to see the same behavior. The amplitude of these oscillations cannot be exactly determined since the observed tiny phase shifts $\sim \pi/100$ are influenced by the phase contributions of the optical constants. The corresponding temporal evolution of surface reflectivity (not shown) does also exhibit oscillations with the amplitude ~ 0.01, which emphasizes the changes of the optical constants accompanying surface deformations. However, the amplitude of surface oscillations is not likely to exceed a few nanometers.

Essentially, we hoped to see such tiny oscillations of the surface from the very beginning of the experiments since they are likely to represent thermo-acoustic oscillations of the laser-molten superficial layer. Upon melting the hot pressurized liquid layer is created on top of a non-molten solid. Liquid film stands under big pressure and starts to expand in both directions, whereas initial spatially inhomogeneous pressure (or strain) distribution tends to relax via acoustic perturbations propagating through the film. Since a solid-liquid interface possesses a high acoustic impedance, the acoustic perturbations experience partial reflections, which gives rise to damped oscillations in the time domain. At liquid-vacuum interface acoustic pulses are reflected completely whereas the strain changes the sign upon reflection. A more detailed description of perturbations is provided in [39]. The characteristic timescale of thermo-acoustic oscillations is naturally determined by the ratio of liquid film thickness l to the speed of sound in liquid c_s:

$$\tau_{ac} = \frac{2l}{c_s}\,. \tag{22}$$

According to our knowledge the sound velocity in liquid GaAs has neither been measured nor calculated. However, in many materials (Si,Ge,Sn,$Cd_xZn_{1-x}Te$) the sound velocity of a liquid phase is roughly half as large as that of the longitudinal

acoustic waves in a solid [54, 55]. For this reason we estimate the speed of sound in liquid GaAs to be around 2500 m/s (5000 m/s in solid). Assuming that the observed minima and maxima of phase dependencies are induced by thermo-acoustic oscillations, we get an estimate for the thickness of liquid film $l = 0.5 \times 30\ ps \times c_s \simeq$ 40 nm. This is a very reasonable estimate, which falls within the range of previous estimations based on the depth of ablation craters [1, 2], but also consistent with the results of recent X-ray-diffraction experiments on ultrafast melting in germanium [39].

The most straight-forward estimation for the thickness of a laser-heated layer based on the penetration depth of the laser wavelength is hardly possible for several reasons. First of all the linear absorption is very weak (skin depth $\sim$ 700 nm for GaAs at $\lambda = 800$ nm) so that nonlinear absorption mechanisms must be considered. At the applied intensities of about 1 TW/cm^2 the penetration depth due to two-photon absorption ($\sigma_2 = 2.2 \times 10^6$ cm/TW at $\lambda = 1060$ nm [56]) would be of the order of a nanometer, which is nonsense. Most likely the mechanism of light absorption is more complicated. After being generated hot carriers might, for example, transfer energy inside the material by diffusion until the lattice is heated and melting takes place [57]. Thus, it is extremely difficult to exactly calculate the spatial distribution of deposited energy inside the material, which could provide a reliable estimation for the thickness of the laser-molten layer.

However, a simple and robust estimate for the thickness of the molten layer can be obtained from the energy conservation law for the absorbed laser energy. A significant fraction F_{abs} of the incident laser fluence F_{inc} is absorbed by the solid: $F_{abs} = F_{inc}(1-R)$, where R can be well approximated by a reflection coefficient from an unexcited solid [57]. Using the Fresnel formula for p-polarized pulses (800 nm @ 45°) and $\tilde{n}_{solidGaAs} = 3.7 + 0.09i$ [27] we obtain R=0.2. Thus, for excitation 20% below ablation threshold the absorbed laser fluence is $F_{abs} = 0.8 \times 0.8 F_{thr} \simeq$ 0.13 J/cm^2. Assuming the spatial distribution of deposited energy density inside the material to be exponential $E(z) = (F_{abs}/z_0)\ \exp(-z/z_0)$ with an unknown scale z_0, one could ask the question "What is a thickness l of the molten layer?" In order to melt 1 cm^3 of the material a definite amount of energy must be supplied, which is equal to $E_M = \{c_p(T_M - T_0) + L_M)\}\rho_0$ with $c_p = 0.3$ J/gK - heat capacity, T_0=300 K - initial (room) temperature, $T_M = 1511$ K - melting temperature, $L_M = 670$ J/g - latent heat of fusion, $\rho_0 = 5.3$ g/cm^3 - density of solid GaAs at room temperature [58, 59]. Thus the thickness l of the molten layer is given by:

$$\frac{F_{abs}}{z_0}\ \mathrm{e}^{-l/z_0} = \{c_p(T_M - T_0) + L_M)\}\rho_0\,. \tag{23}$$

Some trivial mathematical analysis of Eq. (23) shows that the maximum possible thickness

$$l_{max} = \frac{F_{abs}}{\mathrm{e}\{c_p(T_M - T_0) + L_M)\}\rho_0} \simeq 90 \text{ nm} \tag{24}$$

is reached for $z_0 = l_{max}$ (z_0 was used as a free parameter). Although this estimate was obtained assuming an exponential profile for the deposited energy density, it will be not strongly different for other smooth profiles with the maximum at $z = 0$ and zero at $z = \infty$. The obtained requirement $l < l_{max} \simeq 90$ nm is fully consistent with the above interpretation.

The temperature of liquid film for $z < l$ must be higher than the equilibrium melting temperature: the rest of the deposited laser energy is spent in overheating the liquid above the equilibrium melting temperature T_M ($c_p^M = 0.434$ J/gK - heat capacity of liquid GaAs). Assuming the exponential profile with $z_0 = 90$ nm and $F_{abs} = 0.13$ J/cm^2 a huge overheating at the surface by 4000 K is obtained. Apart from this very rough estimate, the experimentally determined, slightly underestimated surface temperature for a given fluence is around 2500 K [40] suggesting a strong overheating of 1000 K. The role of strong overheating for the dynamics of surface deformations will be discussed in the next section.

Summarizing this discussion the interpretation of the observed onset of temporal phase oscillations on a sub-100 ps-time scale as thermo-acoustic oscillations of laser-molten film seems to be very plausible and provides an estimate for the thickness of the laser-molten superficial layer.

For the two highest fluence values $F = 0.84, 0.88\ F_{thr}$ in Fig. 32 no temporal oscillations can be recognized any more. Surface dynamics seems to be reduced to a simple up-and-down surface motion similar to that for deformations observed a few percent below ablation threshold (see figures 30 and 31) but with lower amplitudes and on a faster time-scale. In some other interferometric data sets we have seen indications of thermo-acoustic oscillations for fluence values around $\sim 0.85\ F_{thr}$ but on a slightly larger time scale. More measurements with shorter time intervals need to be done in order to verify this preliminary observation.

For fluence values below $0.7\ F_{thr}$ no indications of thermo-acoustic oscillations have been observed. Fluence value $F \simeq 0.5\ F_{thr}$ corresponds to the melting threshold: slightly above the melting threshold the thickness of the laser-molten layer is comparable with the skin-depth for the probe wavelength, which makes the interpretation of interferometric measurements complicated. For this reason we do not discuss the corresponding experimental data.

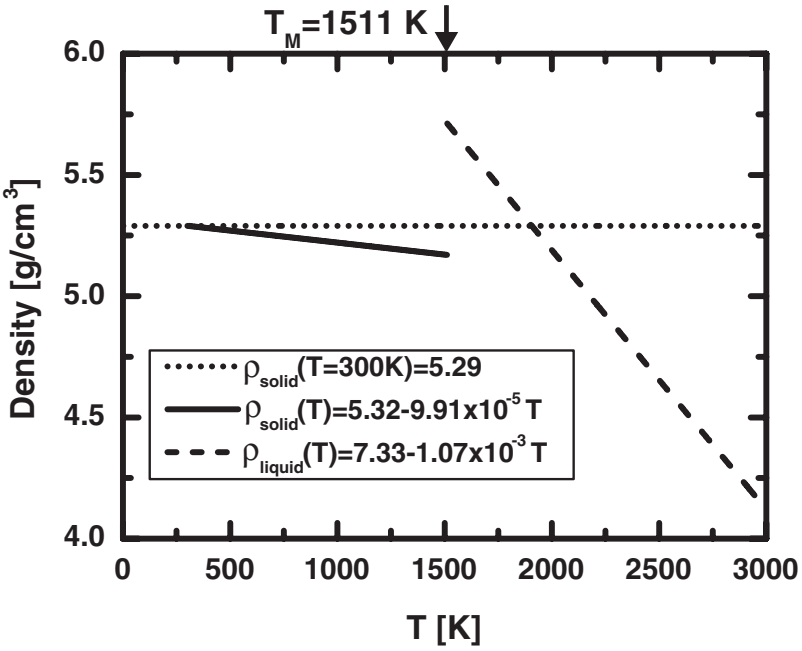

Figure 33: Temperature dependence of mass density in solid and liquid GaAs. Density experiences a positive jump upon solid-liquid phase transition, whereas a negative slope for both phases indicates a thermal expansion.

3.3 Scenario of surface dynamics and sharp ablation threshold in GaAs

At this point, having presented and discussed some details for several types of laser-induced surface deformations in GaAs corresponding to a rather broad range of applied laser fluences, it is time to discuss the two most important observations. These are (i) the fully reversible large-amplitude deformations of a GaAs-surface excited a few percent below threshold on a time-scale $\tau >> \tau_{acoustic}$ (see Fig. 31) and (ii) deceleration and formation of a jump in velocity of a moving ablation front (see Fig. 26). These two findings represent the main experimental results of this investigation; they have been obtained without any assumptions concerning the underlying physics and cannot be explained by the ambiguities of the technique. Other observations and their interpretation as, for example, the justification of the existence and optical properties of the "bubble-like" structure just seem to be plausible.

In order to interpret these observations we must inevitably make some assumptions and, for this reason, this interpretation will be referred to as the possible scenario of femtosecond laser ablation, which is capable of explaining the available experimental data.

All previous discussions are based on the assumption that a hot pressurized laser-

molten layer of material is created a few picoseconds after laser excitation. Since energy thermalization is so fast it occurs at constant volume (at solid density at room temperature). Figure 33 shows the temperature dependence of density for the solid and liquid phases of GaAs [58], whereas the dotted horizontal line in Fig. 33 marks the density of GaAs at room temperature. For both phases the density decreases with growing temperature due to thermal expansion. The striking feature is a positive jump of density by 10% as a result of melting. Whereas for temperatures around the melting temperature, $T \sim T_M$, the equilibrium liquid density is larger than ρ_0, it becomes smaller in case of strong overheating $T > 1.25\ T_M$. Thus the molten layer at solid density is pressurized and tends to expand only in the case of sufficient overheating.

For further discussion we would like to stress that the interval of surface temperatures $T_M < T < 3000$ K approximately corresponds to fluence range $0.5F_{thr} < F < F_{thr}$ [40]. The disregarded fluence interval $0.5F_{thr} < F < 0.7F_{thr}$ corresponds to the region where we would expect the formation of a thin contracting liquid layer on top of a hot expanding solid. No reliable experimental data is available for this fluence range. For higher fluence values a rather thick overheated liquid layer at solid density must be slightly pressurized (see Fig. 33), which makes the physical origin of the tiny thermo-acoustic oscillations observed for $0.7F_{thr} < F < 0.8F_{thr}$ quite clear.

In order to get a feeling about the amplitudes and velocities of surface motion upon thermo-acoustic expansion we shall first discuss a very simple model of a pressurized homogeneously heated liquid film of thickness l on a hard substrate, which is allowed to expand in one dimension. Liquid density is assumed to have the temperature dependence shown in Fig. 33 and initial density ρ_0. The initial strain

$$\frac{\Delta l}{l} = -\frac{\Delta \rho}{\rho}\,, \tag{25}$$

which is proportional to the density difference $\Delta\rho = (\rho_{liquid}(T) - \rho_0)$, would drive the surface to expand with constant velocity

$$v = c_s \frac{\Delta l}{l}\,, \tag{26}$$

during the time $0 < t < \tau_{ac}$, whereas the maximum surface excursion is $d_{max} = d(\tau_c) = 2\Delta l$. For the time interval $\tau_{ac} < t < 2\tau_{ac}$ the surface will move back with the same speed until the original position is reached $d(2\tau_{ac}) = 0$ and so on. Upon expansion the internal tensile stresses in a liquid are developed (corresponding to negative pressure!), which slow down the surface motion and lead to the subsequent

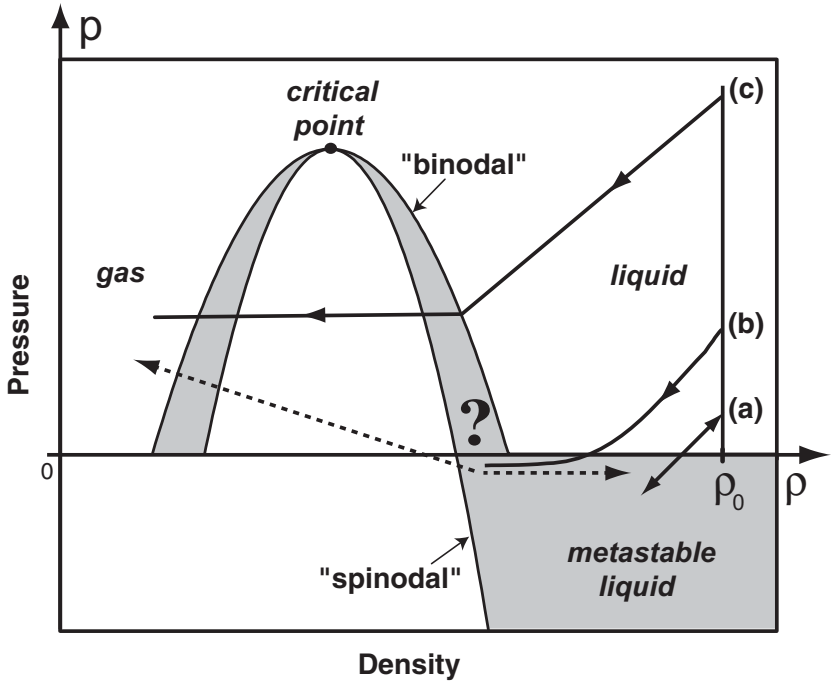

Figure 34: Transient states of expanding material on pressure-density phase diagram. Three expansion isoentropes (a), (b) and (c) correspond to three different excitation fluences: (a)-fast thermo-acoustic oscillations 20% below threshold, (b)-long reversible surface movement in the vicinity of the threshold, (c)-irreversible dynamics above threshold.

contruction of the expanded liquid film. In reality the oscillations of liquid film thickness between l and $l + 2\Delta l$ will be damped out, leaving a residual surface excursion $d = \Delta l$ due to the thermal expansion of the liquid. Final state of liquid film is, of course, that at zero (atmospheric) pressure.

Thermodynamic states with *negative pressures*, which are well defined for liquids, are *metastable* [60]. Some very basic discussion about the role of such states can be found in [61], where the phase diagram of the van der Waals fluid is analyzed. Our analysis of thermo-acoustic oscillations shows that metastable states of liquid under negative pressure play an important role. The concept of a uniform negative pressure is actually applicable only for liquids since, in contrast to the solids, shear forces are practically absent. For dilute gases the pressure must be always positive.

Thermo-acoustic oscillations with a small amplitude of a few nanometers, the indications of which we have observed for excitations $20 \div 30\%$ below ablation threshold, do not lead to a significant reduction of density and, therefore, the sound velocity is constant. On phase diagram in Fig. 34 these small thermo-acoustic oscillations correspond to the oscillations of pressure and density on the isoentrope (a). The

observed velocities of surface movement are much smaller than the speed of sound as expected from Eq. (26).

The situation must be quite different when the amplitudes of surface motion become bigger, which lead to a bigger change of material density. The importance of a liquid-gas phase transition for the formation of the "bubble" has already been mentioned. Keeping in mind the huge amplitudes of a reversible surface excursion of about $d \sim$50 nm, which are observed a few percent below ablation threshold (see Fig. 31 we estimate the reduction of mean density within the expanding film by the factor $(l + d)/l \sim 2$. Here we have used the value $l = 50$ nm, since the thickness of the laser-molten layer excited near the threshold is unlikely to be significantly different from the value of 40 nm estimated for thermo-acoustic oscillations observed 20% below the threshold.

The big estimated reduction of material density suggests that the liquid deeply enters the metastable region of negative pressures on phase diagram (much closer to the spinodal as compared to thermo-acoustic oscillations): it is likely to be a liquid with a lot of small gas bubbles with the radius being below the critical nuclei radius. The onset of phase transition leads to a drastic reduction of sound velocity discussed above (typically by factor $100 \div 1000$), which is capable of explaining an extremely big time-scale for reversible surface deformations. Indeed, given a small sound velocity the time-scale of thermo-acoustic oscillations (see Eq. (22)) becomes correspondingly large. This situation corresponds to the expansion isoentrope (b) in Fig. 34.

Small bubbles with a subcritical radius, generated as a result of thermal density fluctuations, tend to contract again due to the *surface tension* providing a microscopic mechanism of *small residual tensile stresses* or *small negative pressures* at the last stage of expansion. The existence of the tensile stresses manifests itself in the slowing down of initially fast surface expansion presented in Fig. 26. Whereas below the threshold these residual tensile stresses are capable of stopping the expansion completely, above the threshold they can only reduce the expansion velocity. The balance between the tensile stresses acting during the last stage and the kinetic energy acquired during the initial stage of hydrodynamic expansion will essentially determine whether the layer will detach from the surface (ablate) or not. These two alternatives are represented by two dashed arrows at the end of the isoentrope (b) in Fig. 34. According to our scenario, both the hydrodynamic expansion and the kinetics of liquid-gas phase transition should be incorporated into realistic theoretical calculations in order to simulate the behaviour near ablation threshold.

At this moment it is not yet clear whether the jump in expansion velocity observed 15% above the threshold (see Fig. 26) has something to do with the generation and the properties of the gas bubbles (kinetics of phase transition). The observed deceleration of the surface motion upon expansion suggests that the states of liquid under negative pressure also play an important role for ablation dynamics slightly above the threshold. More theoretical understanding of poorly investigated thermodynamic properties of metastable liquids and liquid-gas mixtures under negative pressures is required in order to verify the suggested scenario and explain the experimental data.

In the above discussion we have not mentioned such possible ablation mechanisms as "explosive boiling" [62], "spinodal decomposition" [46] and "spallation" [63, 64]. At the current level of understanding the interpretation of available (published) experimental results using these mechanisms would be rather speculative.

Summarizing this discussion we have presented a scenario which is capable of *qualitatively* explaining reversible large-amplitude surface deformations just below the threshold and deceleration of the ablating surface just above the threshold by a frustrated liquid-gas phase transition accompanied by the formation of subcritical bubbles. The proposed mechanism does also reveal the physical nature of the sharp ablation threshold in GaAs.

3.4 Interferometric measurements at fs-laser excited Si-surface

3.4.1 Failure of interferometric observation of moving ablation front in Si

In an attempt to obtain analogous information about the dynamics of femtosecond laser ablation, we have performed similar interferometric measurements in silicon. Unfortunately, all the results of the above-threshold interferometric measurements can be summarized in only one figure. Figure 35 shows an example of the interferometric and reflectivity measurement at a Si(111) surface excited with $F = 1.33\ F_{thr}$ ($F_{thr} = 0.35$ J/cm^2) made at a delay time of 0.9 ns. Newton rings (Fig. 35(a)) represent spatial reflectivity modulation with diminishing contrast from the periphery to the center (dotted curve in Fig. 35(e)). A transient interferogram (Fig. 35(b)) allows us to retrieve a remarkable phase surface (Fig. 35(c)), which is visualized by an almost flat-top spatial profile of the phase (solid curve in Fig. 35(e)). The remaining ablation crater (Fig. 35(d)) is extremely shallow and has a depth of 7 nm at the crater boundary, in agreement with the results of microscopic characteriza-

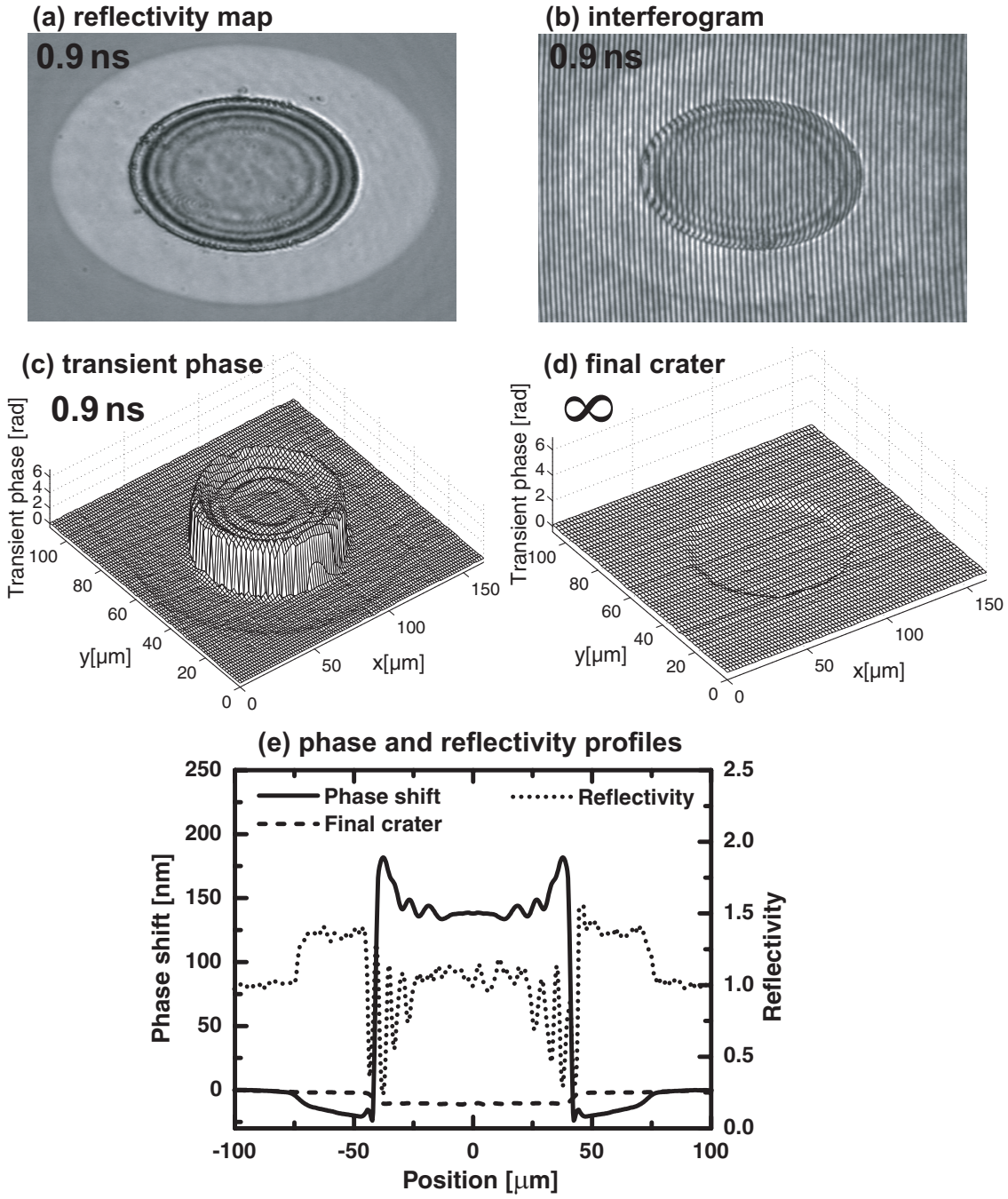

Figure 35: Example and results of time-resolved interferometric measurements at ablating Si-sufrace, $F = 1.3\ F_{thr}$, Δt=900 ps: (a) transient reflectivity map, (b) transient interferogram, (c) transient phase, (d) final crater, (e) spatial profiles of phase and reflectivity.

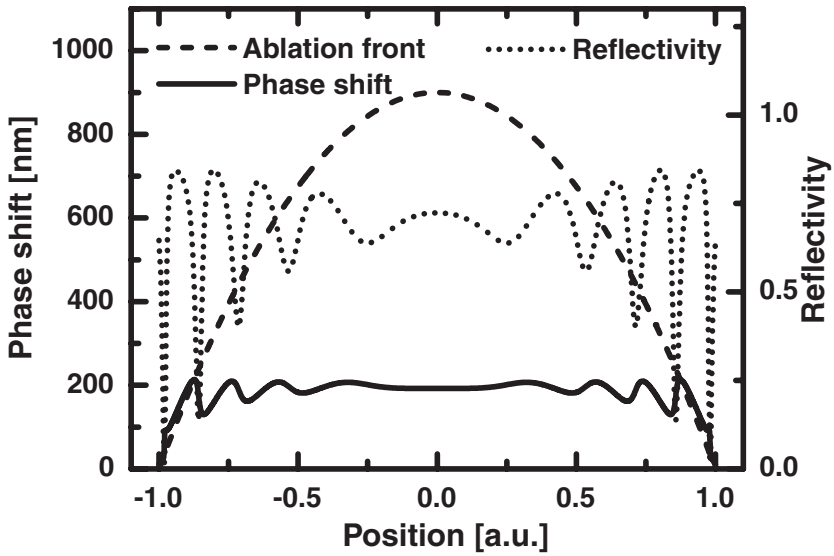

Figure 36: Thin-film calculations for spatial profiles of phase and reflectivity for a thin "bubble" with spatially varying thickness. The spatial profile of the ablation front (dashed) is assumed to be parabolic, whereas a "bubble" ($\tilde{n}_1 = 3.0 + 3.4i$) has a spatially varying thickness with $d_1(\pm 1)$ =10 nm, $d_1(0) = 1$ nm. The optical constants of the "bubble-like" model of Fig. 28(a) are: $\tilde{n}_1 = 3.0 + 3.4i$, $\tilde{n}_2 = 1$, $\tilde{n}_3 = 1.1 + 3.4i$.

tion. The spatial phase profile is very different from what we observe in GaAs, it can be hardly associated with the actual surface profile. We have performed extensive thin-film calculations and were able to generate phase and reflectivity profiles, which are qualitatively similar to those observed in the experiment. These simulated profiles are presented in Fig. 36. The position of the ablation front was assumed to have a parabolic spatial dependence with the maximum of 900 nm in the center of the ablating area (x=0) and zero at the threshold (x=$\pm$1). A "bubble" with spatially varying thickness $d_1(x)$ ($d(\pm 1) = 10$ nm, d(0)=1 nm) and $\tilde{n}_1 = 3.0 + 3.4i$ ($d(\pm 1) = 10$ nm, d(0)=1 nm) followed by a two-phase mixture with $\tilde{n}_2 = 1$ was assumed for the internal structure of the ablating layer, which was placed on the top of liquid Si, $\tilde{n}_3 = 1.1 + 3.4$.

At the crater boundary the "bubble" possesses a high reflection coefficient and an interferometrically measured phase follows the geometry of the ablation front. At some point (in space) the bubble becomes so thin that part most of the incident light is transmitted and reflected from the bottom, whereas the interferometrically measured phase follows the profile of the bottom. The decrease of the bubble thickness also models the reduction in contrast for the Newton rings.

The results of the above fitting procedure are complicated and not unique, although

the main features of the experimental data are reproduced. There are too many fit parameters and dozens of different parameter sets and spatial dependencies for the bubble thickness, which produce the same results. However, we were not able to get any similar phase and reflectivity profiles with a bubble of constant thickness, or a spatially homogeneous layer according to Maxwell-Garnett or a combination of them.

We have sketched here a few problems with interferometric measurements and their interpretation and do not want to continue it. It became clear at the very beginning of the interferometric measurements in silicon that they do not allow us to directly follow the dynamics ofthe ablation front in a desired range of excitation fluences $\sim 10 \div 30\%$ above the threshold. The main reason for this failure is a small crater depth, which inevitably requires that the bubble must be very thin and also suggests that the laser-molten layer is thin. This would also make the measurements of thermo-acoustic oscillations complicated, since the absolute value of the surface displacement is proportional to the thickness of laser-molten layer. Because of these obvious complications we decided not to carry out many time-dependent measurements performed for GaAs.

3.4.2 Extremely long reversible surface deformations of Si-surface excited a few percent below ablation threshold

The only successful interferometric measurement in silicon represents the dynamics of reversible surface deformations for excitations a few percent below ablation threshold shown in Fig. 37. Qualitatively the dynamics is very similar to that observed in GaAs: the closer to ablation threshold the larger is the time-scale and the amplitude of a fully reversible surface excursion. Quantitatively the maximally achieved excusion amplitudes and time-scales of the deformations are significantly smaller than in case of GaAs. We believe that this difference can be again attributed to a much smaller depth of laser-excited surface area in silicon.

However, it can be concluded that also in silicon the time-scale of subthreshold surface deformations is much longer than expected for simple thermo-acoustic behavior and most likely the reduction of density is quite substantial. Moreover, the available experimental data provide indications that the thickness of the laser-molten layer does not greatly exceed the skin-depth for the probe wavelength $\delta \sim$10 nm. This suggests that also in silicon substantial density reduction of the expanding liquid layer occurs, which indicates the importance of liquid-gas phase transition. Thus the experimental data for silicon do not contradict the scenario of surface dynamics presented for GaAs.

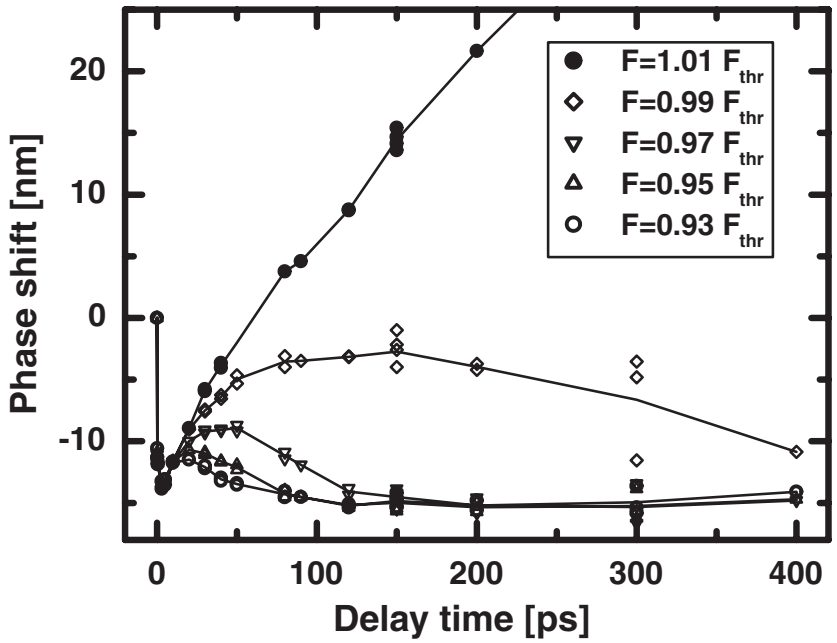

Figure 37: Dynamics of transient surface deformations of Si-surface for fluences very close to ablation threshold. The curves are automatically reconstructed from data sets with peak fluence $F = 1.3\ F_{thr}$ by integrating over the area of constant fluence.

3.5 Conclusions and future perspectives

In this chapter we have presented the results of ultrafast time-resolved interferometric investigations of GaAs- and Si-surfaces. The application of advanced fully automatic data processing algorithms allowed us to extract important physical information.

We have directly observed several types of transient surface deformations at fs-laser-excited GaAs-surface, which are (i) the damped thermo-acoustic oscillations of a laser-molten superficial layer of material for excitation 20% below threshold, (ii) extremely long large-amplitude reversible surface excursions a few percent below threshold and (iii) irreversible motion of a sharp ablation front above the threshold. The results of above-threshold measurements for excitation 30% above the threshold were used to test the two different models for the internal structure of the ablating plume: spatially homogeneous and inhomogeneous "bubble-like" structure. The results of optical thin-film simulations performed for both structures are in agreement with experimental data only for a "bubble"-like structure. Moreover, the 40 nm-thin bubble is found to possess the dielectric optical properties, which is essentially expected for low-density liquid GaAs. However, keeping in mind certain problems with a multiparameteric fitting procedure, more experimental measurements should

be performed in order to verify these very interesting, but preliminary observations. Our analysis shows that broadband optical spectroscopy would be an appropriate tool for such investigation.

Several important conclusions about surface dynamics could be deduced from the results of interferometric measurements in the vicinity of the ablation threshold. First of all, we observe the deceleration of initially fast surface motion during the first 100 ps after excitation both a few percent below and above the ablation threshold. This phenomena can be attributed to the contribution of tensile stresses (negative pressure) in a strongly expanded liquid.

Second, fully reversible large-amplitude surface deformations just below the threshold occur on a time-scale much larger than that of thermo-acoustic oscillations, which have been observed 20% below the threshold. A strong estimated reduction of the density of the expanding liquid suggests that the liquid-gas phase transition is likely to occur, which results in a dramatic decrease of the sound velocity and provides an explanation for the observed large time-scale of reversible surface motion.

The amount of physically relevant information, which we were able to extract from the interferometric measurements in GaAs more than fulfilled our initial expectations. Similar measurements performed in silicon appeared to be less successful: for example, we were not able to directly observe the movement of the ablation front. Most likely the failure of the measurements is predetermined by a much smaller thickness of ablating layer. The ablation craters in Si are only 7 nm deep (for comparison: in GaAs the crater depth reaches 50 nm). Therefore the thickness of the laser-molten layer and of the "bubble" cannot be much larger. The results of thin-film calculations show that the position of a very thin "bubble" cannot be measured interferometrically since its reflection coefficient is not high enough. However, the observed large-amplitude surface deformations in Si excited a few percent below the ablation threshold do also occur on a long time-scale $\tau >> \tau_{ac}$. This indicates that near-threshold surface dynamics in Si is the same as in GaAs.

Concluding this chapter we believe that the presented interferometric measurements represent the key to the understanding of the physical nature of the ablation threshold. Of course, more measurements should be performed in different well-characterized materials. Available experimental data indicate that interferometric measurements are most useful on materials with deep ablation craters.

Interferometric measurements on thin absorbing films on a dielectric substrate represent an interesting opportunity to generate a hot homogeneously excited liquid layer. The well-defined initial conditions would enable a direct comparison of the exper-

imental data with, for example, the simple theoretical model for thermo-acoustic oscillations.

4 Ionization of dielectrics by femtosecond laser pulses

4.1 Overview of known ionization mechanisms

When talking about laser-induced ionization of crystalline dielectrics specialists mean the generation of free carriers, i.e. electrons-hole pairs. Typical dielectric crystals possess the bandgap of the order of several eV, which is larger than the photon energy of visible or infrared laser radiation. Therefore, in order to enable the transfer of electrons from the completely filled valence band to the empty conduction band (electron-hole pair generation) several photons must be absorbed. The two most important ionization mechanisms are photoionization and avalanche ionization.

Photoionization assumes that an electron-hole pair is generated via the direct absorption of several photons. The minimal number n_{min} of absorbed photons of frequency ω is determined by the bandgap $\Delta < n_{min}\hbar\omega$. In 1965 L.V. Keldysh introduced a new concept of perturbation theory in quantum mechanics [66], which he applied to study photoionization in atoms and crystals and derived a general formula for the rate of photoionization, which appears to be a superposition of multiphoton processes of higher orders (i.e $n = n_{min}, n_{min} + 1, n_{min} + 2, ...$). Keldysh demonstrated that depending on the material and laser parameters his general ionization formula has two limiting cases known as multiphoton ionization of the lowest order n_{min} and tunneling ionization in a quasistatic electric field. Roughly speaking for relatively weak laser intensities multiphoton ionization of the lowest order dominates, whereas for high intensities it is the tunneling ionization. The borderline between these ionization mechanisms is determined not by intensity itself but by the so-called Keldysh parameter.

Avalanche ionization requires that a "seed"-electron already existing in the conduction band acquires kinetic energy by absorbing several photons from the laser field via free-carrier absorption. When its kinetic energy exceeds a certain critical value $E > E_{cr} > \Delta$ [67], it is able to generate an additional electron-hole pair by impact ionization, which is an inverse process to Auger-recombination. Because of the exponential growth in time of carrier concentration this ionization mechanism is called avalanche. The most comprehensive theory of impact ionization in solids was provided in 1960 also by Keldysh [68], who has derived an analytical solution of the Boltzmann equation for free-carrier distribution functions in an external electric field under certain approximations. A recent numerical solution of the Boltzmann

equation does also deserve attention [67]. Any realistic theory for impact ionization requires that the solution of a Boltzmann equation to be obtained, usually with many assumptions and simplifications, which is extremely complicated and we will not discuss it here for this reason.

Two important statements about avalanche ionization should be mentioned. First of all, since avalanche assumes the heating and multiplication of electrons in a time domain it requires the existence of some "seed"-electrons, which must be generated in the conduction band by a different ionization mechanism. Second, in order to be able to generate further electrons by impact ionization, the seed electrons need a certain amount of time to acquire a critical energy via free-carrier absorption. This delay-time of the avalanche is estimated to be around a few tens of femtoseconds but its exact value depends on the concrete parameters put into the model [67].

Both photoionization and avalanche ionization have been well studied in atomic physics. Keldysh's theory of photoionization gave rise to further successful theoretical research and stimulated the understanding of above-threshold ionization in atomic physics (ATI-spectra) [69]. A simple theory of laser-induced avalanche in gases is described in [70]. In solid-state physics, unfortunately, there has been no significant progress since Keldysh's works [66, 68, 71, 72, 73]. Jones and Reiss [74] claim that they have performed similar calculations to those of Keldysh but for solids ionized by a field of a strong circularly polarized wave. The basic assumptions underlying their formal calculations appear to be somewhat different from those of Keldysh's model and the comparison with Keldysh's model is practically absent. For this reason we have not studied the details of their rather complicated calculations. The only systematic study was the comparison of the predictions of Keldysh's approach with conventional calculations for one- and two-photon absorption rates in semiconductors [56, 75, 76, 77, 78], to be discussed further.

The reason for a relatively poor understanding of ionization mechanisms in solids as compared with atoms is quite clear: the interaction of atoms with radiation and associated phenomena are much more simple, transparent and better characterized in atomic physics as compared with solid state physics. Because of the intrinsic complexity of optical processes in solids many experimentalists try to directly apply Keldysh's model to fit their experimental data without taking into account its actual applicability limits [79, 80, 81].

In the following section we shall discuss in detail Keldysh's theory of the photoionization of solids, which aims to reveal the physical background of his model calculations and establish the applicability limits.

4.2 Physical background of Keldysh's theory of photoionization

A common way to treat intraband optical transitions in solid state physics is based on perturbation theory. The description of the interaction of a plane monochromatic electromagnetic wave with a solid within a dipole approximation, i.e. with interaction Hamiltonian of the form $H' = \mathbf{d} \cdot \mathbf{E}$, and use of Fermi's golden rule leads to the following well-known expression for the rate of transition from the valence band to the conduction band [82]:

$$w_{v\to c} = \frac{2\pi}{\hbar} \int \frac{d^3\mathbf{p}}{(2\pi\hbar)^3} |M_{cv}(\mathbf{p})|^2 \delta(\varepsilon(\mathbf{p}) - \hbar\omega) \tag{27}$$

with $M_{cv}(\mathbf{p}) = \langle \Psi^c_{\mathbf{p}} | H' | \Psi^v_{\mathbf{p}} \rangle$ being the matrix element of transition between the Bloch wave functions of the undisturbed crystal $\Psi^{c,v}_{\mathbf{p}} = u^{c,v}_{\mathbf{p}} \exp(\mathrm{i}\,\mathbf{pr}/\hbar)$ in the conduction and valence bands, respectively. The integral is taken over all states which obey the energy conservation law $\varepsilon(\mathbf{p}) = \hbar\omega$, where

$$\varepsilon(\mathbf{p}) = \varepsilon_c(\mathbf{p}) - \varepsilon_v(\mathbf{p})\,. \tag{28}$$

Keeping in mind the following property of a δ-function: $\int \delta(f(x))dx = \sum_{x_i} |(df/dx)_{x_i}|^{-1}$ with $f(x_i) = 0$, it can be shown that the transition rate (27) is proportional to the so-called joint density of states $\propto |\nabla_{\mathbf{p}} \varepsilon|^{-1}$.

Formula (27) represents the result of first-order perturbation theory. If the photon energy is smaller than the bandgap, the expression (27) turns to zero indicating that one-photon absorption is forbidden. To obtain the expression for the rate of multiphoton absorption, a perturbation theory of high order must be applied. Due to the significantly larger amount of efforts required to calculate the rate of multiphoton ionization using high order perturbation theory, calculations were made for a maximum of 4 photons [83, 84].

The brilliant idea of Keldysh was to apply time-dependent first-order perturbation theory considering the transition not between *unperturbed* Bloch states, but between *perturbed* states which take into account the acceleration of electrons and holes in the electric field of the electromagnetic wave. Similar states first introduced by Volkov for free electrons accelerated in vacuum [85] have been generalized for Bloch-electrons in a solid by Houston [86].

The electric field of the electromagnetic wave, periodically varying in time

$$\mathbf{F}(t) = \mathbf{F} \cos \omega t \tag{29}$$

induces the periodic temporal dependence of quasimomentum for both the electron and the hole:

$$\mathbf{p}(t) = \mathbf{p} + \frac{e\mathbf{F}}{\omega}\sin\omega t\,. \tag{30}$$

Bloch wave functions of an electron, accelerated by the field inside each of the bands have the form:

$$\Psi^{c,v}_{\mathbf{p}}(\mathbf{r},t) = u^{c,v}_{\mathbf{p}(t)}(\mathbf{r})\exp\left(\frac{\mathrm{i}}{\hbar}\Big[\mathbf{p}(t)\mathbf{r} - \int_0^t \varepsilon_{c,v}(\mathbf{p}(\tau))d\tau\Big]\right), \tag{31}$$

where $u^{c,v}_{\mathbf{p}}(\mathbf{r})$ are periodic functions that have the translational symmetry of the lattice. It is important to notice that states (31) possess both the time-dependent quasimomentum and time-dependent energy. For this reason it is natural to apply time-dependent perturbation theory. Keeping the notation from Keldysh's original paper [66], the transition rate in the first-order time dependent perturbation theory reads:

$$\begin{aligned} w_0 &= \frac{1}{\hbar^2}\lim_{T\to\infty}\mathrm{Re}\int\frac{d^3\mathbf{p}}{(2\pi\hbar)^3}\int_0^T dt\cos\omega T\cos\omega t\, V_0^*\Big(\mathbf{p}+\frac{e\mathbf{F}}{\omega}\sin\omega T\Big) \\ &\times\ V_0\Big(\mathbf{p}+\frac{e\mathbf{F}}{\omega}\sin\omega t\Big)\exp\Big[\frac{i}{\hbar}\int_T^t\varepsilon\Big(\mathbf{p}+\frac{e\mathbf{F}}{\omega}\sin\omega\tau\Big)d\tau\Big] \end{aligned} \tag{32}$$

with the transition matrix element given by

$$V_0(\mathbf{p}) = i\hbar\int u^{c*}_{\mathbf{p}}(\mathbf{r})e\mathbf{F}\nabla_{\mathbf{p}}u^{v}_{\mathbf{p}}(\mathbf{r})d^3\mathbf{r}\,. \tag{33}$$

It should be noted that Keldysh did not mention how he estimated the transition matrix elements, except for writing down the final contribution of the matrix element to the contour integral (see Eq. (32) in [66]), to be discussed later. The limiting case of Keldysh's approach for one-photon absorption is found to coincide with the formula obtained by conventional perturbation theory [75, 76]. The conventional calculations for one-photon absorption [75] make use of the so-called **kp**-method [89] to evaluate the matrix transition element (33), suggesting that Keldysh used the same approximation.

It is quite difficult to interpret the expression (32) except for mentioning that it represents a temporal average of many oscillating terms. It appears to be important to introduce the following quantity:

$$L(\mathbf{p},t) = V_0\Big(\mathbf{p}+\frac{e\mathbf{F}}{\omega}\sin\omega t\Big)\exp\Big[\frac{i}{\hbar}\int_0^t\Big(\varepsilon\Big(\mathbf{p}+\frac{e\mathbf{F}}{\omega}\sin\omega\tau\Big)-\overline{\varepsilon(\mathbf{p})}\Big)d\tau\Big]\,, \tag{34}$$

with

$$\overline{\varepsilon(\mathbf{p})} = \frac{1}{2\pi}\int_{-\pi}^{\pi}\varepsilon\Big(\mathbf{p}+\frac{e\mathbf{F}}{\omega}\sin x\Big)dx \tag{35}$$

being the averaged over time energy difference between the two perturbed Bloch states (31). Substituting the representation of (34) in terms of its Fourier expansion with respect to time

$$L(\mathbf{p},t) = \sum_{n=-\infty}^{\infty} L_n(\mathbf{p}) \exp(-in\omega t) \tag{36}$$

into (32) leads to the following final result for the desired transition rate:

$$w_0 = \frac{2\pi}{\hbar} \int \frac{d^3\mathbf{p}}{(2\pi\hbar)^3} \sum_{n=-\infty}^{\infty} \frac{1}{4} |L_{n+1}(\mathbf{p}) + L_{n-1}(\mathbf{p})|^2 \, \delta(\overline{\varepsilon(\mathbf{p})} - n\hbar\omega) \, . \tag{37}$$

Thus the transition rate represents the sum of the multiphoton processes of different orders

$$\overline{\varepsilon(\mathbf{p})} = n\hbar\omega \, . \tag{38}$$

Note that the unperturbed band structure $\varepsilon(\mathbf{p})$ (28) is replaced by the *modified band structure* $\overline{\varepsilon(\mathbf{p})}$ (35), in which the fast oscillatory motion of the electron in the electric field of the wave is averaged out. It can be recognized that the *joint density of states* for the *modified band structure* plays a similar role to that of the conventional joint density of states in the usual semiconductor optics described by Eq. (27). The probability of the multiphoton transition is given by coefficients of Fourier expansion $L_n(\mathbf{p})$ (36). It is possible to provide an intuitive explanation for the physical meaning of these coefficients: the quantity $L(\mathbf{p},t)$ of Eq. (34) is the product of the two terms. The first amplitude term $V_0(\mathbf{p}(t))$ is the matrix dipole moment of the transition, which is in general time-dependent. Indeed, the dependence of the periodic part of the Bloch function on quasimomentum results in the dependence of the transition matrix element on quasimomentum. Since the quasimomentum oscillates in time, the transition matrix element must oscillate also. However, it is commonly believed that matrix transition elements are smooth and slowly varying functions of quasimomentum which could be replaced by a constant [82].

The second exponential term, or phase term, in (34) represents the time-dependent *detuning* from the resonance due to inevitable temporal energy variations of the oscillating electrons. Alternatively Eq. (34) can be interpreted in such a way that the transition dipole moment exhibits a strong temporal modulation of the *phase*, which leads to the generation of high-order harmonics in the Fourier spectra even if temporal energy variation is purely harmonic! It is clear that the Fourier expansion coefficients $L_n(\mathbf{p})$, which determine the probability of multiphoton transitions, will be sensitive to the discussed temporal evolution of the phase. For strong fields,

when electron oscillation amplitude is a significant fraction of the Brillouin zone, the temporal energy variation becomes unharmonic and is determined by the properties of the band structure.

We believe that formula (37) represents the main result of Keldysh's approach. The meaning of all physical quantities entering into (37) is clear, any band structure can be put into it. However, the significance of exact calculations of the transition matrix elements in Kedlysh's approach and the role of the band structure remain poorly understood. The straightforward numerical evaluation of the ionization rate using expression (37) does not seem to involve significant computational difficulties and, therefore, represents an interesting project for future research.

Since Keldysh did not have a computer he had to evaluate the expression (37) analytically. Using the following specific band structure, known as Kane's model [87, 88]:

$$\varepsilon(\mathbf{p}) = \Delta\sqrt{(1+\mathbf{p}^2/m\Delta)}\,, \tag{39}$$

where Δ represents the (direct) bandgap and

$$m = \frac{m_e m_h}{m_e + m_h}\,, \tag{40}$$

stands for a reduced electron-hole effective mass, Keldysh converted the expression (37) to a contour integral over the complex plane and evaluated it using the saddle-point approximation. The result of these rather complicated mathematical calculations is represented by the final formula for the ionization rate [66]:

$$w_0 = \frac{2\omega}{9\pi}\Big(\frac{\sqrt{1+\gamma^2}}{\gamma}\frac{m\omega}{\hbar}\Big)^{3/2} Q\Big(\gamma, \frac{\tilde{\Delta}}{\hbar\omega}\Big) \exp\left[-\pi\Big\langle\frac{\tilde{\Delta}}{\hbar\omega}+1\Big\rangle\frac{K(\phi)-E(\phi)}{E(\theta)}\right], \tag{41}$$

$$Q(\gamma,x) = \sqrt{\frac{\pi}{2K(\theta)}}\sum_{n=0}^{\infty}\exp\Big[-\pi\frac{K(\phi)-E(\phi)}{E(\theta)}n\Big]\Phi\left(\sqrt{\frac{\pi^2[\langle x+1\rangle - x + n]}{2K(\theta)E(\theta)}}\right), \tag{42}$$

with

$$\tilde{\Delta} = \frac{2}{\pi}\Delta\frac{\sqrt{1+\gamma^2}}{\gamma}E(\theta)\,, \tag{43}$$

$$\theta = \frac{1}{\sqrt{1+\gamma^2}}\,, \phi = \frac{\gamma}{\sqrt{1+\gamma^2}}\,, \Phi(z) = \int_0^z \exp(y^2-z^2)dy\,, \tag{44}$$

where functions K and E are complete elliptic integrals of the first and the second kind [90] and $\langle x\rangle$ represents the integer part of x. The famous Keldysh parameter

$$\gamma = \frac{\omega\sqrt{m\Delta}}{eF} \tag{45}$$

sets the borderline between the two limiting cases of the general ionization formula (41). For $\gamma >> 1$ Eq. (41) converges against

$$w_0 = \frac{2\omega}{9\pi}\Big(\frac{m\omega}{\hbar}\Big)^{3/2}\Phi\Big[\sqrt{4\Big\langle\frac{\tilde{\Delta}}{\hbar\omega}+1\Big\rangle-\frac{4\tilde{\Delta}}{\hbar\omega}}\Big] \times \exp\Big[2\Big\langle\frac{\tilde{\Delta}}{\hbar\omega}+1\Big\rangle\Big(1+\frac{e^2F^2}{4m\omega^2\Delta}\Big)\Big]\Big(\frac{e^2F^2}{16m\omega^2\Delta}\Big)^{\langle\tilde{\Delta}/\hbar\omega+1\rangle}, \quad (46)$$

which is the usual multiphoton ionization of the lowest order. The probability of multiphoton processes of higher orders is negligibly small. Formula (46) has been corrected for misprints by V.E. Gruzdev, who has completely verified Keldysh's calculations [91]. Multiphoton ionization of the lowest order is a well-known process, which can be accurately treated using parabolic approximation of band extremuma. For $\gamma << 1$ the general formula (41) contains many multiphoton processes of higher orders, which have comparable probabilities so that the sum (42) can be replaced by an integral providing the second asymptotic limit

$$w_0 = \frac{2\omega}{9\pi^2}\frac{\Delta}{\hbar}\Big(\frac{m\omega}{\hbar}\Big)^{3/2}\Big(\frac{e\hbar F}{m^{1/2}\Delta^{3/2}}\Big)^{5/2}\exp\Big[-\frac{\pi}{2}\frac{m^{1/2}\Delta^{3/2}}{e\hbar F}\Big(1-\frac{1}{8}\frac{m\omega^2\Delta}{e^2F^2}\Big)\Big], \quad (47)$$

which is directly related to the tunneling effect in solids in a constant (DC) electric field [71]. Physical interpretation of Eq. (47) suggests [66] that for each time moment during the optical cycle the electric field of the wave can be considered as *quasistatic* and, therefore, the instantaneous ionization rate is given by the tunneling rate in a DC-electic field [71]. Formula (47) represents a tunneling rate in a DC-electric field averaged over one optical cycle. At this point it must be pointed out that a well-known expression for tunneling ionization in a DC-electric field, often referred to as the Franz-Keldysh effect, is also obtained with some approximations (expansion in powers of quasimomentum) for the band structure. Keldysh's original paper [71] does also contain a general formula for an arbitrary band structure, which can be evaluated numerically. Such a study has not been conducted so far.

However, the general Keldysh expression for photoionization rate (41) remains the only available formula, which is widely used to fit experimental results. Figure 38 represents the dependence of ionization rate (Eq. (41)) on laser intensity together with the two asymptotic curves for multiphoton (Eq. (46)) and tunneling ionization (Eq. (47)) for the following laser and material parameters: $\hbar\omega = 1.55$ eV ($\lambda = 800$ nm), $\Delta = 9$ eV, $m = 0.5m_e$, $n_0 = 1.45$. The relation between the intensity I[W/cm^2] and peak electric field F[V/cm] of a linearly polarized electromagnetic wave is given by

$$I = \frac{1}{2}n_0\varepsilon_0 cF^2, \quad (48)$$

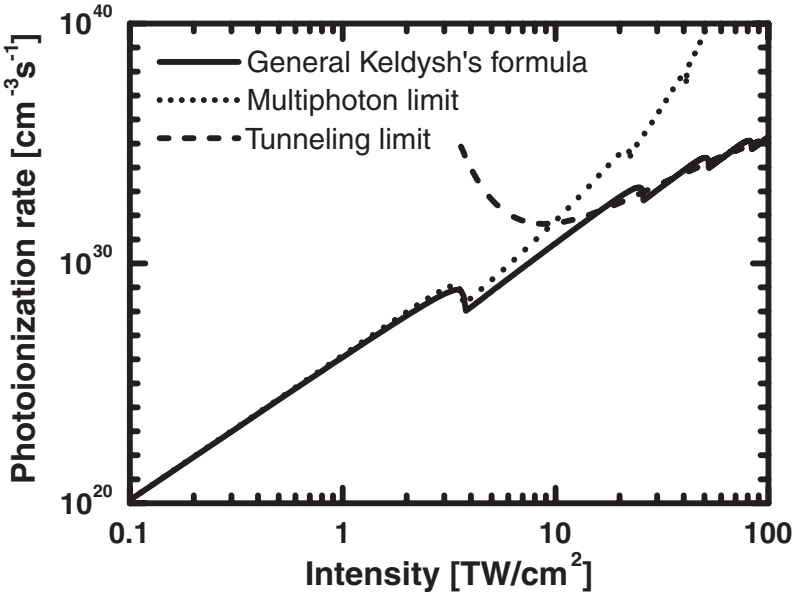

Figure 38: Rate of photoionization according to Keldysh's formula (Eq. (41)) versus laser intensity together with the two asymptotic curves for multiphoton (Eq. (46)) and tunneling ionization (Eq. (47)) for the following laser and material parameters: $\hbar\omega = 1.55$ eV, $\Delta = 9$ eV, $m = 0.5m_e$, $n_0 = 1.45$.

where n_0 is the linear index of the refraction of a medium, ε_0 is the dielectric permittivity of vacuum and c is the speed of light in vacuum. It can be seen in Fig. 38 that for low intensities the ionization rate scales as $w \propto I^6$, characteristic for multiphoton ionization, since the minimal number of photons needed to cross the band gap is $\langle 1 + \Delta/\hbar\omega \rangle = 6$. As expected, for low intensities the general Keldysh formula (41) coincides with the multiphoton limit (46). One remarkable feature characteristic of both the general Keldysh formula and its multiphoton approximation is the presence of many small "jumps" for higher intensities. Apart from crossing the usual band gap, some additional oscillatory (ponderomotive) energy must be supplied to the electrons because they oscillate in a strong external optical field. This leads to the appearance of the effective band gap $\tilde{\Delta}$ (see Eq. (43)) in Keldysh's theory, which exceeds the conventional band gap Δ by the value equal to the ponderomotive energy of the electrons. The ponderomotive energy does naturally become larger with increasing intensity. Therefore, the characteristic "jumps" in Fig. 38 are due to a step-like increase in the number of photons needed to cross the effective band gap, i.e. from 6 to 7, 7 to 8 photons and so on.

For high intensities above 10 TW/cm^2 for a given set of parameters the ionization rate (41) converges against the tunneling approximation (47). The tunneling approximation shows no "jumps" since it is constructed within the limit of a quasistatic

electric field.

Graphs like that of Fig. 38, which represent the dependence of Keldysh's photoionization rate on laser intensity are often discussed in relation with experimental studies of optical breakdown by ultashort laser pulses [79, 80, 81]. According to available experimental data the threshold for optical breakdown of dielectric surfaces by femtosecond laser pulses lies in the range of a few times 10^{13} W/cm^2 with little variation on material parameters [28]. For typical material and laser parameters such as the ones we used, this corresponds to the transition from multiphoton ionization to tunneling ionization, which makes speculations utilizing Keldysh's photoionization formula to explain the experimental observations very attractive.

At this point it is important to mention the general limitation of Keldysh's approach with respect to the maximally allowed strength of the electric field. Being the starting point of Keldysh's calculations, perturbed Bloch states (31) are valid only for laser fields which are small compared to the crystal field, which determines the properties of the band structure [82]. A reasonable estimate for the crystal field is given by

$$F_{cryst} = \frac{\Delta}{ed}\,, \tag{49}$$

where d stands for the lattice constant. For typical dielectrics like quartz or aluminum oxide (sapphire) $d \simeq$0.5 nm, $\Delta \simeq$9 eV we obtain $F_{cryst} = 180$ MV/cm corresponding to laser intensities of about 60 TW/cm^2 [91]. Therefore the applicability of Keldysh's approach for laser intensities in the vicinity of optical breakdown threshold appears to be questionable.

An interesting question is how big is the amplitude of quasimomentum oscillation driven by such high laser field compared to the size of the Brillouin zone. A characteristic electric field amplitude required to drive an electron through the whole Brillouin zone reads:

$$F_{Br} = \frac{\pi\hbar\omega}{ed}\,. \tag{50}$$

The ratio

$$\frac{F_{Br}}{F_{cryst}} = \frac{\pi\hbar\omega}{\Delta} \sim 1 \tag{51}$$

depends only on band gap and laser frequency and is of the order of unity for visible or near-infrared radiation. For strong fields, at which the electron starts to oscillate through the whole Brillouin zone, the approximation on undisturbed band structure, which is assumed in Keldysh's model, breaks down. Formula (51) does also suggest that for smaller photon energies Keldysh's ionization theory remains applicable even for large-amplitude electron oscillations, where the details of the band

structure will play a dominant role. Experiments utilizing excitation of dielectrics by intense ultrashort infrared laser pulses could serve as a test for strong-field Keldysh's photoionization theory. Sources of such radiation based on optical parametric amplification using standard Ti:Sa near-infrared optical pulses are already available.

The last limitation of Keldysh's approach, to be discussed, is that it completely disregards any electronic collisions. This assumption is justified when the electronic collision time is large compared to the period of the optical cycle. In case of atoms the homogeneous broadening of atomic levels is taken into account by replacing the δ-functions in Keldysh's formula for the ionization rate (which is similar to Eq. (37) for solids) by Lorentzians with corresponding width [69]. We believe that seldom electronic collisions in solids might be taken into account in the same way. However, as will be shown in next section, the experimentally measured and theoretically predicted collision rates appear to be quite big, so that "collisional broadening" (in the sense of laser physics [92]) exceeds the light frequency. The concept of "collisional broadening" of electronic states due to extremely short collision times was introduced and extensively discussed by Fischetti at al. [93], who have also presented and discussed in detail the Monte-Carlo simulations for high-field carrier transport in the isolators. It seems to be possible to incorporate such frequent collisions in Keldysh's theory by the direct modification of initial states (31), in which the coherent evolution of electronic wave functions in the external field will by interrupted by successive collisions. As the implementation of such purely numerical Monte-Carlo simulations are absolutely necessary to correctly interpret experimental data, this represents an issue for separate theoretical research, although a lot of technical work has already been done in [93].

Finally, we want to mention the results obtained by Vaidyanathan and co-workers [56] who have calculated the two-photon absorption rate in some semiconductors using realistic energy bands and transition matrix elements, which are obtained from the detailed band structure calculations. Being in a good agreement with experimentally measured two-photon absorption rates, the results of their calculations strongly differ from the predictions of Keldysh's theory. This finding suggests that Keldysh's ionization model is indeed very sensitive to the details of band structure.

Recently Keldysh-type calculations have been presented, which describe ionization of quantum wells by intense laser fields [88, 94]. These calculations predict some specific effects due to the presence of natural potential barriers forming a quantum well (a good example of a quantum well is an AlGaAs/GaAs/AlGaAs-heterostructure). For such types of structures the effects due to the exact band structure of bulk

compounds and high scattering rates are likely to be dominated by the structure of the potential energy of a quantum well and, therefore, the predictions of the theory [88, 94] can be tested in the experiment.

4.3 State-of-the-art in experimental studies of laser-induced ionization

Most of the previously reported studies on laser-induced ionization of dielectrics by ultrashort laser pulses are optical studies. They can be divided into three categories: (i) investigation of breakdown thresholds via post-mortem analysis of laser-irradiated surface and/or volume areas as a function of laser and material parameters, (ii) numerical simulations of ultrashort pulse propagation through the nonlinear dispersive dielectric media that can be ionized and (iii) dynamical studies monitoring the temporal evolution of the optical properties within a laser-excited region.

The first group, i.e. investigations of breakdown thresholds, exploits the close relation between the phenomena of optical breakdown and the generation of high-density free carriers by laser-induced ionization. It is commonly believed that in order to produce optical breakdown in solids the generation of overcritical (in the sense of plasma physics) carrier density is required which is of the order of 10^{21} cm^{-3} for 800 nm. At such high concentrations the plasma becomes opaque, exhibiting a strong absorption which allows a significant amount of laser energy to be absorbed in a small volume leading to destruction of the material. This interpretation is analogous to that developed for optical breakdown in gases [70].

One of the big questions was the absence of optical breakdown in bulk dielectrics irradiated by femtosecond laser pulses under "normal" focusing conditions, whereas for pulses longer than a few picoseconds the permanent damage in the form of typical breakdown "cracks" was observed [28]. To explain this behavior the propagation effects of intense ultrashort laser pulses in a nonlinear dispersive medium have been considered such as self-phase modulation, self-focusing, dispersive broadening and, of course, different mechanisms of laser-induced ionization. The results of highly complicated numerical simulations suggest that the overcritical carrier concentration can never be reached, due to the fact that already at modest electron concentrations $\sim 10^{20}$ cm^{-3} the electron gas acts as a defocusing lens for the pump beam, which effectively stops further development of the ionization process [81]. The original idea that defocusing by laser-generated electron gas in a solid is able to compensate for self-focusing by leading to formation of stable filaments is discussed in a classical paper by Yablonovitch and Bloembergen [95]. It has also been demonstrated that

for "tight" focusing conditions, in which the laser pulse is focused by a high-NA microscope objective into the tiny spot of submicron size, the propagation effects can be neglected and traces of optical breakdown in the form of permanent damage can be observed [80, 96]. The basic idea is that under tight focusing conditions a high intensity can be reached in focus, even when keeping the laser power below the critical power for self-focusing and, therefore, avoiding it [28, 80].

However, this type of investigation appears not to be sensitive to the mechanisms of laser-induced ionization. For example, the authors were able to explain similar experimental observations in fused silica by considering either 5-photon-absorption in [97] or 6-photon absorption [81]. In the latter paper experimental results were fitted by the general Keldysh formula using the effective mass as a fit parameter: $m^* = 0.635 m_e$. Since small variations of the effective mass result in huge variations of Keldysh's ionization rate (to be discussed later), such fit is meaningless.

In summarizing these criticisms we would like to stress that measurements of breakdown and/or permanent material modification thresholds appear to be rather insensitive to different ionization mechanisms since (i) the ionization rate exhibits a strong dependence on laser intensity for *any* of previously discussed mechanisms and (ii) there are too many unknown "fit"-parameters.

The second group of investigations is represented by purely numerical simulations of ultrashort pulse propagation through a dielectric including the propagation effects mentioned above [98, 99, 100, 101]. To obtain a correct solution to a 3-dimensional nonstationary partial differential equation of second order with diverse nonlinear terms is really a difficult task.

According to our knowledge, the third group of ultrafast time-resolved investigations is restricted, apart from [28], to a few experimental reports by French scientists currently guided by Philippe Martin [9, 102, 103]. The main idea of these investigations is based on the fact that the interaction of an intense laser field with a dielectric material induces *ultrafast* changes to its optical properties. The most important processes leading to changes of the complex index of refraction are the optical Kerr-effect and the generation of free carriers as a result of ionization:

$$\tilde{n} = n_0 + \Delta\tilde{n}_{Kerr} + \Delta\tilde{n}_{Drude}\,. \tag{52}$$

The optical Kerr-effect is responsible for self-phase modulation and self-focusing [70] and induces a real positive contribution to the complex refractive index

$$\Delta\tilde{n}_{Kerr} = n_2 I\,, \tag{53}$$

which is proportional to laser intensity I with n_2 being the nonlinear refractive index.

Free-carrier contribution can be described by the Drude-model:

$$\Delta\tilde{n}_{Drude} = -\frac{1}{2n_0}\Big(\frac{\omega_{pl}}{\omega}\Big)^2 \frac{1}{1-1/i\omega\tau_c}\,, \tag{54}$$

where $\omega_{pl} = \sqrt{e^2\rho/\varepsilon_0 m^*}$ stands for the plasma frequency. The two most important parameters of the plasma are Drude collision time τ_c and free-carrier density ρ. The reduced electron-hole mass m^* given by Eq. 40 originates from the concept of the effective mass and is usually not known precisely. This is why it is often assumed to be of the order of a free electron mass for both crystalline and disordered dielectrics. Although the concept of band structure does not exist for disordered solids like fused silica, the effective mass can be introduced as a measure for mobility $\mu = e\tau_c/m^*$ of free carriers (mobility effective mass).

It appears to be possible to extract useful information about the dynamics of the electron density from the temporal evolution of the complex refractive index, which can be measured interferometrically. At this point we want to briefly discuss some recent results by Quere et al. [103], who applied spectral interferometry to directly observe the dynamics of free carriers. The schematic of their experimental setup for spectral interferometry is shown in Fig. 39. An intense femtosecond pump pulse is used to excite a large superficial volume of a dielectric sample. Two identical 60 fs pulses, separated by a fixed delay time of the order of a few *ps*, are focused in the center of the laser-excited area and used to probe laser-induced refractive index changes. The phase shift accumulated over the whole inhomogeneously excited area along the probe path L in Fig. 39(a) represents the final result of interferometric measurements. Typical results of interferometric measurements reported in [103] are presented in Fig. 39(b). For two different materials, fused silica and sapphire, the temporal evolution of phase shifts and the dependence of carrier concentration at positive pump-probe delay time on laser intensity have been measured. Big fluctuations of data points are apparent in both graphs in Fig. 39(b). Nevertheless, the authors claim that they have clearly observed the 6-photon ionization at low intensities: the straight solid lines represent the expected dependencies of 6-photon ionization for both materials. It should be mentioned that in a previous publication [9] the same authors explained the experimental data by 5-photon absorption. Thus, the question about the actual ionization mechanism at low intensities has remained open until know. At high intensities the authors report deviations from the multiphoton ionization law and discuss some possible explanations [103].

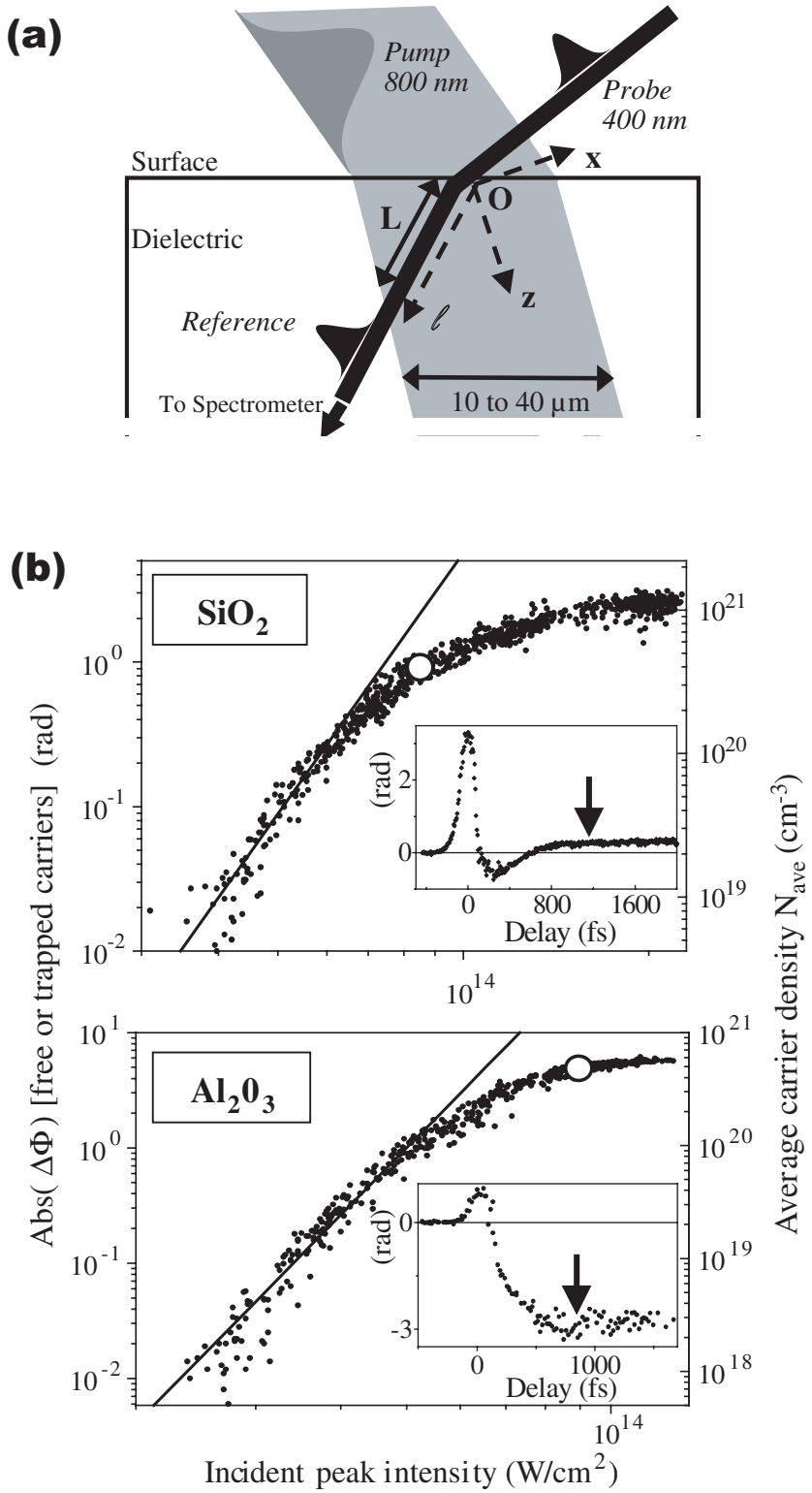

Figure 39: (a) Schematic of experimental setup for time-resolved spectral interferometry by Qeure at al. [103] and (b) results obtained by this technique [103](see text for details).

4.4 Setup for time-resolved Mach-Zehnder interferometry

In order to study the temporal evolution of the complex index of refraction in dielectrics induced by femtosecond laser pulses we have developed a setup for ultrafast time- and space-resolved Mach-Zehnder interferometry. The schematic of the experimental setup is presented in Fig. 40. The imaging interferometer consists of a Mach-Zehnder interferometer and a high-resolution microscope objective. A thin optically transparent dielectric sample, which is excited by an intense femtosecond laser pulse (Ti:Sa, 10 Hz, 800 nm, 50 fs) is positioned in the object arm of an interferometer. The focusing conditions for the pump pulse and the thickness of the sample have been chosen in such a way that excitation of the sample is spatially homogeneous. The time-delayed collimated probe pulse (400 nm, 50 fs) illuminates the excited area of the sample as shown in Fig. 40. The back surface of the sample is imaged on the CCD-chip, which is used to record interferograms formed by interfering probe and reference pulses. It is possible to reconstruct phase shifts and amplitude changes from the interferograms by using the 2D-Fourier transform algorithm in the same way as described in Chapter 2 for the Michelson interferometry. Under certain conditions, the reconstructed phase shifts and amplitude changes of the interference fringes can be interpreted as the actual phase shifts and transmission changes of the probe pulses. This issue will be discussed later on the basis of experimental data.

By choosing the collinear pump-probe geometry we are able to avoid spatial averaging effects in the transverse direction. Spatial averaging occurs in the propagation direction only, along which the phase shifts and amplitude changes are accumulated. Minimization of spatial averaging effects represents a big advantage as compared with previously reported interferometric setups [9, 103] (see, for example, Fig. 39(a)).

Some technical aspects of the experimental setup deserve particular attention. Pump pulses were focused in a 60 μm big spot on the sample surface under normal incidence through a thin dichroic mirror (to be explained later). The intensity of the pump pulses can be continuously varied by a combination of a $\lambda/2$-plate and reflecting polarizers in the range between 1-50 TW/cm^2. In contrast to thick crystal polarizers, which could produce strong temporal and probably also spatial distortions of intense light pulses due to the optical Kerr-effect (self-phase modulation and self-focusing), the reflecting polarizers do not influence the quality of the pump pulses.

One optical component, which has been especially designed for this experiment, is a thin dichroic mirror. Positioned between the pump focusing lens (f=30 cm) and the sample (see Fig. 40) it is used to reflect probe pulses and couple in pump

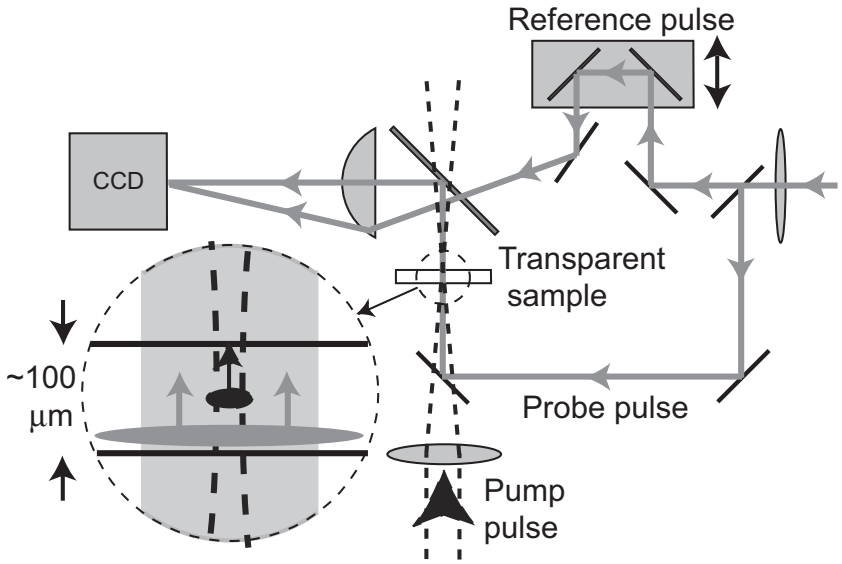

Figure 40: Schematic of experimental setup for ultrafast Mach-Zehnder interferometry.

pulses. It consists of a glass substrate covered with one reflecting dielectric coating for λ =400 nm @ 45° and two anti-reflecting coatings for λ =800 nm @ 45°. The dichroic mirror is positioned between the focusing lens and the sample and, therefore, must withstand really high intensities of partially focused pump pulses. In order to prevent the distortions of the intense pump pulses mentioned above we have minimized the thickness of the glass substrate by using a 200 μm-thin microscope cover glass. When trying to use a dichroic mirror manufactured on a standard 6 mm-thick glass substrate, we were able to observe the generation of white light in the mirror itself! The generation of white light in transparent materials is accompanied by strong self-phase modulation and self-focusing [104].

Temporal resolution of the technique is given by the duration of the probe pulses, which can be determined from the duration of the pump-probe cross-correlation function measured by means of a Kerr-shutter [70]. The operation principle of the Kerr-shutter is based on light-induced anisotropy: pump-induced refractive index changes due to (instantaneous) optical Kerr-effect appear to be anisotropic. Given a proper relative orientation of polarization planes and temporal overlap of pump and probe pulses, the polarization state of the probe pulse is changed in a manner as if it were passing through a conventional wave-plate. The goal is to measure the changes in the polarization state of the probe as a function of pump-probe delay time (cross-correlation function).

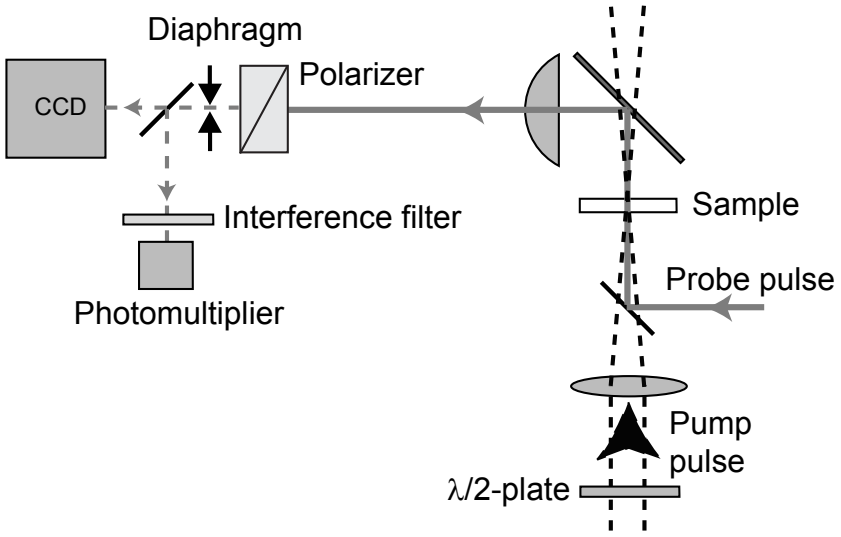

Figure 41: Setup for the measurement of pump-probe cross-correlation function.

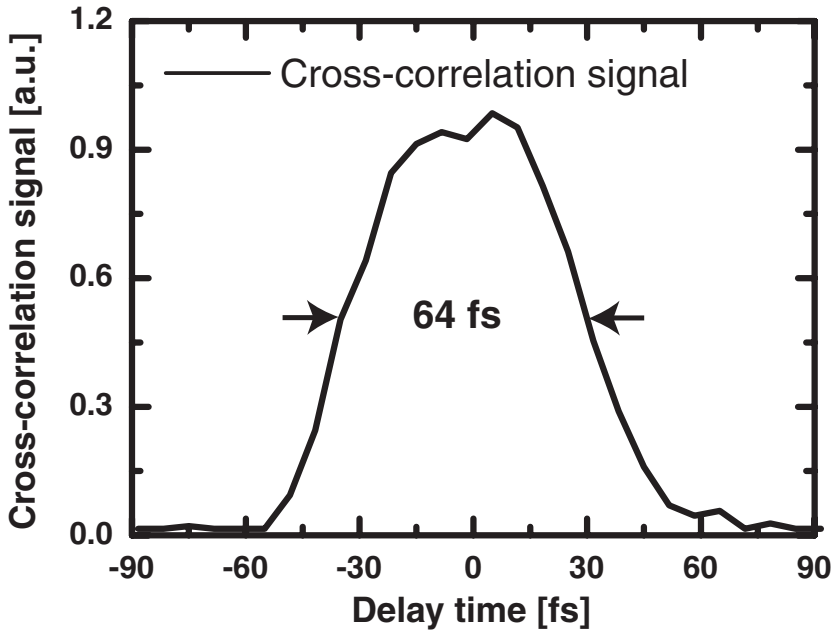

Figure 42: Typical pump-probe cross-correlation function measured in 100 μm-thick sapphire sample.

In order to measure the cross-correlation function we have slightly modified the interferometric setup, which is sketched in Fig. 41. The reference arm of the interferometer is blocked. After passing through the unexcited sample the s-polarized probe beam is blocked by a crystal polarizer positioned after the microscope objective. The polarization vector of the pump is rotated by 45 degrees with respect to the probe pulse with help of an additional $\lambda/2$-plate positioned in front of the focus-

ing lens (see Fig. 41). Due to the change in the polarization state some fraction of the probe pulse is transmitted through the polarizer and acquired by an integrating detector (in our case with a photomultiplier):

$$G_{cross}(\Delta t) \sim \int_{-\infty}^{\infty} I_{probe}(t) I_{pump}^2(t+\Delta t) dt\,, \tag{55}$$

where Δt denotes the pump-probe delay time. The transmitted fraction of the probe beam was simultaneously monitored by a CCD-camera and detected by the photomultiplier (using a beamsplitter). Since the laser-excited area is quite small, we adjust a diaphragm to select the signal only from the central part of the laser-excited spot. The use of a diaphragm helps to cut off the background illumination produced by probe radiation transmitted through the unexcited sample due to the finite extinction ratio of the polarizers. The level of this residual transmission is, of course, much smaller as compared to the cross-correlation signal. However, being integrated over the whole illuminated area (probe beam diameter on the sample is much bigger than pump-excited area), it would produce a strong background. Other possible sources of background illumination, not related to probe pulses are cancelled by the narrow-band interference filter for central wavelength λ=400 nm placed in front of the photomultiplier.

On-line monitoring of transmitted probe pulses on a CCD-camera appeared to be extremely helpful, not only to correctly position the diaphragm, but also to keep the the pump intensity at relatively low level, for which the Eq. 55 is valid [70]. For high pump intensities transmitted probe pulses show a sequence of dark and bright rings within the laser-excited area.

An example of a background-free cross-correlation function measured in a 100 μm-thick sapphire sample presented in Fig. 42 has the duration of τ_{cross}=64 fs (FWHM). This curve has been measured automatically within the LABVIEW-environment: the photomultiplier signal (10 Hz pulse train) integrated by computer-controlled analog-to-digital-converter (ADC) was averaged over many pulses for several seconds for each pump-probe delay. Between the successive acquisitions the delay time was synchronously moved by a step-motor controller with the minimal possible step of 6.67 fs.

In order to estimate the duration of the probe we have directly characterized the temporal shape of the pump pulses at the position of the sample (τ_{pump}=50 fs FWHM) by frequency-resolved optical gating (FROG)[105]. The pump pulses did not show any indications of phase modulation and possessed bell-shaped temporal and spatial intensity profiles, which can be well fitted by a Gaussian. Assuming that probe

pulses can be also approximated by the Gaussian and using Eq. (55) we obtain an expression for the width of the cross-correlation function:

$$\tau_{cross}^2 = \tau_{probe}^2 + \frac{1}{2}\tau_{pump}^2 , \tag{56}$$

which provides an estimate for the probe pulse duration τ_{probe}=53 fs (FWHM).
It should be mentioned that it was not easy to make both pump and probe pulses short at the position of the sample. First of all, ultrashort infrared pulses coming from Ti:Sa-laser are split into two pulses using a beamsplitter. These two pulses already have different durations since one of them experiences dispersive broadening upon transmission through a relatively thick beamsplitter ($\simeq$6 mm path in BK7-glass), whereas the other one remains unchanged upon reflection. Then both pulses are transmitted through further different refractive optical components such as $\lambda/2$ plates and lenses and, therefore, have different durations. However, the total amount of accumulated dispersion can be made equal for both pulses simply by putting an additional glass plate of appropriate thickness in the appropriate beam path. This well-known trick is used, for example, to obtain white-light interferograms in a Michelson interferometer. The dominant contribution to dispersion is due to the so-called second-order dispersion, which is often referred to as a *chirp* (linearly time-dependent optical carrier frequency within the pulse). A positive chirp accumulated in the refractive components of the experimental setup can be *compensated* by providing the initial laser pulses with a negative chirp through varying the distance between the two gratings of the compressor in the Ti:Sa-laser.
Without an additional glass plate the minimal width of the cross-correlation function, obtained after compressor optimization was around 150 fs. With an additional 7 mm-thick BK7-glass plate put into (an infrared) probe path before second harmonic generation, the width of a cross-correlation function is reduced to 60 fs. This arrangement corresponds to the minimal duration of the pump at the position of the sample and of the (infrared) probe at the position of the frequency-doubling crystal (110 μm-thin LBO-crystal), which corresponds to the maximum efficiency of second harmonic generation. Frequency-doubled probe pulses do not pass through any refractive optical components before entering the sample.

4.5 Interferometric measurements in fused silica

We started our interferometric measurements with optically polished glass samples (BK7, fused silica and high-purity fused silica). The thickness of the samples equal to 100 μm was chosen to be as small as possible in order to minimize the propagation

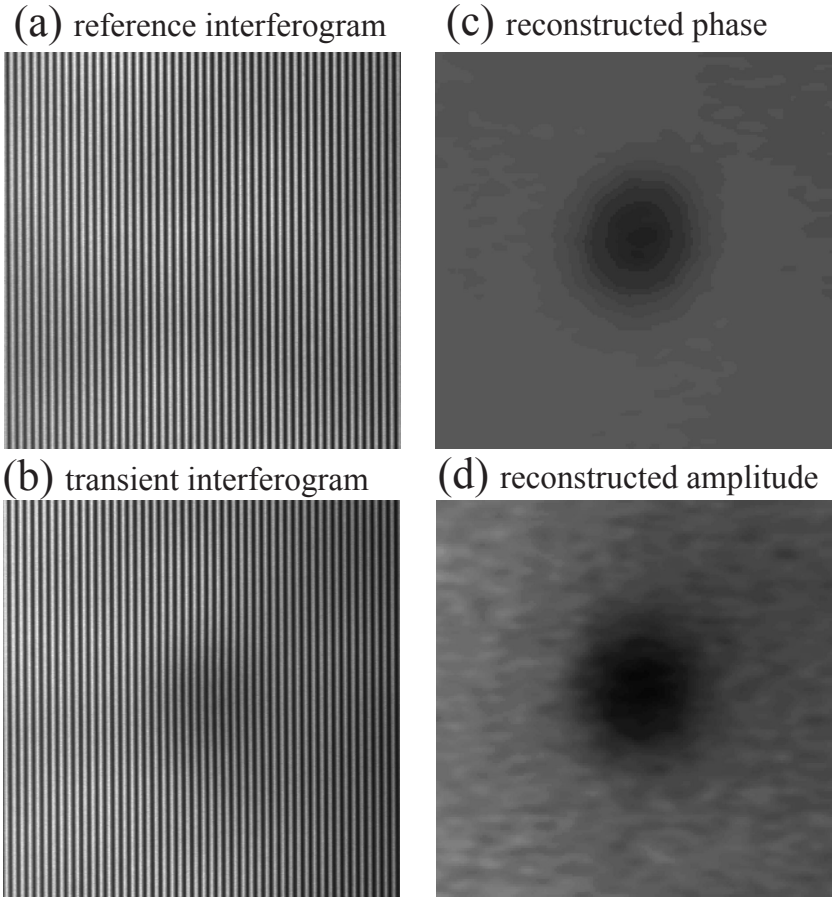

Figure 43: Example of interferometric measurements in fused silica: (a) reference interferogram, (b) transient interferogram, pump-probe delay time Δt=150 fs, (c) reconstructed phase, (d) reconstructed amplitude. Peak pump intensity was 10 TW/cm^2.

effects due to self-focusing, diffraction and temporal broadening of the pulses due to dispersion. The influence of self-phase modulation at high pump intensities was controlled by comparison of the spectra of pump pulses after propagation through the sample with the reference spectra without the sample. A strong self-phase modulation leads to spectral broadening of the pulses [70], which we have clearly seen in much thicker fused silica samples (L=500 μm).

We were not able to observe free carriers in ordinary optical glasses like BK7 and fused silica. A possible explanation is that the lifetime of free carriers is extremely short due to the high density of the defect states. Recently reported results on time-resolved broad-band optical absorption spectroscopy in fs-laser-excited BK7 and fused silica suggest that in these materials free carriers possess an extremely short life time below 100 fs [106]. For this reason we have performed further experiments

using a special type of high-purity fused silica (Schott Lithotec fused silica Q1-E193) with an extremely low bulk defect level around 0.1 ppm. Given the total concentration of silicon and oxygen atoms in fused silica of about 6.6×10^{22} cm^{-3} (mass density is 2.2 g/cm^3) we estimate an extremely small concentration of defects below 10^{16} cm^{-3}. Note that previously reported experiments starting with [9] were also performed using high-purity amorphous and crystalline quartz samples.

The results to be discussed first were obtained in the very beginning using slightly longer pump and probe pulses with duration of about 70-80 fs (width of cross-correlation function 90 fs), since not all tricks described in the previous section have been used to improve temporal resolution. An example of interferometric measurement in (high-purity) fused silica is presented in Fig. 43. The reference interferogram (Fig. 43(a)) was produced with a blocked pump beam while the transient interferogram (Fig. 43(b)) was taken 150 fs after excitation by a pump pulse with peak intensity of 10 TW/cm^2. The difference between the reference and transient interferograms is quite apparent. Laser-induced changes in the phase (Fig. 43(c)) and amplitude (Fig. 43(d)) of interference fringes were reconstructed by the 2D-Fourier-transform algorithm in the same way as described in Chapter 2.

A series of interferograms was recorded and processed for different pump-probe delay times. The results of such measurements are presented in Fig. 44, where the phase shift and normalized transmission of the probe pulse relative to the unexcited sample are plotted as a function of pump-probe delay time. The peak pump intensity in the center of the laser excited area was about 20 TW/cm^2.

For small delay times corresponding to the temporal overlap between the pump and probe pulses a positive phase shift was observed, which can be explained by cross-phase modulation due to the optical Kerr-effect. For positive delay times, after the pump pulse has gone, there remains a negative phase shift due to the generation of free carriers. The simultaneous decrease of probe transmission can be explained by free-carrier absorption. The identical relaxation time for phase shift and transmission indicates a very short lifetime of free carriers of about 150 fs, whereas at longer delay times the normalized transmission recovers almost to unity but phase shift becomes slightly positive. These qualitative observations are in excellent agreement with previously reported results [9, 103]. The temporal dependence of the phase shift is essentially identical to that shown in a subplot of Fig. 39(b), obtained by spectral interferometry. Particular attention should be paid to the explanation of a positive phase shift and small residual absorption at large pump-probe delay times existing for more than a few hundred picoseconds. When mobile free electrons are

cooled down via electron-phonon interaction the self-trapped excitons can be created, which provide a positive contribution to the refractive index and exhibit small absorption [102].

It is also possible to extract quantitative information about the parameters of the Drude-model from the interferometric measurements. Before doing that we want to discuss in detail the conditions under which the reconstructed phase shifts and amplitude changes of interference fringes can be interpreted as the actual laser-induced amplitude (transmission) changes and phase shifts of the probe pulses.

The basic assumption underlying the processing of interferograms is that a laser-induced phase shift does not change significantly on a time scale given by the duration of the probe pulse. While the changes of a time-dependent phase shift $\Delta\phi(t)$ during the width of the probe pulse are small compared to π, the processing algorithm supplies, as expected, the time-averaged phase shift $\langle\Delta\phi(t)\rangle$ and time-averaged transmission. In the opposite case of big phase modulation of the phase during the probe pulse strong artifacts can be obtained. The most remarkable effect in this case is the reduction of the fringe contrast, which has nothing to do with actual changes of transmission. The simple analysis of synthetic interferograms generated by the interference of a phase-modulated probe pulse due to cross-phase modulation induced by the pump with a non phase-modulated reference pulse suggests that besides the artificial contrast reduction, the reconstructed phase exhibits an extremely fast temporal variation on an unphysically short time-scale, which is shorter than the duration of the probe pulse.

Both artifacts can be recognized in the experimental data in Fig. 44. Apart from an extremely fast drop of the phase after the pump pulse, the reconstructed transmission drops almost to zero during excitation. The observed positive phase shift due to cross-phase modulation in Fig. 44 approximately equals 2π suggesting that the drop in transmission is an artifact. We have measured the actual transmission of probe pulses in the same setup under the same excitation conditions with a blocked reference arm of the interferometer. In this case the technique is reduced to the conventional time-resolved transmission microscopy. This direct measurement, not presented here, does not show a dramatic decrease in probe transmission around zero delay time, when both pulses overlap in time. However, approximately 100 fs after excitation the reconstructed and directly measured transmissions become equal. Starting from this point the results of interferometric measurements can be assigned to the transient absorption and phase shift of the probe pulses.

As already mentioned above, the background for qualitative interpretation of in-

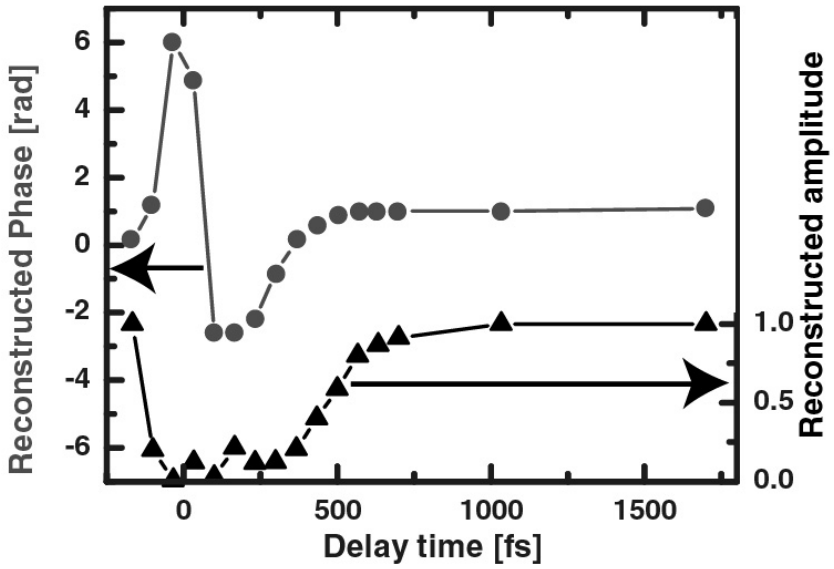

Figure 44: Interferometrically measured phase shifts (circles) and amplitude changes (triangles) versus pump-probe delay time in fused silica, I=20 TW/cm^2.

terferometric measurements is provided by the Drude-model. Assuming spatially homogeneous excitation of the sample along the propagation direction we can express the interferometrically measured phase shift $\Delta\phi$ and normalized transmission T of the probe pulses in terms of the real and imaginary part of the complex refractive index $\tilde{n}$:

$$\Delta\phi = \frac{2\pi}{\lambda} L \cdot \mathrm{Re}\{\Delta\tilde{n}\}\,, \tag{57}$$

$$T = \exp\Big(-\frac{4\pi}{\lambda} L \cdot \mathrm{Im}\{\Delta\tilde{n}\}\Big)\,, \tag{58}$$

where $L = 100$ μm is sample thickness and $\lambda = 0.4$ μm is probe wavelength. The Drude-model described by Eq. (54) gives:

$$\Delta n = \mathrm{Re}\{\Delta\tilde{n}\} = -\frac{e^2}{2n_0\varepsilon_0\omega^2 m_e} \cdot \frac{(\omega\tau_c)^2}{1+(\omega\tau_c)^2} \cdot \Big(\frac{\rho}{m^*}\Big) \sim \Delta\phi\,, \tag{59}$$

$$\Delta k = \mathrm{Im}\{\Delta\tilde{n}\} = \frac{e^2}{2n_0\varepsilon_0\omega^2 m_e} \cdot \frac{\omega\tau_c}{1+(\omega\tau_c)^2} \cdot \Big(\frac{\rho}{m^*}\Big) \sim \ln\{T\}\,. \tag{60}$$

In principle the probe beam does also experience additional phase shifts $\pm\Delta k/(n_0+1)$ (in rad) at both air-dielectric interfaces due to the change of optical absorption, which cancel each other out in the case of homogeneous excitation. Since the actual changes of the optical constants appear to be rather small these shifts can be disregarded in Eq. (57). Starting from this point it is more convenient to use a dimensionless effective mass $m^* \Rightarrow m^* m_e$, which is utilized in Eq. (59,60). It is clear

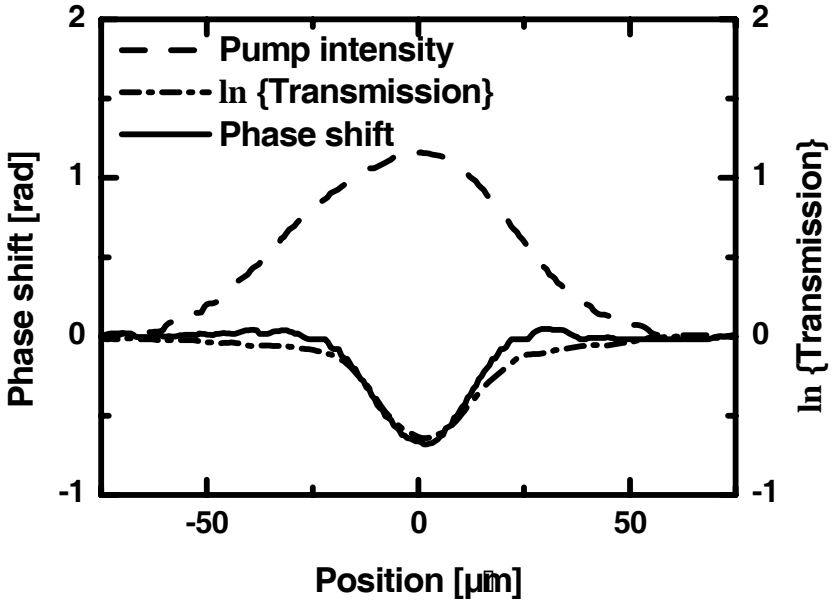

Figure 45: Spatial profiles of the phase (solid) and logarithm of transmission (dash-dot) of probe pulses obtained from Fig. 43(c) and 43(c); spatial intensity distribution of the pump pulse (dashed); fused silica, Δt=150 fs.

that three unknown parameters of the Drude-model, collision time τ_c, free-carrier density ρ and the reduced effective mass m^* cannot be uniquely determined from two measured quantities. However, it is possible to determine to the collision time τ_c and the ratio ρ/m^*, which has the dimensionality of electron concentration.
Figure 45 shows spatial profiles of the phase shift and the logarithm of transmission of pump pulses obtained from Fig. 43, together with the spatial intensity distribution of the pump pulse. Intensity distribution was directly measured by a CCD-camera. Peak intensity in the center of the laser-excited area was around 10 TW/cm^2, where a negative phase shift and decrease in the transmission of probe pulses induced by free-carriers are observed. The phase shift (in rad) is equal to the logarithm of transmission (see Fig. 45). It is possible to directly determine the collision time using equations (57-60):

$$\omega\tau_c = -\frac{\Delta n}{\Delta k} = \frac{2\Delta\phi}{\ln\{T\}} \simeq 2 \Rightarrow \tau_c \simeq 0.4 \text{ fs}\,. \tag{61}$$

The experimentally determined collision time appears to be very short, probably at the applicability limit of the Drude-model. Since fused silica is a disordered material it is reasonable to assume that the dominant scattering mechanism is electron scattering by disordered atomic potentials [51]. Two types of electronic states exist in a disordered material: (i) delocalized states, which are analogous to Bloch-waves in crystals at least considering optical absorption and (ii) localized states describing

electrons "trapped" by an ion (Anderson localization [51]), which practically do not contribute to optical absorption. Between the two successive collisions the electrons, if they are free, are characterized by mean *group velocity* $\langle v \rangle$ and should cover at least one interatomic distance d:

$$\tau_c > \tau_{Joffe} = \frac{d}{\langle v \rangle} . \tag{62}$$

This condition known as the Joffe-Regel limit sets the borderline between the high free-carrier conductivity and low "hopping" conductivity when the electrons spending most of the time in a localized state occasionally "jump" to the neighboring ion driven by thermal fluctuations or some external perturbation [51]. A drastic decrease of carrier mobility in case of hopping conductivity is usually characterized by the so-called mobility edge.

For typical values of parameters: average interatomic distance in fused silica of 0.25 nm, mean kinetic energy of the electrons $0.5 m_e \langle v \rangle^2$ ~1 eV (m^*=1) we obtain a rough estimate $\tau_{Joffe} \simeq 0.4$ fs, which is identical to the experimentally measured collision time (61). At first glance the applicability of the Drude-model becomes questionable. However, reliable quantitative experimental [109, 110] and theoretical [107, 108] studies exist on charge transport and "band"-structure in fused silica. Low-field mobility of the electrons in a DC-electic field at room temperature $\mu_e = 20$ cm^2/V is measured [109], which is much bigger than that of the holes $\mu_h \sim 10^{-5}$ cm^2/V [110]. The value of electron mobility appears to be much bigger than for other disordered materials [109]. This experimental observation is fully consistent with the results of microscopic "band"-structure calculations, which predict the *absence of localized states* near the conduction band edge. Localized states are found to exist in the vicinity of the valence band forming the mobility edge for the holes (with a width ~0.2 eV). Since there are almost no localized states in the conduction band, the "free" electrons possess a high mobility and dominate the carrier transport. Most likely, the actual electron energies exceed 1 eV since for small collision times, which are much shorter than pump pulse duration, electrons generated during the pulse can efficiently absorb photons ($\hbar\omega$=1.55 eV) by free-carrier absorption. The results of theoretical modeling of high-field (F>10 MV/cm) carrier-transport in crystalline silicon dioxide at room temperature predict extremely short momentum relaxation times (~0.1 fs) and energy relaxation times (~100 fs) for the conduction band electrons with energies of several eV scattered on both optical and acoustical phonons [93, 111]. Some important discussion about the physical interpretation of such short relaxation times, the concept of "collisional broadening"

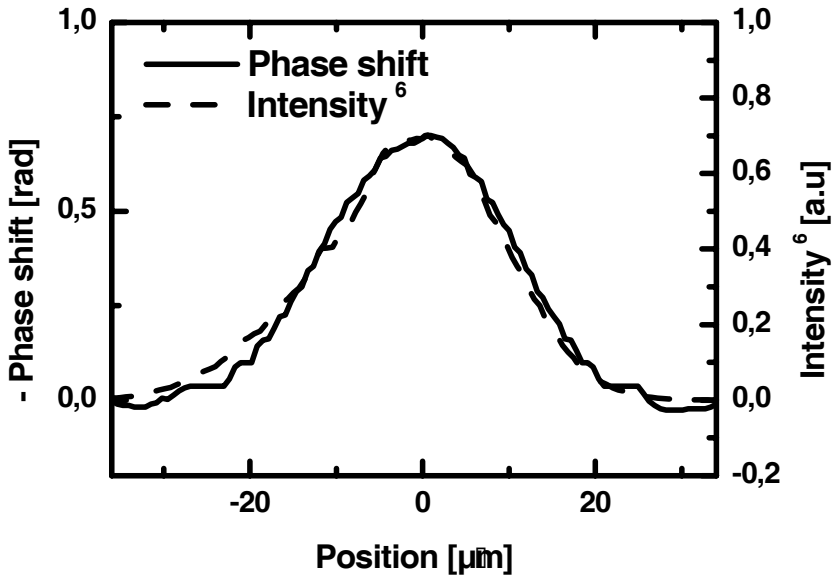

Figure 46: Spatial profiles of the phase (solid) the sixth power of pump intensity I^6 (dashed) of Fig. 45; fused silica, Δt=150 fs.

for electronic states, and the essential problem of the applicability of the developed model in case of an amorphous silicon dioxide (fused silica) is given in [93].

The above arguments strongly suggest that the Drude-model is applicable in our case and the measured value of momentum relaxation time $\tau_c = 0.4$ fs is reasonable. Since we are talking about relatively high temperatures and small electron concentrations below 10^{20} cm^{-3} (to be shown further), band-filling effects can be neglected and the electrons are distributed according to the Maxwell-Boltzmann law whereas thermal velocities are large compared to the Fermi-velocity.

Free carrier density or, more precisely, the ratio ρ/m^* in the center of the laser-excited area in Fig. 45 is around 10^{19} cm^{-3}. For such low electron concentrations we can assume that both the effective mass and collision time do not depend on pump intensity. This assumption is supported by a relatively good coincidence of the two spatial profiles in Fig. 45, because in this case both changes in phase and transmission (ln T) must be proportional to free-carrier concentration.

Figure 46 aims to demonstrate that the spatial phase profile coincides with the sixth power of the pump intensity: $\rho \sim I^6$, which represents a clear signature of 6-photon ionization. A sharp optical absorption edge in fused silica is around 9 eV: imaginary part k of the linear complex refractive index changes by *four orders of magnitude* for photon energies between 7.75 eV=5 $\hbar\omega$ ($k < 4.7\times10^{-6}$) and 9.3 eV=6 $\hbar\omega$ ($k = 0.034$) [112]. Therefore the expected minimal number of infrared photons needed to cross the optical absorption edge is indeed equal to 6.

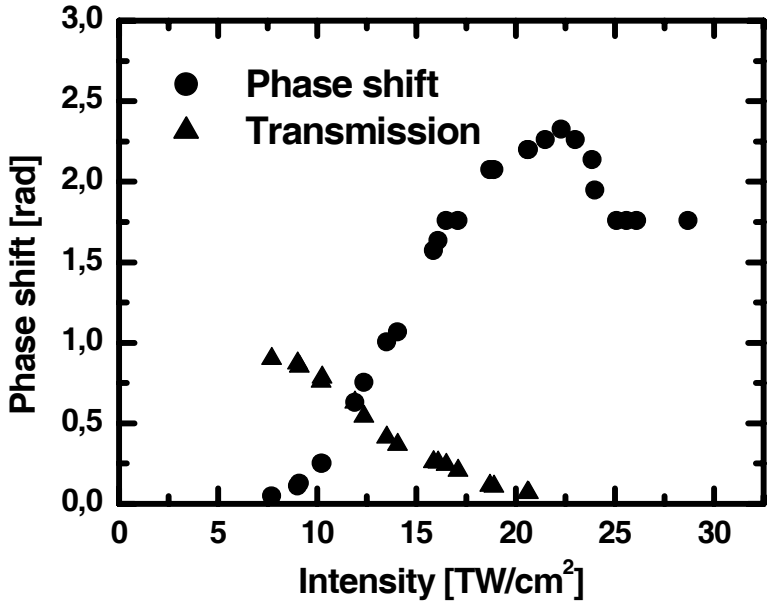

Figure 47: Dependence of phase shift (circles) and transmission (triangles) of the probe pulse on peak pump intensity; fused silica, Δt=150 fs.

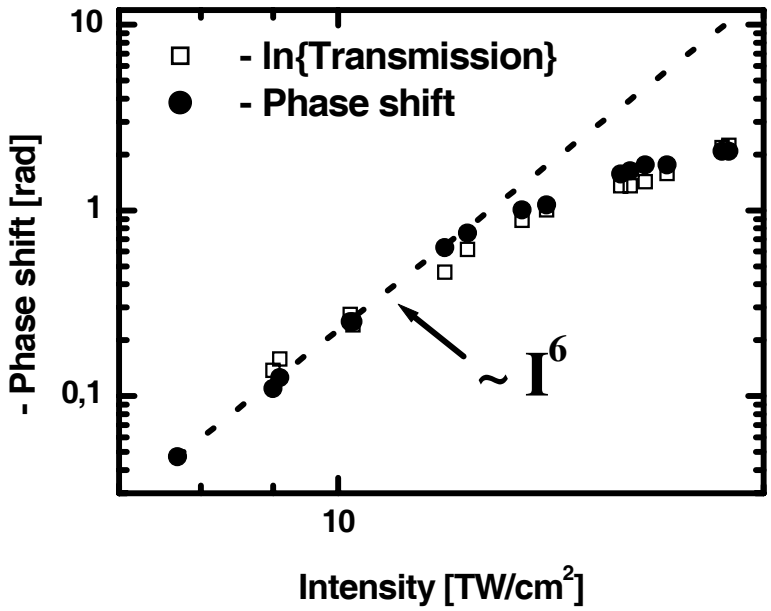

Figure 48: Intensity dependence of phase shift (circles) and the logarithm of transmission (squares) of Fig. 47, plotted on a double-logarithmic scale; fused silica, Δt=150 fs.

In order to verify the conclusion that 6-photon ionization is a dominant ionization mechanism, we have measured the dependence of free-carrier density on peak pump intensity by varying the energy of the pump pulses. The result of this measurement is presented in Fig. 47: with increasing intensity the modulus of the phase shift increases up to intensities of about 25 TW/cm^2 whereas the transmission decreases, indicative for the growth of the electron concentration. In figure 48 the dependencies of Fig. 47 for low intensities are plotted on a double-logarithmic scale. The fitting of the experimentally measured phase dependence for low intensities by a potential law $\rho \sim I^{\alpha}$ provides the value of $\alpha = 5.96$. The logarithm of transmission shows similar behavior. Thus the 6-multiphoton ionization mechanism is again confirmed by this measurement.

For higher pump intensities we observe some deviations from multiphoton law $\rho \sim I^6$. The conspicuous decrease of the phase shift and drastic decrease of transmission in the intensity range around 30 TW/cm^2, at which surface breakdown in dielectrics is expected, is quite apparent in Fig. 47. After finishing the optimization of the temporal resolution of the setup, we conducted additional interferometric measurements in fused silica with 50 fs-short linearly and circularly polarized pump pulses. Circularly polarized pulses were obtained by using an additional thin $\lambda/4$-plate positioned in front of the focusing lens. A rotation of a $\lambda/4$-plate by 45 degrees allows one to switch between the two polarization states without changing anything else. We have performed comparative energy calibrations and direct measurements of the actual polarization state with the help of a rotatable polarizer and a photodiode. The transmission of a perfect circularly polarized wave through a polarizer does not depend on its orientation. When rotating the polarizer we observed weak variations in the transmitted signal with $(I_{max} - I_{min})/(I_{max} + I_{min}) < 0.2$, which corresponds to the superposition of orthogonally polarized $\lambda/4$-phase-shifted plane waves with electric field amplitudes equal within 10%.

The results of interferometric measurements for two polarizations of the pump pulses are presented in Fig. 49. The 6-photon ionization represents the dominant ionization mechanism for both polarizations at low intensities around 10-15 TW/cm^2. For circular polarization the ionization rate is approximately 3 times smaller than for the linear one, whereas the collision time is somewhat bigger: $\tau_c \simeq 0.8$ fs at the lowest intensity.

For higher intensities (i) phase shift precisely coincides with the logarithm of transmission for each polarization and (ii) the curves for both polarizations come close together and their slope on a double-logarithmic scale becomes smaller, showing a

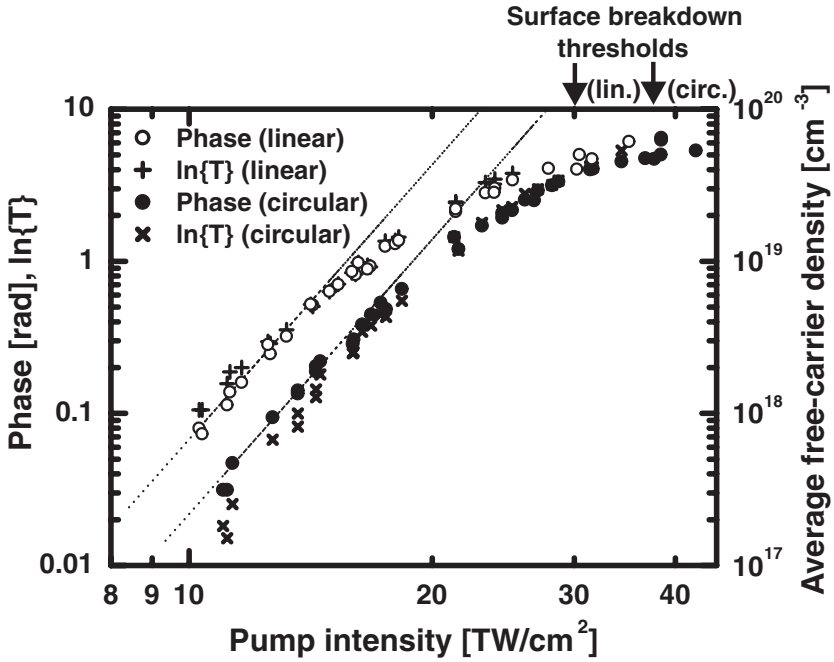

Figure 49: Intensity dependence of phase shift and the logarithm of transmission for linear and circular polarizations; fused silica, Δt=150 fs. The arrows in the upper right corner denote the intensities at which surface breakdown threshold takes place.

pronounced deviation from multiphoton law.

For high intensities around 30 TW/cm^2 the slope of the curves becomes close to zero. We were able to precisely determine the surface breakdown threshold from the interferometric measurements in a similar way as for femtosecond laser ablation of absorbing solids. Surface breakdown in dielectrics does also lead to the formation of well-defined ablation craters, a few tens of nanometers deep. This leads to pronounced phase shifts in *final* interferograms proportional to the crater depth times refractive index difference between air and dielectric $(n_0 - 1)$. From the analysis of final ablation craters the surface breakdown threshold is found to occur at laser intensities of I_{thr}^{lin}=30 TW/cm^2 for linear and I_{thr}^{circ}=37 TW/cm^2 for circular polarizations. The accuracy of the absolute values is around $\pm$ 20%, which accounts for errors in the determination of the absolute values for pulse energy, pulse duration and beam diameter. However, since these calibration errors are identical for two pump polarizations, the ratio of breakdown thresholds as well as the ratio of ionization rates is known precisely. A bigger ionization rate leads to a smaller breakdown threshold.

The nature of conspicuous deviations from multiphoton ionization law at higher intensities remains to be clarified. As suggested in [103], this could be an artifact

due to a *strongly inhomogeneous* excitation in longitudinal direction. Then the simplified formula (59,60) must be replaced by the following expressions

$$\langle \Delta n \rangle = -\frac{e^2}{2n_0\varepsilon_0\omega^2 m_e} \cdot \frac{(\omega\tau_c)^2}{1+(\omega\tau_c)^2} \cdot \frac{1}{L}\int_0^L \frac{\rho(z)dz}{m^*}\,, \tag{63}$$

$$\langle \Delta k \rangle = \frac{e^2}{2n_0\varepsilon_0\omega^2 m_e} \cdot \frac{\omega\tau_c}{1+(\omega\tau_c)^2} \cdot \frac{1}{L}\int_0^L \frac{\rho(z)dz}{m^*}\,, \tag{64}$$

where a probably strong spatial dependence $\rho(z)$ on the longitudinal coordinate z is averaged out by integrating over the whole sample thickness L. The use of expressions (63,64) is justified for a smooth carrier-density profile on a spatial scale given by optical wavelength (WKB-approximation).

In order to realize the relevance of spatial averaging effect we have mentioned, we have performed simple model calculations for a 1D-pulse propagation through the sample using the following set of coupled differential equations:

$$\frac{\partial\rho(z,t)}{\partial t} = \sigma_6 I^6\,, \tag{65}$$

$$\frac{\partial I(z,t)}{\partial z} = -6\hbar\omega\sigma_6 I^6 - \alpha(\rho) I\,. \tag{66}$$

These take into account 6-photon absorption described by its cross-section σ_6 and free-carrier absorption with $\alpha(\rho) = (4\pi/\lambda)\Delta k(\rho)$, where $\Delta k(\rho)$ is given by Eq. (60). Since a small fraction of the incident pulse $I_{inc}(t)$ is reflected from the front surface of the sample, the actual input pulse reads $I(0,t) = I_{inc}(t)[1-R(t)]$, where the reflection coefficient $R(t)$ is calculated using the Fresnel-formula with time-dependent optical constants at the surface due to free carrier generation. For free-carrier density at the surface below the critical density the changes in $R(t)$ are negligibly small. Equation (66) is valid if the induced spatial gradients of the refractive index are small: $\partial n(z,t)/\partial z \ll 1/\lambda$, which allows us to neglect the back-scattered wave. In case of strong refractive index gradients, i.e. for pump intensities close to the surface breakdown threshold, wave-equation must be solved. A fundamental issue concerning the applicability limits of simplified propagation equations derived from Maxwell's equations is discussed by Brabec and Krausz [99].

A few examples of simple modeling utilizing equations (65,66) are presented in Fig. 50 for three different pump intensities of incident pump pulses (10, 20 and 30 TW/cm^2) and the following set of parameters: $n_0 = 1.45$, $m^* = 1$, $\sigma_6 = 7.5\times10^{-47}$ [s1cm^9/W^6], τ_c=0.4 fs, τ=50 fs (FWHM). The incident pulse propagates from the left to the right through a 100 μm-thin sample and generates free carriers by 6-photon ionization. As the pulse propagates its peak intensity decreases due

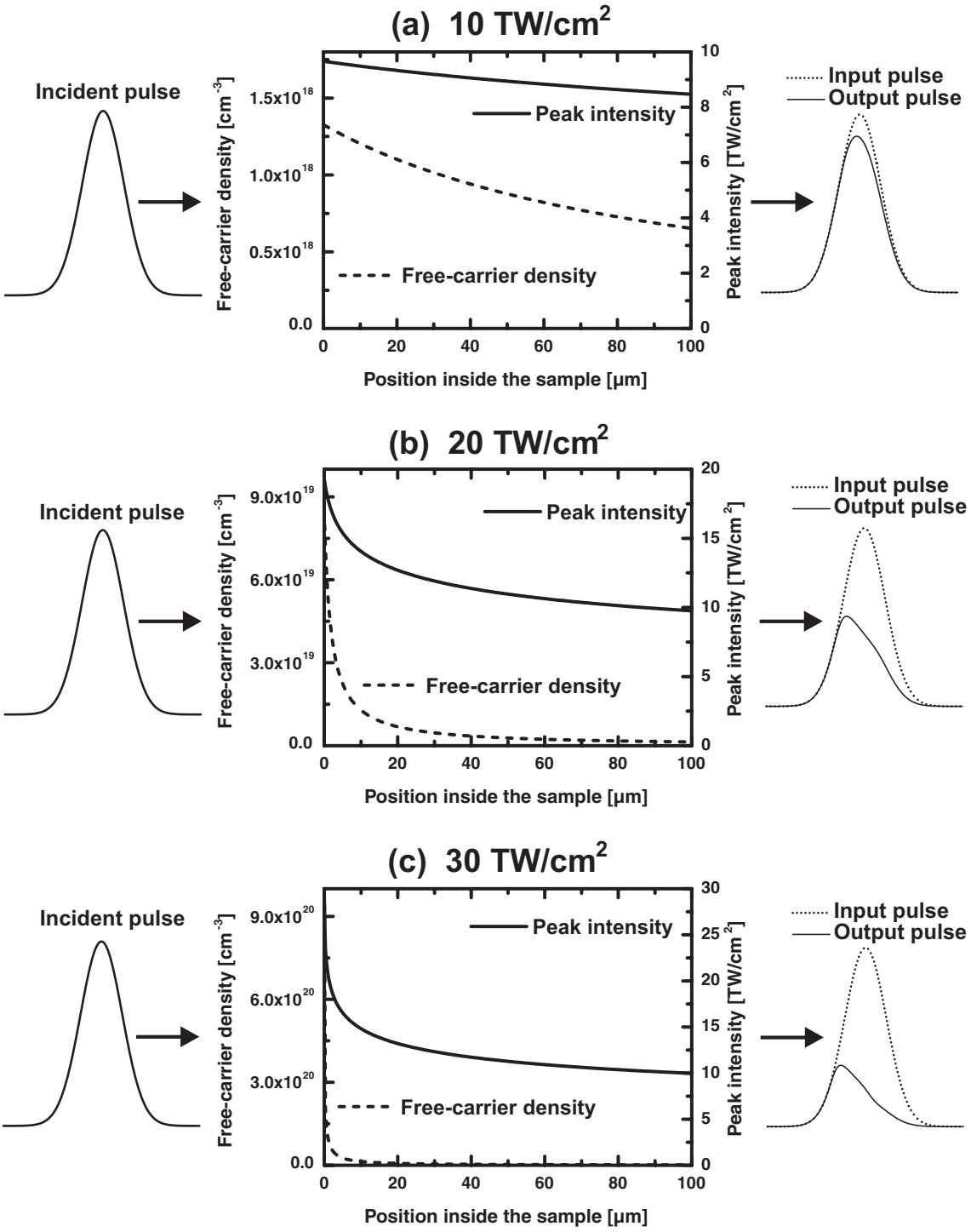

Figure 50: Results of model calculations of 1D-pump pulse propagation through a dielectric medium (see text for details) for three different pump intensities: 10, 20 and 30 TW/cm^2. Pump pulses normally incident on the sample (on the left), profiles of free-carrier distribution and peak intensity inside the sample (in the center), temporal shape of output pulses as compared to the input pulses (on the right). Parameters of the model: $n_0 = 1.45$, $m^* = 1$, $\sigma_6 = 7.5 \times 10^{-47}$ [s^{-1}cm^9/W^6], τ_c=0.4 fs, τ=50 fs (FWHM).

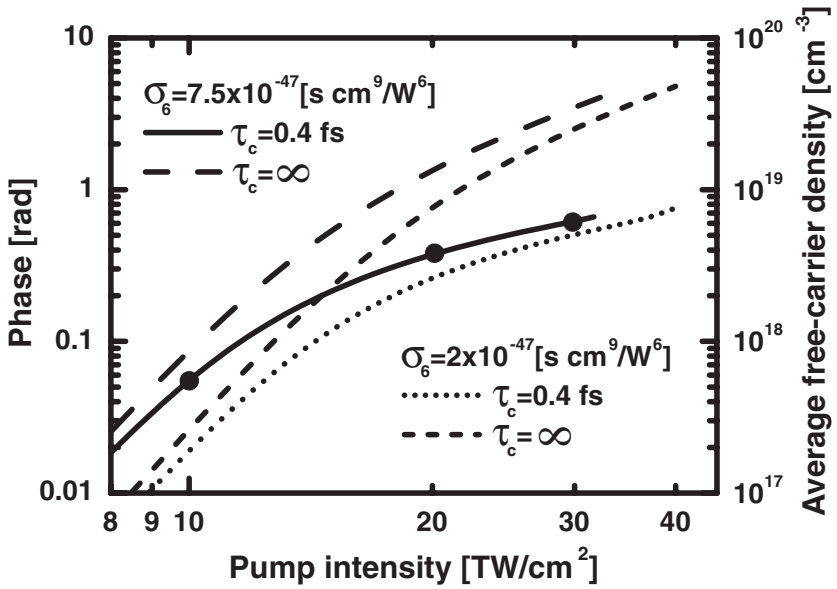

Figure 51: Simulated intensity dependence of spatially averaged free-carrier density for two different crossections of 6-photon-ionization, $\sigma_6 = 2 \times 10^{-47}$ and 7.5×10^{-47} [$s^{-1}cm^9/W^6$], and two different collision times τ_c=0.4 fs and ∞ (no collisions). Other parameters are the same as in Fig. 50, whereas the 3 bold black points on the solid curve correspond to 3 examples in Fig. 50.

to 6-photon absorption and free-carrier absorption. Spatial profiles of free-carrier distribution and peak pump intensity inside the sample are presented in the central part of Fig. 50. The temporal shape of transmitted pump pulses (output pulses) is compared with that of the input pulses on the right side of Fig. 50. For the peak intensity of 10 TW/cm^2 the pump pulses experience minor absorption and do not show any significant changes in their shape after propagation through the sample. The relatively low density of free-carriers at the surface about 10^{18} cm^{-3} decreases only by 40% within the sample and, therefore, the excitation is quite homogeneous. For 20 TW/cm^2 the situation changes dramatically: the peak intensity decreases to 10 TW/cm^2 at the rare side of the sample and output pulses are strongly distorted. A high free-carrier density of about 10^{20} cm^{-3} is reached at the front surface, which drastically decreases within the first few microns and reaches the value of about 10^{18} cm^{-3} at the rare side of the sample. For 30 TW/cm^2 surface free-carrier concentration 10^{21} cm^{-3}, which is slightly below the critical density, 3.5×10^{21} cm^{-3}, drops by an order of magnitude within only 1 μm. In this intensity range high spatial gradients of the refractive index are apparent and, therefore, our simple model described by Eq. (65,66) is likely to fail.

To connect the results of this simple modeling with the experimental data presented

in Fig. 49 we have calculated the phase shift of the probe pulses, which is proportional to spatially averaged free-carrier density, as a function of peak pump intensity. Figure 51 shows the results for two different cross-sections of 6-photon-ionization, $\sigma_6 = 2 \times 10^{-47}$ and 7.5×10^{-47} [$s^{-1}cm^9/W^6$], and two different Drude-collision times τ_c=0.4 fs and ∞ (no collisions), whereas other parameters are the same as in the last paragraph. The three bold black points on a solid curve in Fig. 51 correspond to the examples presented in Fig. 50.

The two different values for the cross-sections of 6-photon ionization fit the experimental data for linearly and circularly polarized pump pulses at low intensities. The comparison of the situation in which frequent collisions occur, τ_c=0.4 fs, with a collisionless case provides an illustration of how strongly the results depend on the particular choice of parameters. It is quite apparent from Fig. 51 that independent of the collision time the two curves with different cross-sections of multiphoton ionization come close together for high intensities, whereas their slopes decrease. Thus the characteristic features of the experimentally measured dependencies of Fig. 49 can be explained by the effects of the spatial averaging of highly inhomogeneous free-carrier distribution in the propagation direction, without any deviations from the multiphoton ionization mechanism.

The curves for equal 6-photon cross-sections with different collision times in Fig. 51 coincide for small intensities. The small difference between them is mainly due to different factors $\omega^2\tau_c^2/(1+\omega^2\tau_c^2)$ in Eq. (63), but not due to different free-carrier concentrations. For higher intensities average electron density is significantly higher in the collisionless case because pump pulse absorption by free-carriers is absent. At first glance, from a comparison of phase shifts at high intensities, the curves for the collisionless case seem to be in a better agreement with the experimental data. However, the collision time of 0.4 fs gives $\omega_{pump}\tau_c = 1$, which corresponds to the maximum of free-carrier absorption. We believe that this collision time measured 100 fs after the pump pulse can strongly differ from that present during the pulse, since during the pump pulse a highly non-equilibrium free-carrier distribution can be generated by free-carrier absorption implying the existence of extremely short-living hot carriers [67] with momentum and energy relaxation times down to 0.1 fs and 100 fs, respectively [111]. If we set a shorter collision time in our model calculations, $\tau_c < 0.4$ fs, the average electron concentration for high intensities becomes bigger due to the diminishing contribution of free-carrier absorption.

It is very surprising, but given the experimentally measured cross-sections and assuming that the 6-photon ionization is the dominant ionization mechanism for all

intensities, the surface electron density reaches the critical density at intensities which are very close to experimentally determined threshold intensities for surface breakdown, for both linearly and circularly polarized pump pulses.

The above interpretation is purely qualitative; the multi-parameter fit to experimentally measured curves does not make sense since, for example, not only the collision time but also the effective mass depends on the energy distribution function of free carriers [82]. The possibility discussed to explain the experimental results for high intensities purely by spatial averaging effects and the surprising coincidence of breakdown thresholds assuming the multiphoton ionization does not, of course, rule out the possibility that avalanche or tunneling ionization contribute to free-carrier generation at high intensities. Moreover, we were able to observe a small transverse spatial narrowing of the transmitted pump pulses for high intensities, indicating the onset of self-focusing, which could also effect the results of experimental measurements.

The interferometric measurements presented do not in principle allow us to learn something about the actual ionization mechanisms at high intensities because of the variety of unknown parameters. In contrast, for small intensities and small free-carrier densities, at which both spatial averaging effects and free-carrier absorption are negligible, the deduced cross-sections of 6-photon-ionization $\sigma_6^{lin} = 7.5 \times 10^{-47\pm0.5}$ [$s^{-1}cm^9/W^6$] for linear and $\sigma_6^{circ} = 2 \times 10^{-47\pm0.5}$ [$s^{-1}cm^9/W^6$] for circular polarizations can be considered as relatively accurate quantitative results. The error factor $10^{\pm0.5}$ results from the 20%-uncertainty in experimental intensity determination, but the assumption about free-carrier effective mass $m^* = 1$ should also be kept in mind. Previously reported estimations for a 6-photon absorption cross-section vary over many orders of magnitude [81]: $\sigma_6^{lin} = 3 \times 10^{-49} \div 6 \times 10^{-45}$ [$s^{-1}cm^9/W^6$], all of them being the results of a multiparameteric fit to experimental data obtained from the post-mortem analysis of laser-induced damage. Our experimentally determined cross-sections fall within this broad range of estimations and the error factor $10^{\pm0.5}$ appears to be not that bad.

It is interesting to compare our results with the predictions of Keldysh's ionization theory. It can be deduced from Eq. (46) that for low intensities $\sigma_{n_{ph}} \sim (1/m^*)^{n_{ph}-1.5}$ with $n_{ph} = 6$ in our case. Assuming different values of m^* allows us to tune the ionization cross-section over many orders of magnitude. However, in order to obtain the experimentally determined value of $\sigma_6^{lin} = 7.5 \times 10^{-47}$ [$s^{-1}cm^9/W^6$] we need to substitute $m^* = 0.49$, which is a reasonable value. The value of the Kedlysh

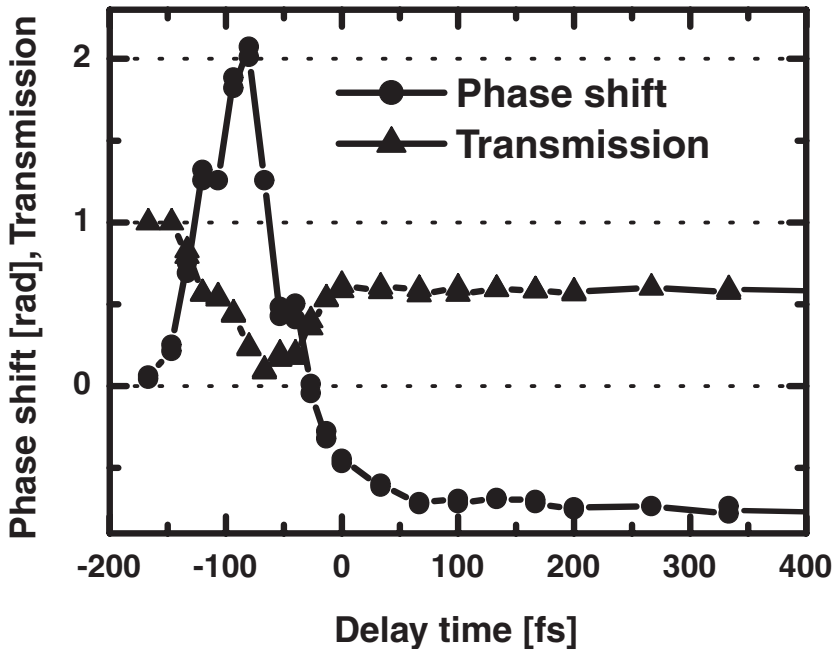

Figure 52: Interferometrically measured phase shifts (circles) and transmission changes (triangles) in sapphire versus pump-probe delay time, I=12 TW/cm^2.

parameter γ given by Eq. (45) is equal to

$$\gamma = \frac{\omega}{e}\sqrt{\frac{n_0\varepsilon_0 c m^* m_e \Delta}{2I}} \simeq 1.5 \tag{67}$$

for I=10 TW/cm^2, m*=0.5, $\Delta = 9$ eV, $\omega = 2.35 \times 10^{15}$ Hz ($\lambda = 800$ nm). We made use of Eq. (48), which relates the peak electric field F with intensity I of a linearly polarized wave. The estimated value of $\gamma \simeq 1.5$ is just at the applicability limit of multiphoton ionization, for which the condition $\gamma >> 1$ must be fulfilled. Thus Keldysh's theory predicts that the transition to tunneling ionization is the intensity range at which we have observed deviations from multiphoton law.
This purely qualitative comparison with Keldysh's model calculations should be considered very critically since their actual applicability limits, in particular in the case of disordered materials and frequent collisions, are unknown so far.

4.6 Interferometric measurements in sapphire

We have performed similar interferometric measurements with 100 μm-thin optically polished wafers of high-purity sapphire (Al_2O_3), which is an optically uniaxial ionic crystal with a hexagonal (rhombohedral) structure and direct band gap at $\Delta = 8.7$ eV [113]. For the first set of samples grown by the Verneuil method the crystallographic orientation was not defined by the manufacturer (Schott-Guinchard,

Switzerland). From the measurements of the optical anisotropy of the sample positioned between the two parallel or crossed polarizers at 3 different wavelengths (selected from a white-light source with interference filters) we have determined the angle of 31 degrees between the surface normal and the optical axis. The first run of the measurements was performed by exciting the sample with linearly polarized extraordinary pulses, for which the electric field oscillates in the same plane, in which the optical axis lies.

The typical dependence of phase shift and transmission change in the center of the laser-excited area (τ_{pump} = 50 fs, peak intensity 12 TW/cm^2) is presented in Fig. 52. A positive phase shift due to cross-phase modulation is followed by a negative phase shift due to free carriers at positive delays. Negative phase shift and reduced transmission remain unchanged for a couple of picoseconds and decay to initial values within roughly 100 ps. The observed behavior is fully consistent with previously reported results [103] (see also Fig. 39(b)). Figure 53 shows the temporal evolution of the collision time τ_c and ratio ρ/m^* just after the pump pulse. Within the first 200 fs after the pulse both quantities τ_c and ρ/m^* increase rapidly and reach their stationary values 0.65 fs and 1.4×10^{19} cm^{-3}, respectively . Note that the indications of this ultrafast dynamics can be seen in the decrease of the phase shift after the pump pulse in the data by Quere at al. (subplot in Fig. 39(b)), who have never discussed this effect. The observed fast dynamics is more pronounced for the stronger excitation of 20 TW/cm^2 shown in Fig. 54, whereas the stationary values are $\tau_c = 0.55$ fs and $\rho/m^* = 6.5 \times 10^{19}$ cm^{-3}.

Thus, both the collision time τ_c and the ratio ρ/m^* increase after the pulse, indicative on some ultrafast dynamics of free carriers in sapphire *just after* laser excitation. The observed collision times for sapphire are very short, in particular just after the pulse. This strongly suggests that hot electrons are present which could be generated during the laser pulse by free-carrier absorption. It is possible to associate the observed increase of the collision time with the relaxation of hot electrons to the bottom of the conduction band via electron-phonon scattering [93]. The predicted rate of electron-phonon scattering is about 10^{15} s^{-1} and increases as a function of electron energy [93]. Thornber and Feynman also report on very high relaxation rates of electron energy for hot electrons interacting with optical phonons in a polar crystal, which they have obtained from first-principle non-perturbative calculations utilizing the path-integral method [115].

At the same time the increase of the ratio ρ/m^* can be explained purely by the reduction of the effective mass as the electrons are cooled down, without any changes

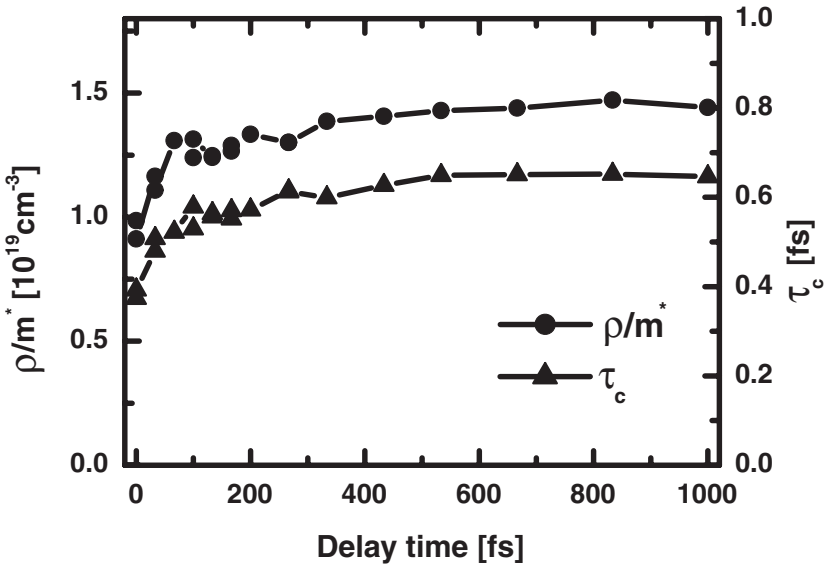

Figure 53: Temporal evolution of the collision time τ_c and the ratio ρ/m^* just after the pump pulse, obtained from Fig. 52; sapphire, I=12 TW/cm^2.

of electron density. Indeed, the effective mass is found to be $m^* = 0.25$ for low-energy electrons in sapphire [117], whereas hot electrons are assumed to have an effective mass close to that of free electrons , $m^* = 1$ [93]. Note that the energy relaxation of hot electrons in fused silica occurs on the same time-scale: within 150 fs free carriers form self-trapped excitons, which is possible only with low-energy electrons [102].

However, there exists an alternative explanation for the observed ultrafast dynamics of free carriers after the pump pulse. It is predicted by numerical simulations [67] that long-living electrons with high kinetic energies exceeding the critical energy for the avalanche ionization could be generated during the pulse, which create additional low-energy conduction-band electrons via impact ionization after the pump pulse.

The presented experimental data aim to demonstrate that the optical properties of free-carriers in sapphire measured 100 fs after the pulse are different from those during the action of the pulse, which justifies the discussion in the previous section about time-dependent parameters of the Drude-model for fused silica.

As already mentioned above, the experimental data discussed were obtained for excitation with extraordinary pulses. We have performed similar interferometric measurements for excitation with ordinary pulses (electric field perpendicular to the optical axis) and obtained qualitatively the same results, implying ultrafast dynamics of the optical properties after excitation. However, the collision time appeared to be significantly larger.

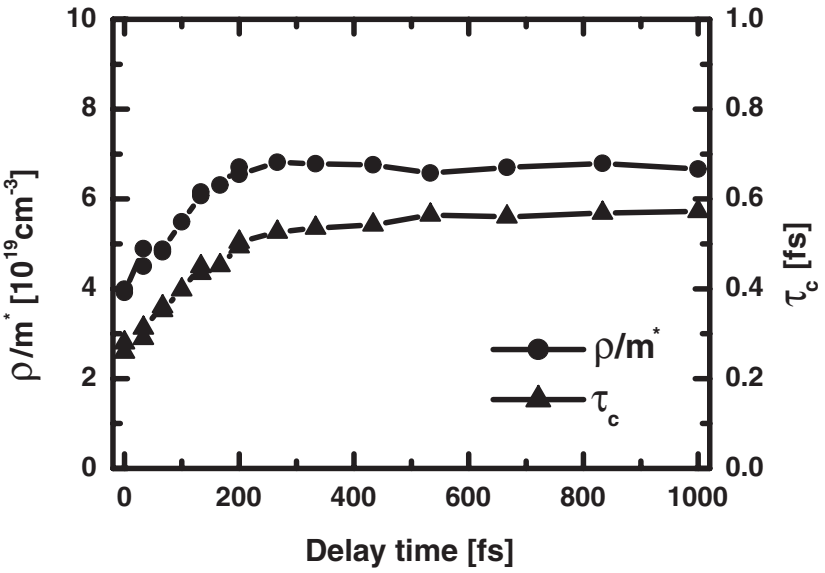

Figure 54: Temporal evolution of the collision time τ_c and the ratio ρ/m^* just after the pump pulse; sapphire, I=20 TW/cm^2.

In order to convince ourselves that the differences observed are due to the orientation of the sample, we have performed interferometric measurements for a fixed pump-probe delay time of 1 ps and constant pump intensity of 12 TW/cm^2 by rotating the sample around its normal (Fig. 55).

The static anisotropy signal in Fig. 55 represents the result of preliminary measurements to determine the sample orientation by means of HeNe-laser. The sapphire sample was placed between two crossed polarizers and rotated around the surface normal. The dashed line in Fig. 55 represents the intensity of a transmitted HeNe-laser beam as the sapphire sample is rotated around its normal. A linearly polarized incident electromagnetic wave can be decomposed into ordinary and extraordinary waves in a uniaxial crystal that are orthogonally polarized and possess different phase velocities. They experience different phase shifts and produce an elliptically polarized wave at the output of the crystal, which results into non-zero transmission through the second polarizer. However, if the angle between the plane of laser polarization and the plane formed by the optical axis of the crystal and the normal to the surface is either 0° or 90°, the polarization state of the electromagnetic wave does not change and transmission is zero. In this manner we were able to mark the angles at which the excitation of the crystal occurs as ordinary "*o*" or extraordinary "*e*" pump pulses.

It appears from Fig. 55 that the collision time τ_c correlates with the orientation of the sample: for the ordinary wave the collision time is larger than for the extraordinary.

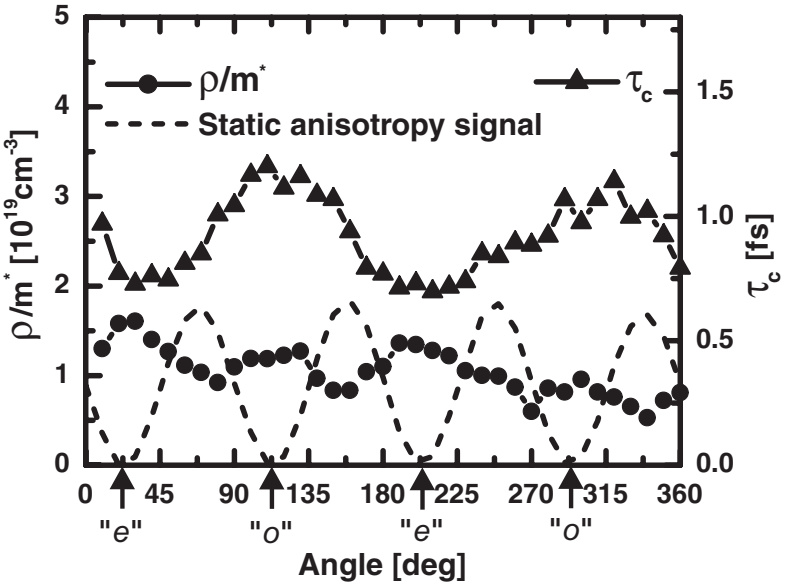

Figure 55: Dependence of the collision time τ_c and carrier density ρ/m^* on the orientation of a sapphire sample after excitation with a linearly polarized pump pulse, Δt=1 ps. The dashed curve represents the static anisotropy signal whereas the arrows indicate the excitation with ordinary "*o*" and extraordinary "*e*" pulse (see text for details).

This observation correlates with measurements of carrier mobility in sapphire excited by x-rays, which appears to be two times larger in the direction perpendicular to the optical axis than parallel to it [116].

The carrier density ρ/m^* exhibits local maxima for both the ordinary and extraordinary pulses and local minima between them (a linear decrease of ρ/m^* with an increasing angle is due to the slight decrease of the pulse energy determined by the long-term drift of the laser during this measurement). One could explain this unusual angular dependence of free-carrier density (4 minima and 4 maxima) by different ionization rates for linearly and circularly polarized pump pulses. Whereas for angles "*o*" and "*e*" the pump pulses remain linearly polarized propagating through the sample, for angles in between them the initially linear polarization state changes with propagation distance first to circular, then back to linear, then again to circular as in a normal optical wave-plate. Thus the 4 minima of the angular dependence of free-carrier density correspond to "mixed" excitation with both linearly and circularly polarized pump pulses due to the propagation-induced polarization change in a birefringent sapphire sample.

In order to investigate the influence of the polarization state of the pump pulses (ordinary versus extraordinary, but also linear versus circular) upon ionization rate

we have performed the second run of measurements in sapphire samples with different crystallographic orientations. The samples are 50 μm-thick high-purity sapphire wafers manufactured by the film-fed growth (EFG) method (CrysTec, Berlin) and are characterized by a low density of foreign atoms below 50 ppm.

In order to compare the ionization rates with linearly and circularly polarized pump pulses we have performed the interferometric measurements in thin sapphire (001) samples with the optical axis being perpendicular to the surface. Thus for both linearly and circularly polarized pump pulses the excitation of the crystal occurs with an ordinary wave. All remarks concerning the quality of the polarization state and energy calibration for the pump pulses are the same as described in the previous section for fused silica.

Figure 56 shows the dependence of the phase shift (average free-carrier density) and logarithm of transmission of probe pulses measured 1 ps after excitation with linearly and circularly polarized pump pulses on their intensity. The results appear to be similar to those for fused silica in Fig. 49. The solid curves denoted as "guide for the eye" in Fig. 56 represent polynomial fits for the corresponding dependencies of the phase. At low intensities the curves for both polarizations scale as $\sim I^6$ (dotted lines in Fig. 56), which is consistent with the expected 6-photon ionization at low intensities. An additional measurement with more data points at low intensities for circular polarization, not presented here, has demonstrated that phase data can be fitted only with I^6-law, which represents clear evidence of the 6-photon ionization mechanism.

The curves for the logarithm of transmission lie significantly below the phase dependencies and provide equal values of the collision time of about 1.2 fs, with slight dependence on laser intensity. The numerical values are in perfect agreement with previously discussed measurements (see Fig 55).

With growing intensities the curves for the two polarizations deviate more and more from the multiphoton law, come close together and saturate ("zero slope" is reached) at the intensities around 40 TW/cm^2. The surface breakdown threshold is reached at significantly higher intensities of I_{lin}^{thr}=54.5 TW/cm^2 and I_{circ}^{thr}=62 TW/cm^2 for linear and circular polarizations, respectively. The values of surface breakdown intensities are almost twice as large as for fused silica. In the same manner as described in the previous section, we have tried to model and explain the observed dependencies by a multiphoton ionization combined with spatially inhomogeneous free-carrier distribution. For any set of intensity-independent parameters, which fit the data for low intensities it was impossible to get "zero slope" for high intensities below break-

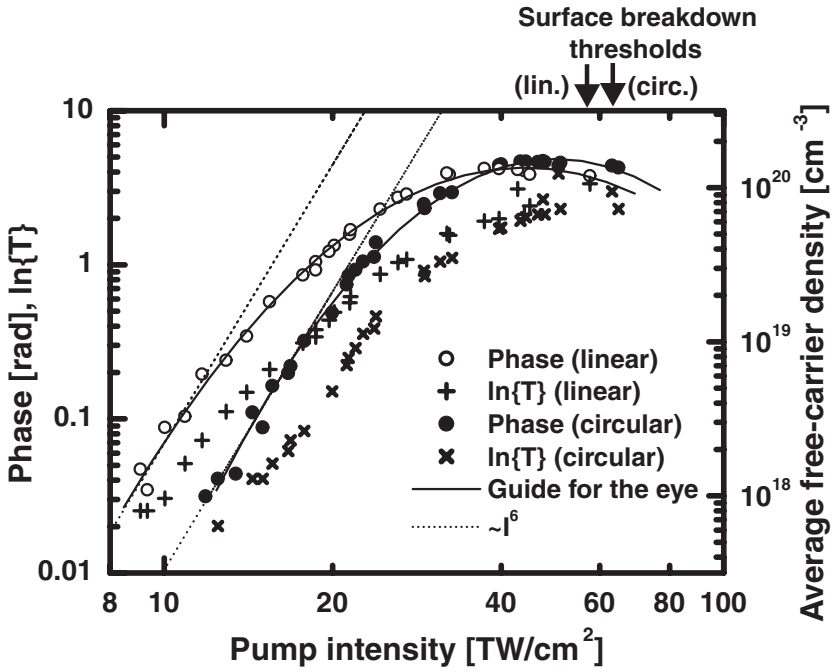

Figure 56: Intensity dependence of phase shift (circles) and the logarithm of transmission (crosses) for linear and circular polarizations in sapphire, Δt=1 ps. The continuous lines denotes as "guide for the eye" are obtained from polynomial fit of phase dependencies, whereas the dotted lines are proportional to I^6. The arrows in the upper right corner denote the intensities at which surface breakdown thresholds are reached for two polarizations.

down threshold. The critical density of free carriers is always reached for incident intensities below 40 TW/cm^2. This analysis strongly suggests that the ionization mechanism at high intensities is *different* from multiphoton ionization. Of course, one could argue that the band structure is strongly distorted by a strong external field and that the multiphoton ionization mechanism can be rescued by introducing some intensity-dependent parameters. The high intensity needed to produce surface breakdown corresponds to electric fields of about 170 MV/cm, which is comparable with the strong internal field of the the crystal (see Eq. (49) and corresponding numerical estimations). One could also think that such strong external electric fields simply break the ionic bonds and disrupt the crystal, which might be an alternative physical mechanism for surface breakdown. However, for equal intensities the peak electric fields in linearly and circularly polarized waves are different by the factor of $\sqrt{2}$. The breakdown fields calculated from breakdown intensities are found to be quite different F_{lin}^{thr}=153 MV/cm and F_{circ}^{thr}=115.5 MV/cm, which rules out breakdown mechanism via direct bond-breaking. The same arguments can be applied in the case of fused silica.

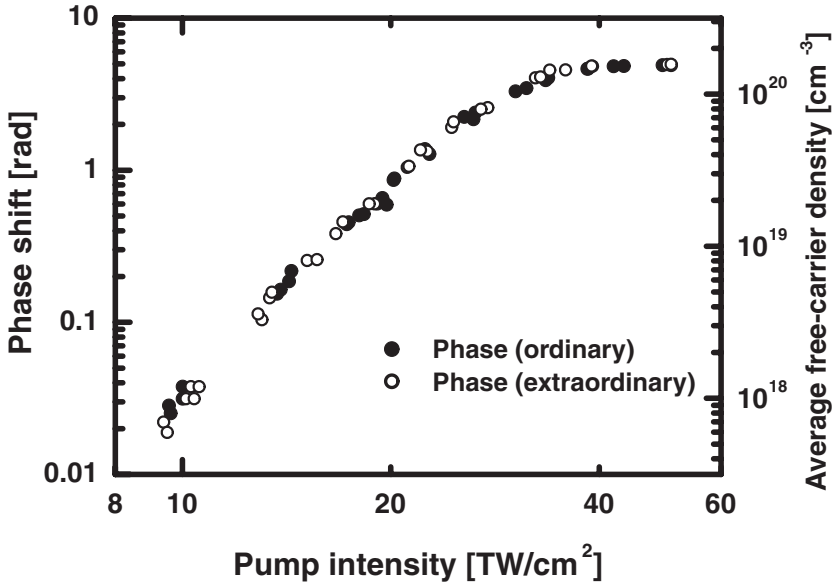

Figure 57: Intensity dependence of ionization rate (phase shift) by ordinary and extraordinary pump pulses in sapphire, $\Delta t = 1$ ps.

At low intensities the cross-sections of 6-photon-ionization are found to be $\sigma_6^{lin} = 20 \times 10^{-47\pm0.5}$ [$s^{-1}cm^9/W^6$] for linear and $\sigma_6^{circ} = 3 \times 10^{-47\pm0.5}$ [$s^{-1}cm^9/W^6$] for circular polarizations. In order to fit the experimental data for linear polarization with Keldysh's formula for multiphoton ionization, the effective mass m^*=0.38 is required, which is slightly larger than the expected value of $m^* = 0.25$ [117]. For I=10 TW/cm^2 and $n_0 = 1.76$ the estimated value of the Keldysh parameter $\gamma \simeq 1.5$ is the same as for fused silica. Thus, we are again just at the applicability limit for the multiphoton limit of Keldysh's theory of photoionization. Although sapphire is a crystal with a direct band-gap which corresponds to the assumptions of Keldysh's model calculations, their applicability is questionable because of extremely short collision times.

In order to compare the ionization rates with linearly polarized ordinary and extraordinary pump pulses, we have performed interferometric measurements in 50 μm-thin sapphire (1120) plates with the optical axis lying in the surface of the sample. Figure 57 shows the dependencies of the ionization rate on laser intensity for the ordinary and extraordinary pump pulses. The ionization rates but also the surface breakdown thresholds appear to be identical for ordinary and extraordinary pump pulses. Probe transmission curves (not shown) indicate that the collision time is somewhat larger for an ordinary pulse, which is in agreement with previously discussed data.

4.7 Conclusions and future perspectives

In this chapter we have discussed the problems related to the ionization of dielectrics by ultrashort laser pulses. Significant efforts have been devoted to the understanding of the physical background and fundamental limitations of Keldysh's theory of photoionization, which is usually applied to explain various experimental data. A specially designed setup for femtosecond time-resolved imaging Mach-Zehnder interferometry was applied to study ultrafast dynamics of the optical properties in fs-laser excited dielectrics, fused silica and sapphire. We have observed a positive cross-correlation signal due to the pump-induced optical Kerr effect during the pump pulse and a negative phase shift and absorption after the pump pulse, which were attributed to the contribution of laser-generated free carriers and interpreted in the frame of Drude-model. The optical Kerr-effect is found to dominate the contribution of free-carriers, which makes it impossible to study the dynamics of the electron gas during the pump pulse.

The results of the investigations clearly demonstrate that the dominant ionization mechanism for both investigated dielectric materials, fused silica and sapphire, is the 6-photon ionization for low intensities below 10 TW/cm^2. The multiphoton ionization is found to depend on the polarization state of pump pulses (linear versus circular), whereas the experimental data allowed for a relatively precise determination of the cross-sections for 6-photon absorption for both polarizations. We were able to measure small differences in the surface breakdown thresholds for two polarizations for both materials: a higher breakdown threshold for circular polarization corresponds to a lower rate of multiphoton ionization, as compared to the linear polarization.

For higher intensities some conspicuous deviations from multiphoton ionization law are observed. These can be explained by strongly inhomogeneous excitation of the dielectrics localized within a few microns from the sample surface. For fused silica it was possible to model the results of interferometric measurements by assuming the multiphoton ionization mechanism for all intensities up to surface breakdown thresholds, which is masked by the effect of spatial averaging. Moreover, the breakdown thresholds for both linear and circular polarizations coincide very well with the calculated intensities at which the critical free-carrier density is reached at the surface via multiphoton ionization. Nothing like that could be obtained for experimental data in sapphire, indicating the transition to a *different* ionization mechanism at high intensities.

The measured electronic collision times appear to be extremely short $\tau_c \leq 1$ fs, with

little variation on pump intensity. Being significantly shorter than the period of the optical cycle these femtosecond collision times seem to be a universal characteristic of hot carrier transport in dielectrics due to the huge electron-phonon scattering rates for hot electrons [93, 115]. This observation strongly suggests that Keldysh's collisionless ionization theory for strong fields must be generalized to incorporate electronic collisions. The effect of strong "collisional broadening", $\delta\omega_{coll} = 2/\tau_c \sim \omega$, could be even more important than taking care of the detailed band structure in Keldysh's photoionization theory. On the other hand electronic collisions are the basis for free-carrier absorption, which is a starting point for avalanche ionization theories.

The experimental geometry, in which we were able to measure the dynamics of optical properties in the bulk of fs-laser-excited dielectrics, appeared to be useful only for low intensities far below the surface breakdown threshold. For high intensities the information about the ionization mechanisms is masked by spatial averaging over a strongly inhomogeneous spatial free-carrier distribution primarily in the propagation direction. In order to directly study ionization mechanisms in the pre-breakdown regime (for free-carrier concentration just below the critical plasma density) one could perform interferometric measurements in reflection with a Michelson-type interferometer. The sensitivity of the technique is high enough to detect free-carrier densities of about 10^{20} cm^{-3}, which is still much smaller than the critical density. Moreover, since for such free-carrier concentrations the contribution from the pump-induced optical Kerr-effect becomes negligibly small, one could think about measuring the temporal evolution of free-carriers *during* the pump pulse. Therefore, apart from doing conventional interferometry, one could develop the setup for broad-band spectral interferometry, which according to Geindre at al. [118] might in principle provide temporal resolution given not by the *duration* but *coherence time* of the probe pulses, which could be as short as a few femtoseconds. Using 3 ps-long pulses (obtained by the stretching of 35 fs-short pulses) Geingre at al. [118] have demonstrated 50 fs temporal resolution of phase measurement. One could invert their original idea and essentially apply any type of well-defined and reproducible temporal phase modulation (no random phase!) to femtosecond pulses in order to broaden their spectra and, therefore, improve temporal resolution down to a few femtoseconds. However, the precise technical requirements under which such ultimate temporal resolution can be achieved need to be clarified.

5 Conclusion

In this work we have presented the technique for ultrafast time-resolved imaging interferometry and its application to the two different problems of laser-matter interaction: femtosecond laser ablation of absorbing solids and optical breakdown in dielectrics.

The presented detailed analysis of the technique including the optical design of the Michelson- and Mach-Zehnder-type imaging interferometers, analysis of the image formation and its relation to the 2D-Fourier-transform algorithm, artifacts in the reconstructed phase and amplitude maps as well as the physical interpretation of phase measurements represent a significant development in the field of time-resolved imaging interferometry. Without such analysis the results of interferometric measurements would be not so valuable and their interpretation not unique.

Interferometric measurements at an ablating GaAs-surface allowed us to directly observe several types of transient surface deformations of laser-excited material both below and above the ablation threshold. The results of interferometric measurements support the theoretically predicted inhomogeneous "bubble-like" internal structure of an ablating layer. The expansion velocity of a hot pressurized laser-molten layer of material is shown to slow down during the first few hundred of picoseconds of expansion, which strongly indicates the build up of tensile stresses in a liquid upon expansion (negative pressure). The observed extremely slow large-amplitude reversible surface deformations could be explained by the frustrated liquid-gas phase transition. This motivates further theoretical investigations of femtosecond laser ablation, which must be focused on the properties of metastable liquids under negative pressure. The variety of new findings deduced from the measurements in GaAs motivate further interferometric studies in different materials and possibly using slightly different experimental configurations. As in the case of the universal Newton fringe phenomena we anticipate transient surface deformations to be driven by a material-independent mechanism. Finally, the price/quality ratio of interferometric measurements at ablating surfaces appeared to be very attractive and the chances of fully understanding the basic physical mechanisms of femtosecond laser ablation in the near future are very good.

Interferometric measurements in transmission made with the help of imaging Mach-Zehnder-type interferometry aimed to clarify the ionization mechanisms in dielectrics irradiated by single intense femtosecond laser pulses. Significant efforts have been made to get rid of the propagation effects such as self-phase modulation and self-focusing, which only represent additional complications in these types of experi-

ments. The 50 fs-time resolution achieved allowed us to follow the extremely fast dynamics of free carriers in sapphire and fused silica just after excitation. We were able to clearly demonstrate that at relatively low intensities below 10 TW/cm^2 the dominant ionization mechanism is the 6-photon ionization, which is polarization dependent. The surface breakdown threshold does also slightly depend on laser polarization. The cross-sections of multiphoton ionization have been determined with an accuracy, which is much better than in all previously reported studies. However, at high intensities the spatial averaging in the propagation direction has been shown to be important. The comparison of experimental data with the results of model calculations of 1D-pulse propagation in dielectrics suggests that in fused silica the multiphoton ionization might be the dominant ionization mechanism up to the surface breakdown threshold, whereas for sapphire the ionization mechanism must be different in the pre-breakdown regime. The attempts to compare the experimental data with the predictions of Keldysh's theory of photoionization were not successful. Without redoing Keldysh's calculations we were able to understand the limitations and assumptions behind his model calculations. Whereas Keldysh's general approach is very interesting and elegant from a theoretical point of view, his model calculations could not be applied for the given experimental situation. The most important problem is that high-field carrier transport in dielectrics induces extremely fast electron-lattice collisions, which are not included in Keldysh's approach. Finally, the price/quality ratio of interferometric measurements in dielectrics appeared to be rather moderate and the chances of understanding the ionization mechanisms in dielectrics in the pre-breakdown regime in the near future are slim.

References

[1] K. Sokolowski-Tinten, J. Bialkowski, A. Cavalleri, D. von der Linde, A. Oparin, J. Meyer-ter-Vehn, S.I. Anisimov, "Transient states of matter during short pulse laser ablation," Phys. Rev. Lett. **81,** 224-227 (1998)

[2] D. von der Linde, K. Sokolowski-Tinten, "The physical mechanisms of short-pulse laser ablation," Appl. Surf. Sci. **154-155,** 1-10 (2000)

[3] V.V. Temnov, K. Sokolowski-Tinten, N. Stojanovic, S. Kudryashov, D. von der Linde, B. Kogan, A. Schlarb, B. Weyers, R. Möller, J. Seekamp, C. Sotomayor-Torres, " Microscopic characterization of ablation craters produced by femtosecond laser pulses," Proc. SPIE **4760,** 1032-1039 (2002)

[4] M.C. Downer, R.L. Fork, C.V. Shank, "Femtosecond imaging of melting and evaporation at a photoexcited silicon surface," J. Opt. Soc. Am. B **4,** 595-598 (1985)

[5] T. Masubuchi, H. Furutani, H. Fukumura, H. Masuhara, "Laser-induced nanometer-nanosecond expansion and contraction dynamics of poly(methyl methacrylate) film studied by time-resolved interferometry," J. Phys. Chem. B **105,** 2518-2524 (2001)

[6] S.R. Greenfield, J.L. Casson, A.C. Koskelo, "Nanosecond interferometric studies of surface deformations of dielectrics induced by laser irradiation," Proc. SPIE **4065,** 557-566 (2001)

[7] J.P. Geindre, P. Audebert, A. Rousse, F. Fallies, J.C. Gauthier, A. Mysyrowicz, A. Dos Santos, G. Hamoniaux, A. Antonetti, "Frequency-domain interferometer for measuring the phase and amplitude of a femtosecond pump-probing a laser-produced plasma," Opt. Lett. **19,** 1997-1999 (1994)

[8] R. Evans, A.D. Badger, F. Fallies, M. Mahdieh, T.A. Hall, P. Audebert, J.P. Geindre, J.C. Gauthier, A. Mysyrowicz, G. Grillon, A. Antonetti, "Time- and space-resolved optical probing of femtosecond-laser-driven shock waves in aluminum," Phys. Rev. Lett. **77,** 3359-3362 (1996)

[9] P. Audebert, Ph. Daguzan, A. Dos Santos, J.C. Gauthier, J.P. Geindre, S.Guizard, G. Hamoniaux, K. Krastev, P. Martin, G. Petite, A. Antonetti, "Space-time observation of an electron gas in SiO_2," Phys. Rev. Lett. **73,** 1990-1993 (1994)

[10] V.P. Linnik, "Ein Apparat für mikroskopisch-interferometrische Untersuchung reflektierender Objekte (Mikrointerferometer)", Akad. Nauk. SSSR Dokl., Vol. **1**, 18-23 (1933)

[11] M. Francon, Jr., *Optical interferometry* (Academic Press, New York, 1966), Chap. #16

[12] V.V. Temnov, K. Sokolowski-Tinten, P. Zhou, D. von der Linde, "Femtosecond time-resolved interferometric microscopy," Appl. Phys. A **78,** 483-489 (2004)

[13] D.J. Bone, H.-A. Bachor, and J. Sandeman, "Fringe-pattern analysis using a 2-D Fourier transform," Appl. Opt. **25,** 1653-1660 (1986)

[14] C. Roddier and F. Roddier, "Interferogram analysis using Fourier transform techniques," Appl. Opt. **26,** 1668-1673 (1987)

[15] A.S. Zakharov, M.V. Volkov, I.P. Gurov, V.V. Temnov, K. Sokolowski-Tinten, D. von der Linde, "Interferometric diagnostics of ablation craters formed by femtosecond laser pulses," J. Opt. Technol. **69,** 478-482 (2002)

[16] M. Takeda, H. Ina, and S. Kobayashi, "Fourier-transform method of fringe-pattern analysis for computer-based topography and interferometry," J. Opt. Soc. Am. **72,** 156-160 (1982)

[17] M. Kujawinska, "Spatial phase measurement methods," in *Interferogram Analysis: Digital Fringe Pattern Measurement Techniques*, D.W. Robinson and G.T. Reid, ed. (IOP, Bristol, 1993)

[18] S. Lawrence Marple, Jr., *Digital spectral analysis with applications* (Prentice Hall, New Jersey, 1987)

[19] K.A. Nugent, "Interferogram analysis using an accurate fully automatic algorithm," Appl. Opt. **24,** 3101-3105 (1985)

[20] J.H. Massig, and J. Heppner, "Fringe-pattern analysis with high accuracy by use of the Fourier-transform method: theory and experimantal tests," Appl. Opt. **40,** 2081-2088 (2001).

[21] M. Born and E. Wolf, *Principles of Optics* (Pergamon Press, Oxford, 1980), Chap. #9

[22] J.W. Goodman, *Introduction to Fourier Optics* (McGraw-Hill, New York, 1968), Chap. #5

[23] G.O. Reynolds, J.B. DeVelis, G.B. Parrent, Jr., and B.J. Thompson, *The new physical optics notebook: Tutorials in Fourier optics* (Copublished by SPIE, Bellingham, and AIP, New York, 1989)

[24] J.B. Liu and P.D. Ronney,"Modified Fourier transform method for interferogram fringe pattern analysis", Appl. Opt. **36,** 6231-6241 (1997)

[25] R.T. Holm, "Convention confusions," in *Handbook of Optical Contstants of Solids II*, E.D. Palik, ed. (Academic Press, San Diego, 1991)

[26] K. Sokolowski-Tinten, J. Bialkowski, M. Boing, A. Cavalleri, D. von der Linde, "Thermal and non-thermal melting of gallium arsenide after femtosecond laser excitation," Phys. Rev. B **58,** R11805-11808 (1998)

[27] E.D. Palik, "Gallium Arsenide (GaAs)," in *Handbook of Optical Contstants of Solids*, E.D. Palik, ed. (Academic Press, Orlando, 1985)

[28] D. von der Linde and H. Schüler, "Breakdown threshold and plasma formation in femtosecond laser-solid interaction," J. Opt. Soc. Am. B **13,** 216-222 (1996)

[29] D.W. Robinson, "Phase unwrapping methods," in *Interferogram Analysis: Digital Fringe Pattern Measurement Techniques*, D.W. Robinson and G.T. Reid, ed. (IOP, Bristol, 1993)

[30] D.C. Ghiglia, G.A. Mastin, and L.A. Romero, "Cellular-automata method for phase unwrapping," J. Opt. Soc. Am. A **4,** 267-280 (1987)

[31] B.B. Hubbard, "Wavelets: die Mathemetik der kleinen Wellen", Birkhäser Verlag, Basel (1997)

[32] L. Onural, "Diffraction form a wavelet point of view," Opt. Lett. **18,** 846-848 (1993)

[33] T.M. Jorgensen, J. Glückstad, L. Onural, "Diffraction form a wavelet point of view: comment," Opt. Lett. **19,** 423 (1994); L. Onural, "Diffraction form a wavelet point of view: reply to comments," Opt. Lett. **19,** 424 (1994)

[34] Acta Opta Sinica **20,** 1617-1621 (2000) (in chinese)

[35] R. Yen, J. M. Liu, H. Kurz, and N. Bloembergen, "Space-time resolved reflectivity measurements of picosecond laser-pulse induced phase transitions in (111) silicon surface layer," Appl. Phys. A **27**, 153-160 (1982)

[36] J. Bialkowski, "Femtosekunden-laserinduzierter Materialabtrag," Ph.D. Thesis, University of Essen, (1998)

[37] A. Boroviec, M. MacKenzie, G. C. Weatherly, and H. K. Haugen, "Electron and atomic force microscopy studies of femtosecond laser machining of Si, GaAs and InP," CLEO 2001 Proc., 440-441 (2001)

[38] M. von Allmen, "Laser-Beam Interactions with Materials", Springer, Berlin (1995)

[39] D. von der Linde, K. Sokolowski-Tinten, C. Blome, C. Dietrich, A. Tarasevitch, A. Cavalleri, J.A. Squier, "'Ultrafast' extended to x-rays: femtosecond time-resolved x-ray deffraction," Z. Phys. Chem. **215,** 1527-1541 (2001)

[40] A. Cavalleri, K. Sokolowski-Tinten, J. Bialkowski, M. Schreiner, D. von der Linde, "Femtosecond melting and ablation of semiconductors studied with time of flight mass spectroscopy," J. Appl. Phys. **85,** 3301-3309 (1999)

[41] U. Kreibig, M. Vollmer, "Optical properties of metal clusters", Springer, Berlin (1995)

[42] S.I. Anisimov, N.A. Inogamov, A.M. Oparin, B. Rethfeld, T. Yabe, M. Ogawa, V.E. Fortov, "Pulsed laser evaporation: equation-of-state effects," Appl. Phys. A **69,** 617-620 (1999)

[43] N.A. Inogamov, Yu.V. Petrov, S.I. Anisimov, A.M. Oparin, N.V. Shaposhnikov, D. von der Linde, J. Meyer-ter-Vehn, "Expansion of matter heated by an ultrashort laser pulse," JETP Lett. **69,** 310-316 (1999)

[44] V. V. Zhakhovskii, K. Nishihara, S.I. Anisimov, N.A. Inogamov, "Molecular-dynamics simulation of rarefaction waves in media that can undergo phase transitions," JETP Lett. **71,** 167-172 (2000)

[45] V. V. Zhakhovskii, *private communication* (2004)

[46] V.P. Skripov, A.V. Skripov, "Spinodal decomposition (phase transitions via unstable states)," Usp. Fiz. Nauk **128,** 389-410 (1979)

[47] S. aus der Wiesche, C. Rembe, E.P. Hofer, "Boiling of superheated liquids near the spinodal: I general theory," Heat and Mass Transfer **35,** 25-31 (1999)

[48] L.D. Landau, E.M. Lifshitz, "Fluid mechanics", Pergamon Press, Oxford (1959)

[49] J.M. Liu, "Simple technique for measurements of pulsed Gaussian-beam spot sizes," Opt. Lett. **7,** 196-198 (1982)

[50] F. Hensel, W.W. Warren, 'Fluid metals: the liquid-vapor transitions of metals", Princeton University Press, Princeton (1999)

[51] N.F. Mott, "Metal-insulator transitions", Taylor & Francis, London (1990)

[52] Q.M. Zhang, G. Chiarotti, A. Selloni, R. Car, M. Parrinello, "Atomic structure ans bonding in liquid GaAs from *ab initio* molecular dynamics," Phys. Rev. B **42,** 5071-5081 (1990)

[53] K. Sokolowski-Tinten, J. Bialkowski, A. Cavalleri, D. von der Linde, "Observation of a transient insulating phase of metals and semiconductors during short-pulse laser ablation," Appl. Surf. Sci. **127-129,** 755-760 (1998)

[54] N. Yoshimoto, H. Shibata, M. Yoshizawa, K. Suzuki, K. Shigematsu, S. Kimura, "Sound velocity measurements of molten germanium," Jpn. J. Appl. Phys. **35,** 2754-2757 (1996)

[55] N. Yoshimoto, M. Ikeda, M. Yoshizawa, S. Kimura, "Sound velocity measurements of molten silicon," Physica B **219-220,** 623-625 (1996)

[56] A. Vaidyanathan, A.H. Guenter, S.S. Mitra, "Band-structure calculations of the two-photon absorption coefficients of GaAs, InP, CdTe, and ZnSe," Phys. Rev. B **24**, 2259-2262 (1981)

[57] K. Sokolowski-Tinten, "Femtosekunden-laserinduzierte Phasenübergänge in Halbleitern," Ph.D. Thesis, University of Essen, (1994)

[58] A.S. Jordan, "An evaluation of the thermal and elastic constants affecting GaAs crystal growth," J. Cryst. Growth **49,** 631-642 (1980)

[59] A.S. Jordan, "Estimated thermal diffusivity, Prandtl number and Grashof number of molten GaAs, InP, and GaSb," J. Cryst. Growth **71,** 551-558 (1985)

[60] L.D. Landau, E.M. Lifshitz, "Statistical physics", Pergamon Press, Oxford (1969)

[61] P.H. Poole, F. Sciortino, U. Essmann, H.E. Stanley, "Spinodal of liquid water," Phys. Rev. E **48,** 3799-3817 (1993)

[62] R. Kelly, A. Miotello, "Comments on explosive mechanisms of laser sputtering," Appl. Surf. Sci. **96-98,** 205-215 (1996)

[63] V.E. Fortov, V.V. Kostin, "Spallation of metals under laser radiation," J. Appl. Phys. **70,** 4524-4531 (1991)

[64] S.I. Anisimov, V.V. Zhakovskii, N.A. Inogamov, K. Nishihara, A.M. Oparin, Y.V. Petrov, "Distruction of a solid film under the action of ultrashort laser pulse," JETP Lett. **77,** 606-610 (2003)

[65] D.F. Egwards, "Silicon (Si) revisited (1.4-6.0 eV)," in *Handbook of Optical Contstants of Solids III*, E.D. Palik, ed. (Academic Press, San Diego, 1998)

[66] L.V. Keldysh, "Ionization in the field of a strong electromagnetic wave," Sov. Phys.-JETP **20**, 1307-1314 (1965)

[67] A. Kaiser, B. Rethfeld, M. Vicanek, G. Simon, "Microscopic processes in dielectrics under irradiation by subpicosecond laser pulses," Phys. Rev. B **61**, 11437-11450 (2000)

[68] L.V. Keldysh, "Kinetic theory of impact ionization in semiconductors," Sov. Phys.-JETP **37**, 509-518 (1960)

[69] M. Protopapas, C.H. Keitel, P.L. Knight, "Atomic physics with super-high intensity lasers," Rep. Prog. Phys. **60**, 389-485 (1997)

[70] Y.R. Shen, "The principles of nonlinear optics", John Wiley & Sons, New York (1984)

[71] L.V. Keldysh, "Behavior of non-metallic crystals in strong electric fields," Sov. Phys.-JETP **6**, 763-770 (1958)

[72] L.V. Keldysh, "Influence of the lattice vibrations of a crystal on the production of electron-hole pairs in a strong electric field," Sov. Phys.-JETP **34**, 665-668 (1958)

[73] L.V. Keldysh, "The effect of a strong electric field on the optical properties of insulating crystals," Sov. Phys.-JETP **34**, 778-790 (1958)

[74] H.D. Jones, H.R. Reiss, "Intense-field effects in solids," Phys. Rev. B **16**, 2466-2473 (1977)

[75] L.M. Narducci, S.S. Mitra, R.A. Shatas, P.A. Pfeiffer, A. Vaidyanathan, "One-photon Keldysh absorption in direct-gap semiconductors," Phys. Rev. B **14**, 2508-2513 (1976)

[76] A. Vaidyanathan, T.W. Walker, A.H. Guenter, S.S. Mitra, L.M. Narducci, "Comparison of Keldysh and perturbation formulas for one-photon absorption," Phys. Rev. B **20**, 3526-3527 (1979)

[77] A. Vaidyanathan, T. Walker, A.H. Guenter, S.S. Mitra, L.M. Narducci, "Two-photon absorption in several direct-gap crystals," Phys. Rev. B **21**, 743-748 (1980)

[78] A. Vaidyanathan, A.H. Guenter, S.S. Mitra, "Two-photon absorption in direct-gap crystals - an addendum ," Phys. Rev. B **22**, 6480-6483 (1980)

[79] A. Tien, S. Backus, H. Kapteyn, M. Murnane, G. Mourou, "Short-pulse laser damage in transparent materials as a function of pulse duration," Phys. Rev. Lett. **82**, 3883-3886 (1999)

[80] C.B. Shaffer, A. Brodeur, E. Mazur, "Laser-induced breakdown and damage in bulk transparent materials induced by tightly focused femtosecond laser pulses," Meas. Sci. Technol. **12**, 1784-1794 (2001)

[81] L. Sudrie, A. Couairon, M. Franco, B. Lamouroux, B. Prade, S. Tzortzakis, A. Mysyrowicz, "Femtosecond laser-induced damage and filamentary propagation in fused silica," Phys. Rev. Lett. **89**, 186601 (2002)

[82] V.L. Bonch-Bruevich, S.G. Kalaschnikov, "Halbleiterphysik", VEB Deutscher Verlag der Wissenschaften, Berlin (1982)

[83] J.H. Yee, "Three-photon absorption in semiconductors," Phys. Rev. **5**, 449-458 (1972)

[84] J.H. Yee, "Four-photon absorption in semiconductors," Phys. Rev. **5**, 355-360 (1972)

[85] D.M. Volkov, "Uber eine Klasse von Lösungen der Diracschen Gleichung," Z. Phys. **94**, 250 (1935)

[86] W.V. Houston, "Acceleration of electrons in a crystal lattice," Phys. Rev. **57**, 184-186 (1940)

[87] E.O. Kane, "Band structure of indium antimonide," J. Phys. Chem. Solids **1**, 249-261 (1957)

[88] V.Ya. Demikhovskii, G.A. Vugalter, "Fisika kvantovich niskorasmernich struktur" (in Russian), Logos, Moscow (2000)

[89] F. Bassani, G. Pastori Parravicini, "Electronic states and optical transitions in solids," Pergamon Press, Oxford (1975)

[90] M. Abramowitz, I.A. Stegun, *Handbook of mathematical functions* (National Bureau of Standards, Applied Mathematics Series 55, Washington, 1972)

[91] V.E.Gruzdev, "Analysis of Keldysh's formula for the ionization rate in solids," *to appear* in Proc. SPIE **5506** (2004)

[92] O. Svelto, "Principles of lasers," Plenum Press, New York (1998)

[93] M.V. Fischetti, D.J. DiMaria, S.D. Brorson, T.N. Theis, J.R. Kirtley, "Theory of high-field electon transport in silicon dioxide," Phys. Rev. B **31**, 8124-8142 (1985)

[94] V.Ya. Demikhovskii, G.A. Vugalter, "Multiphoton ionization of a quantum well," J. Phys.: Condens. Matter **8**, 2585-2595 (1996)

[95] E. Yablonovitch, N. Bloembergen, "Avalanche ionization and the limiting and the limiting diameter of filaments induced by light pulses in transparent media," Phys. Rev. Lett. **29**, 907-910 (1972)

[96] C.B. Shaffer, A. Brodeur, G.F. Garcia, E. Mazur, "Micromachining bulk glass by use of femtosecond laser pulses with nanojoule energy," Opt. Lett. **26**, 93-95 (2001)

[97] S. Tzortzakis, L. Sudrie, M. Franco, B. Prade, A. Mysyrowicz, A. Couairon, L. Berge, "Self-guided propagation of ultrashort IR laser pulses in fused silica," Phys. Rev. Lett. **87**, 212902 (2001)

[98] J.K. Ranka, R.W. Schirmer, A.L. Gaeta, "Observation of pulse splitting in nonlinear dispersive media," Phys. Rev. Lett. **77**, 3783-3785 (1996)

[99] T. Brabec, F. Krausz, "Nonlinear optical pulse propagation in the single-cycle regime," Phys. Rev. Lett. **78**, 3282-3285 (1997)

[100] S. Henz, J. Herrmann, "Self-channeling and pulse shortening of femtosecond pulses in multiphoton-ionized dispersive dielectric solids," Phys. Rev. B **59**, 2528-2531 (1999)

[101] A.L. Gaeta, "Catastrophic collapse of ultashort pulses," Phys. Rev. Lett. **84**, 3582-3585 (2000)

[102] P. Martin, S. Guizard, Ph. Daguzan, G. Petite, P. D'Oliveira, P. Meynadier, M. Perdrix, "Subpicosecond study of carrier trapping dynamics in wide-band-gap crystals," Phys. Rev. B **55**, 5799-5810 (1997)

[103] F. Quere, S. Guizard, Ph. Martin, "Time-resolved study of laser-induced breakdown in dielectrics," Europhys. Lett. **56**, 138-144 (2001)

[104] A. Brodeur, S.L. Chin, "Band-gap dependence of the ultrafast white-light continuum," Phys. Rev. Lett. **80**, 4406-4409 (1998)

[105] R. Trebino, D.J. Kane, "Using phase retrieval to measure the intensity and phase of ultrashort pulses: frequency–resolved optical gating," J. Opt. Soc. Am. A **10**, 1101-1111 (1993)

[106] A. Horn, "Zeitaufgelöste Analyse der Wechselwirkung von ultrakurz gepulster Laserstrahlung mit Dielektrika," PhD Thesis, RWTH-Aachen (2003)

[107] W.Y. Ching, "Microscopic calculation of localized electron states in an intrinsic glass," Phys. Rev. Lett. **46**, 607-610 (1981)

[108] W.Y. Ching, "Theory of amorphous SiO_2 and SiO_x. II. Electron states in an intrinsic glass," Phys. Rev. B **26**, 6622-6632 (1982)

[109] R.C. Hughes, "Charge-carrier transport phenomena in amorphous SiO_2: direct measurement of the drift mobility and lifetime," Phys. Rev. Lett. **30**, 1333-1336 (1973)

[110] S. Katz, A. Halperin, "Thermally stimulated luminescence and its thermally stimulated current in quartz," Phys. Rev. B **36**, 6646-6650 (1987)

[111] D. Arnold, E. Cartier, D.J. DiMaria, "Acoustic-phonon runaway and impact ionization by hot electrons in silicon dioxide," Phys. Rev. B **45**, 1477-1480 (1992)

[112] H.R. Philipp, "Silicon dioxide (SiO_2)(glass)," in *Handbook of Optical Contstants of Solids*, E.D. Palik, ed. (Academic Press, Orlando, 1985)

[113] W.J. Tropf, M.E. Thomas, "Aluminum oxide (Al_2O_3) revisited," in *Handbook of Optical Contstants of Solids III*, E.D. Palik, ed. (Academic Press, San Diego, 1998)

[114] R.W. Klaffky, B.H. Rose, A.N. Goland, G.J. Dienes, "Radiation-induced conductivity of Al_2O_3: experiment and theory," Phys. Rev. B **21**, 3610-3634 (1980)

[115] K.K. Thornber, R.P. Feynman, "Velocity acquired by an electron in a finite electric field in a polar crystal," Phys. Rev. B **1**, 4099-4114 (1970)

[116] R.C. Hughes, "Generation, transport, and trapping of excess charge carriers in Czochralski-grown sapphire," Phys. Rev. B **19**, 5318-5328 (1979)

[117] J. Shan, F. Weng, E. Knoesel, M. Bonn, T.F. Heinz, "Measurement of the frequency-dependent conductivity in sapphire," Phys. Rev. Lett. **90**, 247401 (2003)

[118] J.P. Geindre, P. Audebert, S. Rebibo, J.C. Gauthier, "Single-shot spectral interferometry with chirped pulses," Opt. Lett. **26**, 1612-1614 (2001)

Acknowledgements

First of all I would like to thank Prof. Dr. Dietrich von der Linde for giving me the opportunity to work on highly interesting projects and benefit from the experience of international collaboration. Only under his supervision was I able to learn the right way of doing research in the field of experimental and theoretical physics.
I am particularly indebted to Klaus Sokolowski-Tinten for his active participation in all of my research activities, the fruitful discussions I had with him and his creative ideas. Also for his encouragement and giving me the opportunity to participate in many highly interesting international conferences. The discussions with Bärbel Rethfeld and Vitaly Gruzdev were also extremely helpful.
The invaluable contribution by Ping Zhou to this work should be mentioned. Being an excellent specialist in laser physics and the father of our femtosecond laser system, Ping was ready to help whenever I had problems with the laser.
All members of the research group have contributed to the nice atmosphere in which this work was carried out. Without intense scientific debates during informal coffee-breaks many aspects of ultrafast science would never have opened up to me.
It would be incorrect not to mention our international collaborators S.I. Ashitkov, M. Meunier, M. Wiggins, and A.M. Zheltikov with whom I spent much time in the lab and have learned a lot.
Prof. R. Möller and Prof. C. Sotomayor-Torres provided an invaluable contribution to the microscopic characterization of ablation craters, which is a part of this dissertation. I am also grateful to Prof. R. Möller for his agreement to review my dissertation.
If was helpful not to have to care about many mundane problems, which were dealt with by our technician Michael Bieske, engineer Bernd Proff and secretary Kay Eibl, who did their job very well. I am particularly indebted to Kay Eibl for the numerous corrections she made to my original text.
I would like to thank all of my friends and particularly Evgueni and Sinaida Klimovi for help and support.
Finally, I am indebted to my wife Julia, and my children Michael and Olga for their love and patience during my sometimes unpredictable working times, and also to my parents and grandmother for their support from far away.